University of Trento

Department of Physics

Doctoral thesis
Cycle XXIX

EXPERIMENTS AND MODELLING OF VERTICALLY COUPLED MICRORESONATORS

Candidate: Fabio Turri
Supervisor: Prof. Lorenzo Pavesi

Academic year 2016/2017

A Caterina,
che mi regala sorrisi
e mi riempie la vita.

Abstract

Microresonators are fundamental building blocks in the growing field of integrated photonics and several resonator-based devices such as filters, switches and routers are currently used in common optical telecommunication networks. In order to exploit the peculiar features offered by integrated resonators, a complete and consistent comprehension of their physics and of the processes they can accommodate is needed. More specifically, coupling of light to and from a resonator represents a crucial point: a correct comprehension of the coupling dynamics, a proper model for the system and its validation through experimental procedure are all essential elements for a fruitful exploitation of the device. Among the different resonator-waveguide coupling schemes, the most widely used is the *in-plane* coupling and it consists of a waveguide placed near to a microresonator and laying on the same plane. However, an alternative approach is represented by the *vertical coupling* scheme, where the waveguide lays under the resonator edge. The peculiar position of the waveguide in this last configuration causes the device to show specific properties not present in other common coupling schemes: namely, a working range spanning from almost visible wavelengths (780nm) to the near IR domain (1600nm), the selective excitation of high order resonator radial modes and the possibility to fabricate wedge and free-standing resonators without any detrimental effect on the bus waveguide.

In order to fully exploit these and other features of the vertical coupling scheme, a detailed investigation has been carried out throughout this thesis. The waveguide-microresonator system has been studied at different levels, from the general coupling dynamics to more specific and peculiar phenomena. In particular, the basic model proposed for the vertical coupling has been extended to consider wavelength dependences and an experimental validation has been carried out consequently. The reactive coupling model, which describes the internal dynamics of a vertically coupled resonator in the case of multimodal operation, has been experimentally proven. A general model considering the presence counterpropagating modes has been theoretically proposed and experimentally investigated. Finally, the bistable behaviour generated by thermo-optic effect when a large amount of power circulates in the microresonator has been experimentally studied.

In order to better characterize the system response, a specific interferometric setup has been implemented. It consists in a Mach-Zehnder computer driven interferometer, whose peculiar characteristic is the ability to perform simultaneous pump and probe transmittance and phase measurements of any integrated photonic device provided with input and output ports. In this way, the information carried by the phase of the propagating optical signal is added to the one provided by its intensity and contributes to produce a more complete picture of the investigated system. In the case of microresonators this phase information becomes even more fundamental. Indeed, the phase response of a resonating structure is highly influenced by variations in the coupling strength, and the phase spectrum of a single resonance allows to clearly identify the resonator coupling regime for that specific resonance. This fact does not

hold in the case of transmittance measurements, where single resonance spectrum carries information only on the total losses of the system. Finally, in order to exploit the combined information provided by this measurement procedure, a *phasor plot* representation is extensively used throughout the thesis work.

Contents

Thesis motivation and outline

Integrated microresonators have always been considered fundamental building blocks for the realization of a photonic chip. The possibility to use them as filters, switches, integrated lasers, buffers or even all-optical transistors [1] had always attracted the photonic community. Moreover, the electromagnetic field enhancement present inside the resonating cavity, together with other peculiar features owned by microresonators (i.e. the possibility to create freestanding structures, the small dimensions and the precise control of the coupling gap), contributed to make this device a perfect platform for the experimental investigation of fundamental physical phenomena in a variety of fields, from nonlinear optics to quantum optics and cavity optomechanics [2, 3, 4]. As a consequence to these experimental efforts, several structures with different shapes, materials and coupling schemes were fabricated and widely investigated since the realization of the first integrated resonator in 1983 [5]. In this sense Silicon photonics is nowadays the main photonic platform for both research and application: the mature handling of CMOS fabrication process allows high quality devices to be produced and, together with the good optical properties of Silicon (transparency and nonlinear) and its abundance with respect to other materials (i.e. III-V materials), makes this platform the most suitable one for a widespread use and dissemination of photonic integrated devices. Indeed, Silicon microresonator based devices do not represent a renovation only for telecom applications, but they influence also metrology [6] , sensing [7], neural networks [8] and many others research fields.

Among the different coupling schemes that have been proposed in all these applications, a peculiar role is played by the so called *vertical coupling* [9]. Indeed, the interesting properties owned by this kind of coupling could bring advantages in the realization of a photonic chip: the large working range, spanning from almost visible wavelengths to the near IR domain, could be exploited in wideband networks [10]; the selective excitation of high order resonator modes could bring to a selective filter [11]; the possibility to fabricate wedge and free-standing resonators without any detrimental effect on the bus waveguide increases the Q-factor limit and opens the path for robust and more sensitive biosensing elements [12]. However, a careful handling of the system parameters and a correct comprehension of the system dynamics are needed to achieve a full exploitation of its advantages.

In the field of integrated photonics, the physics of a system is commonly investigated by looking at the transmittance response. However, despite the transmittance

of a device represents one of the most important experimental quantity, there is another important quantity that could provide equally important information: the optical phase. Indeed, since any plane electromagnetic wave with wavevector k and frequency ω can be written as $E(r,t) = Ae^{i(kr+\omega t+\varphi)}$, its evolution can be univocally described only if both its amplitude and phase are known. Moreover, in the case of microresonators, the phase response becomes an even more sensible parameter because of the diverse information that can be extracted through the phase spectrum, from the group delay to the coupling regime. Information that cannot be obtained with a simple transmittance measurement under Continuous Wave (CW) excitation.

In the present thesis we take advantage of the combined information given by phase and transmittance measurements to investigate the properties of the vertically coupled resonator system and provide a comprehensive description of the different phenomena observed in the system. Indeed, a specific interferometric setup for the measurement of transmittance and phase responses has been implemented (Chapter 2). The resonator-waveguide system under CW excitation has been theoretically modelled and experimentally observed. A variety of physics has been investigated: from the basic model describing the coupling dynamics of a single mode resonator (Chapter 3), to the intermodal coupling that is observed when multimodal resonators are used (Chapter 4); from the asymmetric resonance doublet that is observed when counterpropagating modes are non equally excited inside the cavity (Chapter 5) to the bistable behaviour observed when high optical input power is used (Chapter 6). The investigated devices are fabricated by Fondazione Bruno Kessler (FBK), whereas their design, modelling and measurements are carried out within the Nanoscience Laboratory (NL) facilities.

More in detail, the outline of the thesis is the following:

- Chapter 1 aims at providing basic notions on the investigated system, which is composed by a bus waveguide and a microresonator. The waveguide responsible for the resonator excitation is presented in Section 1.1, where its working principle and its characterizing parameters are defined. The microresonator is the subject of Section 1.2: at first, the geometry and materials of a microresonator (Section 1.2.1), its working principle (Section 1.2.2) and the different light coupling schemes (Section 1.2.3) are briefly described; successively, a larger section (Section 1.2.4) is devoted to the theoretical model for a singlemode in-plane resonator: the relevant quantities characterizing a resonator and its different coupling regimes are discussed. In the last section (Section 1.3) the new visualization of the system response through phasor plot is introduced: the transmittance and phase information are condensed in the real and imaginary part of the complex electric field vector, which can be represented in a x-y single graph.

- In Chapter 2 the pump and probe interferometric setup built for the simultaneous acquisition of phase and transmittance spectra is presented. Aim of this

Chapter is to get familiar with this specific measurement procedure in order to better comprehend the experimental results shown in Chapters 4, 5 and 6. More specifically, the first part (Section 2.1) contains an introduction to the subject of phase measurements in integrated devices and highlights the main features of the presented setup. The second section of the Chapter (Section 2.2) is mainly devoted to the description of the different elements composing the apparatus; it starts from the three main stages constituting the actual device, whose aim is to generate, make interfere and reveal the probe light beam; it successively focuses on the two different operation modes that can be used to acquire the data and it concludes the description with the automatized measurement pipeline. This last element provides a remote control of the whole measurement procedure and it makes possible to physically isolate the system from the environment reducing the detrimental action of air fluxes and temperature fluctuations. The third part of the Chapter (Section 2.3) contains the experimental characterization of the system through the observation of integrated waveguide and resonator responses. Firstly, the low power characterization of the two devices in the linear regime is reported. Secondly, the results of a second test in high power conditions are discussed: in particular, through Pump&Probe experiment, the possibility to extract a weak probe signal from a strong pump signal is demonstrated even with degenerate pump and probe wavelengths. Finally, the time stability of the system is analyzed in low power and high power regimes.

- Chapter 3 deals with the fundamental model describing the interaction of a single mode resonator with its vertically coupled bus waveguide. In order to provide the most clear comprehension of the peculiar properties endowed by this configuration, a more in-depth analysis to the other common coupling configuration (i.e. in-plane coupling) is presented in Section 3.1. Section 3.2 introduces the vertically coupled resonator in its geometry and fabrication process, showing the challenging steps to achieve a proper device and summarizing the positive features and the limitations offered by this technique. The developed theoretical model is fully presented in Section 3.3, with particular attention to the gap and wavelength dependences of the model: indeed, observation of these two features evidences the actual differences between vertical coupling and in-plane coupling configurations. Finally, validation of the wavelength dependence is carried out throughout Section 3.4.2, where experiments performed on a device are compared with the predictions from the model.

- In Chapter 4 the investigation moves to multimode resonators. Indeed, the multimodal operation of the microresonator, combined with the peculiar position of the waveguide in the vertical geometry, gives rise to intermode coupling characterized by both reactive and dissipative components. Section 4.1 contains a general introduction to the subject of coupled systems and a more focused description of the reactive coupling observed in the specific case of vertically

coupled resonators. In Section 4.2 the theoretical model proposed in [13] is presented and a different formulation is proposed. Section 4.3 contains the experimental validation of the model through simultaneous acquisition of the phase and transmittance data. In particular, at first, comparison of the experimental data with the theoretical ones confirms the correct description of the system that is given by the model. Secondly, the analysis of the experimental data demonstrates that a precise definition of the coupling dynamics is possible only when both the phase and the transmittance spectra are acquired. Finally, an experimental result is used to evidence the importance of using an interferometric setup in the analysis of a microresonator response.

- Chapter 5 treats another peculiar phenomenon generated by the backscattering of photons inside the resonator cavity. This phenomenon results in the appearance of a resonator mode travelling in the opposite direction with respect to the waveguide-excited mode. The excitation of this counterpropagating mode is mainly due to sidewall roughness of the microresonator and its experimental evidence is the presence of a resonance doublet in the spectrum. This last feature is due to the lift in energy of the two standing waves that are created inside the cavity by the interference of the two propagating and counterpropagating modes. In this Chapter we propose a new model, which takes into account the multimodal nature of a resonator to justify the presence of asymmetric doublets in the resonator spectrum. More in detail, in order to get familiar with the phenomenon of backscattering in microresonators, Section 5.1 contains a review of the different models present in the literature and highlights the relevant contributions that have been identified in the creation of the asymmetric doublet. In Section 5.2, the proposed model is explained: the new contributions, the considered approximations and the quantities characterizing the doublet are described. The successive section (Section 5.5), starting from phase and transmittance measurements, introduces new methods for the identification of a backscattering generated doublet and for the evaluation of its asymmetry. Section 5.3 contains the results of 2D simulations on singlemode and multimode resonators to verify the assumptions of the model. Finally, in Section 5.4, a Pump and Probe experiment performed on a vertically coupled resonator is discussed. Fitting of the experimental data confirms the goodness of the model and the observation of the doublet at different wavelengths shows oscillations of the unbalance up to 40% of the total transmittance. An explanation to this experimental evidence is provided and qualitative agreement with simulations is demonstrated.

- Chapter 6 deals with the bistable behaviour that is observed in a microresonator in high power conditions, due to the mutual coupling of thermal and optical effects. In Section 6.1, a general introduction to the thermo optic effect responsible for the system bistability is given. Then, Section 6.2 focuses on the

common model of a thermo-optically driven microresonator. Section 6.3 discusses the experimental results on a vertically coupled resonator and compares them to the theoretical predictions from the model.

- Final conclusions summarizes the results presented throughout the thesis and presents some future advances that could be reached.

Personal contribution

Since nowadays the research is mainly the result of the joined efforts of several people working together in a laboratory, I provide here a description of my involvement on the different Chapters of the thesis:

- Chapter 2: I directly contributed to the implementation of the setup in all its components and I personally performed its characterization;
- Chapter 3: starting from the results presented in [14], I have both acquired the data and developed the theoretical model for the wavelength dependence;
- Chapter 4: I contributed to both the development of the model from [13] and to the acquisition of the experimental data; this is a collaborative work carried out with two colleagues (Fernando Ramiro-Manzano and Stefano Biasi);
- Chapter 5: I mainly contributed with the simulations and partially with the development of the theoretical model and with the analysis of the experimental data; this is a collaborative work carried out with two colleagues (Fernando Ramiro-Manzano and Stefano Biasi);
- Chapter 6: I developed the simulations and acquired the experimental data.

Chapter 1

Introduction

1.1 Waveguides

Semiconductor waveguides have been firstly proposed as the building blocks of an integrated photonic circuit by Miller in 1969 [15], and that initial idea paved the way for the birth and evolution of nowadays integrated photonic networks. Since then, several kinds of waveguide have been created, proposed and exploited in integrated photonic circuits to channel light from one point to another in the circuit. Strip, strip loaded and slot waveguides (see Figure 1.1[1]) are only few of the several proposed geometries [16, 17, 18, 19].

Despite the countless variety of employed shapes and materials, this basic element is commonly driven by the same steady and simple working principle, namely, Total Internal Reflection (TIR)[2]. The TIR phenomenon, which allows to confine a light beam in a finite geometry, is schematically represented in Figure 1.1(right): the presence of a material with high refractive index n_2 (the waveguide core) surrounded

[1] Mode profile throughout the thesis are simulated with Comsol® software

[2] Actually, light guiding can be achieved exploiting different physical principles from TIR: plasmonic waveguides [20], hybrid-plasmonic waveguides [21] and photonic crystal waveguides [22] are some alternatives to common waveguides.

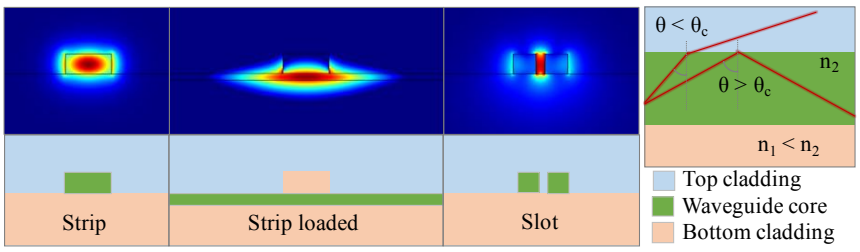

Figure 1.1: (left) Simulated modes and schematic geometries of (from left to right) strip, strip loaded and slot waveguides; FEM simulations have been carried out at $\lambda = 1.55\,[\mu m]$ with Si waveguides ($n = 3.5$) on a Silica substrate ($n = 1.44$) and air as top cladding; strip waveguide dimensions are $220nm \times 500nm$. (right) Schematic representation of the Total Internal Reflection principle.

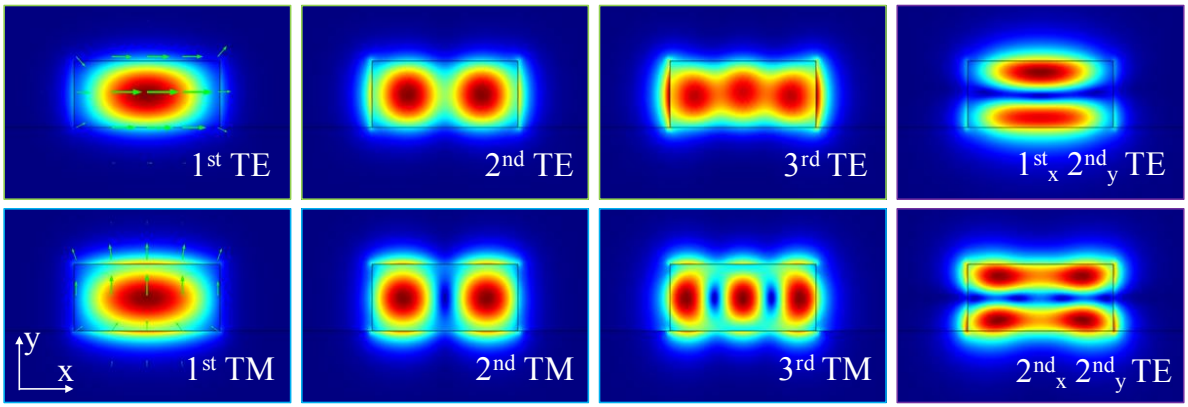

Figure 1.2: Simulated waveguide modes for a $1.1\mu m \times 0.5\mu m$ Silicon waveguide at $\lambda = 1.55\,[\mu m]$: the electric field arrows in the 1^{st} TE and TM modes evidence the difference between the two polarized modes. High order vertical modes are also guided thanks to the large height of the waveguide.

by a material with lower refractive index n_1 (the waveguide cladding) forces the beam to bounce back inside the core each time it reaches the waveguide walls (see Figure 1.1(Right)). As it is widely known, this effect holds only for beams arriving on the waveguide wall with an angle θ greater than the critical angle $\theta_c = \arcsin(n_2/n_1)$, which results in $n_2 > n_1$ to have a guided beam. In order to describe more in detail the propagation of an optical beam along a semiconductor waveguide, the wavy nature of electromagnetic radiation must be taken into account.

Indeed, the electric field component of an electromagnetic plane wave travelling along a waveguide can be described as: $E(x, y, z) = E(x, y)e^{-i\beta z}$ where z is the propagation axis, $E(x, y)$ is the electric field profile along the waveguide cross section and β is the propagation constant of the wave [23]. The accepted values for β and the corresponding profiles of $E(x, y)$ can be found by solving the Helmholtz equation for $E(x, y)$:

$$\left(k_0^2 n^2(x, y) - \nabla_{xy}^2\right) E(x, y) = \beta^2 E(x, y) \tag{1.1}$$

where n is the refractive index of the materials and k_0 is the wavevector of the propagating wave. Equation 1.1 can be seen as an eigenvalue equation with β and $E(x, y)$ as eigenvalues and eigenvectors. Therefore, discrete values for the propagation constants β_m comes out as natural solutions of the equation, with as many again related profiles $E_m(x, y)$. These two quantities (β_m and $E_m(x, y)$) describes the guided modes, each one identified by integer numbers called *mode numbers* (m_x, m_y).

In Figure 1.2 the profile of $E_m(x, y)$ for different modes is shown as computed with a Finite Element Method (FEM) software which solves and propagates local Maxwell equations. As shown in the figure, many modes are present and more than one mode number is needed to univocally identify them. In particular two mode numbers should be used to indicate the horizontal (m_x) and vertical (m_y) profiles,

with $l = m-1$ indicating the number of nodes in the profile, here the electric field goes to 0. A third symbol must be added to describe the polarization of the propagating field. Indeed, waveguide modes with an electric field component oscillating in the horizontal/vertical direction are said Transverse Electric/Magnetic (TE/TM) modes, respectively. They can show very different behaviours due to their different field distribution, as shown in Figure 1.2. The TE and TM modes with mode number $m = 1$ do not show any node in their field profiles and they are called the *fundamental* modes of the waveguide. Since common waveguides can usually sustain only the fundamental vertical mode ($m_y = 1$), because higher order modes are not guided due to their high attenuation coefficients, only the horizontal mode number is considered and modes are described as $1^{st}TM, 2^{nd}TE$,etc... The electric field profile $E(x, y)$ associated to each mode is not confined within the waveguide core, but it extends into the cladding material. More precisely, in the case of a symmetric slab waveguide ($E(x, y) = E(y)$, the field profile can be described with a cosine function inside the waveguide core and with a decreasing exponential function at the cladding level [23]:

$$E_m(y) \propto \begin{cases} \cos\left(\frac{2\pi}{\lambda}\sin\left(\theta_m\right)y\right) & m = even \\ \sin\left(\frac{2\pi}{\lambda}\sin\left(\theta_m\right)y\right) & m = odd \end{cases} \quad (core)$$

$$E_m(y) \propto \begin{cases} \exp\left(-\gamma_m y\right) & y > 0 \\ \exp\left(\gamma_m y\right) & y < 0 \end{cases} \quad (cladding)$$

where the parameter $\gamma_m = \sqrt{\beta_m^2 - n_2^2 k_0^2}$ is the extinction coefficient. The exponentially decaying field outside the waveguide is also called *evanescent field,* and it represents the part of the field most sensitive part to the outer environment. Indeed, coupling of light from one element to the other takes advantage of this field tail and allows different structures to be used such as directional couplers and resonators.

The other parameter characterizing a mode, i.e. the propagation constant, can be written as $\beta_m = k_0 n_{eff,m}$ where $n_{eff,m}$ is the effective refractive index of the *m-th* mode and, in general, is a complex quantity. In the following, linear propagation of a light beam is considered; a brief discussion of beam propagation inside a nonlinear media can be found in Chapter 6 or, more extensively, in several books [24, 25, 26]. In the linear case, the imaginary part of n_{eff} ($\hat{n}_{eff}$) deals with wave attenuation: the intensity of every waveguide mode decreases exponentially with the propagation length, following the Lambert-Beer's law: $I(z) = I_0 e^{-\alpha z}$, where I_0 is the initial intensity and $\alpha = 2k_0\hat{n}_{eff}$ is the attenuation constant. The sources of losses contributing to an increase of α can be very different, from material absorption to surface scattering, to radiative losses when bent waveguides are considered [27]. The real part of n_{eff} ($\bar{n}_{eff}$) is related to the mode propagation speed along the waveguide. Indeed, the phase velocity of the propagating mode is found to be: $v_{p,m} = \frac{c}{\bar{n}_{eff,m}}$ while the group velocity is obtained as:

$$v_{g,m} = \frac{d\omega}{d\beta_m} = \frac{c}{\bar{n}_{eff,m} + \omega\frac{d\bar{n}_{eff.m}}{d\omega}} = \frac{c}{\bar{n}_{eff,m} - \lambda\frac{d\bar{n}_{eff.m}}{d\lambda}} = \frac{c}{n_{g,m}} \tag{1.2}$$

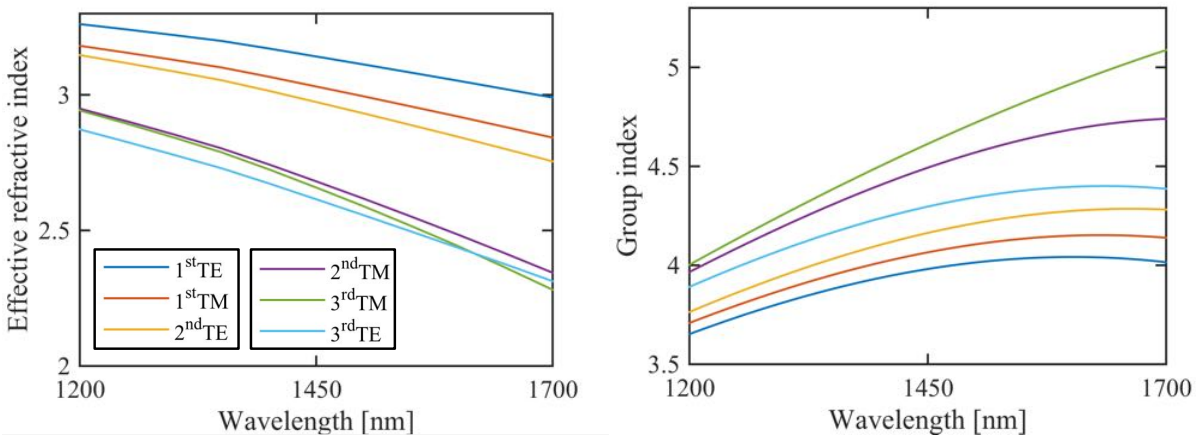

Figure 1.3: Simulated effective index (left) and group index (right) of waveguide modes shown in Figure 1.2. Effective index intersection observed at about 1650nm for high order modes evidences their different dependence on wavelength.

where $n_{g,m}$ is the modal group refractive index. Examples of $n_{eff,m}$ and $n_{g,m}$ for different modes propagating in a common strip Silicon waveguide are shown in Figure 1.3 as a function of the wavelength. In a naive view of the waveguide properties, the n_{eff} parameter can be thought as a weighted refractive index between the core and the cladding ones ($n_{cladd} < n_{eff} < n_{core}$). The weights depend on the distribution of the optical mode inside and outside the waveguide core. A mode highly confined in the core possesses an effective index similar to the bulk core one and, conversely, a very low confinement is associated to modes showing an effective index near the cladding bulk index. As a consequence, the waveguide parameters (γ, β, n_g, *etc.*.) depend on the waveguide geometry, on the materials (core and cladding) and on the wavelength. This last dependence is due to the wavelength dependent refractive indexes and to the lower confinement achieved at higher wavelengths.

In addition to these parameters one can compute the Group Velocity Dispersion (GVD) of a mode as: $GVD_m = \frac{d^2\omega}{d\beta_m^2} = -\frac{2\pi}{\omega}\frac{d^2\bar{n}_{eff}}{d\lambda^2}$ which becomes an important parameter when wideband propagation occurs [28]. Other parameters that can be extracted from the field distribution are the field confinement factor and the effective modal area [29]. The confinement factor is described as :

$$\Gamma_m = \frac{\iint_{core} n^2(x,y)E_m^2(x,y)dxdy}{\iint n^2(x,y)E_m^2(x,y)dxdy} \tag{1.3}$$

and gives a more quantitative description on the amount of field propagating inside the waveguide core. The effective modal area can be written as:

$$A_{eff,m} = \frac{\left(\iint E_m^2(x,y)dxdy\right)^2}{\iint E_m^4(x,y)dxdy} \tag{1.4}$$

and describes the spreading of the mode outside the waveguide core. These pa-

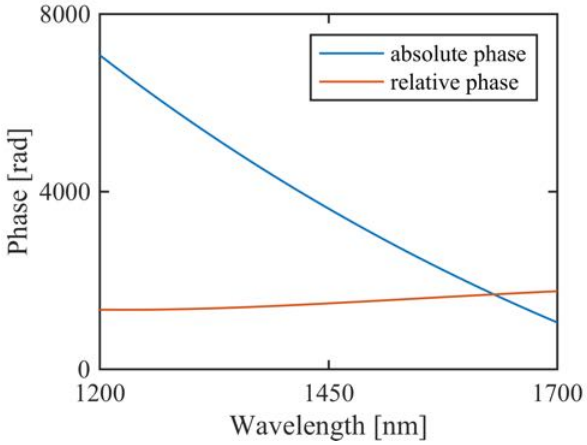

Figure 1.4: Absolute and relative phase for the 1^{st} TE mode shown in Figure 1.2 after 1mm propagation. The relative phase is obtained from the comparison with a reference phase coming from 1mm propagation in bulk Silicon.

rameters become important when nonlinear processes are considered, because a field propagation inside the active element (i.e. the waveguide core) is a desirable condition to increase the efficiency of the process [30].

Finally, also the phase φ_m of a propagating mode can be extracted from the effective index, being $\varphi_m(z) = \arg(E(z)) = \beta_m z$ where z is the travelled length. The phase dependence on wavelength for a Si waveguide is shown in Figure 1.4 for a propagation length of 1mm. As it appears from the figure, a strong phase variation with wavelength is observed: this is due to the long optical path, which enhances the small wavelength variation thousand of times. A possible way to decrease this phase dependence and stabilize its value is to compare it to a reference line where a material with similar refractive index to the one of the guided mode is used. In this way the difference between the reference and the investigated phases is less wavelength dependent, as shown in Figure 1.4 (in the figure the same core material but in its bulk form is used). This small dependence is needed when experimentally probing a device and it is commonly adopted in interferometric measurements, where the signal from a reference arm is combined with the one coming from the sample arm to achieve a relative phase variation. This technique is employed in all the phase measurements presented in the thesis and a more detailed explanation is contained in Appendix A.

1.2 Microresonators

1.2.1 Materials and geometries

Several kinds of microresonators have been fabricated, showing different shapes, materials and dimensions. Fused silica toroids and microspheres, integrated microrings and microdisks (Figure 1.5) and many other resonating geometries have been ideated

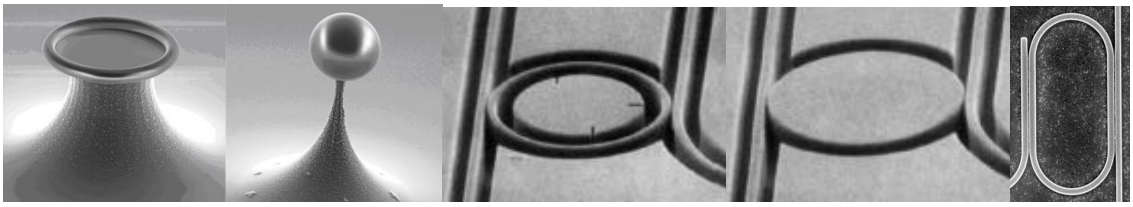

Figure 1.5: SEM images of different microresonator geometries: (from left to right) toroid, sphere, ring, disk and racetrack. Images taken from [32, 33, 34].

for the study of fundamental phenomena as well as for their implementation in a photonic chip. Among the group IV most used materials for microresonators we find Silica, Silicon and Silicon based materials such as Silicon Nitride (SiN), Silicon Oxynitride (SiON) and Hydex [1, 31].

1.2.2 Working principle

The most simple representation of a microresonator is a circular waveguide looped back on itself. Propagation of a light beam inside the resonator is driven by the same principle described for the waveguide and, as for waveguides, the first order vertical modes are usually the only guided modes. Therefore, only the horizontal mode number (m_x) is used and it is called the *radial* mode number (due to the circular geometry of the system). The peculiar property of a microresonator is the possibility to accumulate light, just as it happens in the cavity of a common Fabry-Perot resonator. This can be achieved only when the resonant condition is met:

$$l\lambda = L_{eff} n_{eff} \tag{1.5}$$

where l is an integer number called the *azimuthal* mode number, λ is the circulating wavelength and $L_{eff} = 2\pi R_{eff}$ is the resonator effective length . This latter usually does not coincides with the geometrical perimeter of the resonator. Indeed, as it will be shown in Section 3.3.2, the resonator modes propagate at a radius R_{eff}, different from the resonator one.

Equation 1.7 states that, when the optical path length equals an integer number of the incoming wavelength, the input wave reproduces itself after a roundtrip and a complete constructive interference of several waves is found. Therefore, when the resonant condition occurs, the system accumulates energy in the resonating radial mode. Different resonant modes are usually grouped in families of modes, each one containing modes with different azimuthal number l but with the same radial mode number m. For this reason they are called the *m-th* radial mode order family.

In the case of a racetrack resonator (Figure 1.5) the presence of an extended coupling region modifies the resonant condition: $l\lambda = L_{eff} n_{eff} + 2L_C n_{eff_C}$, where L_C and n_{eff_C} are the length and effective refractive index of the directional coupler, respectively.

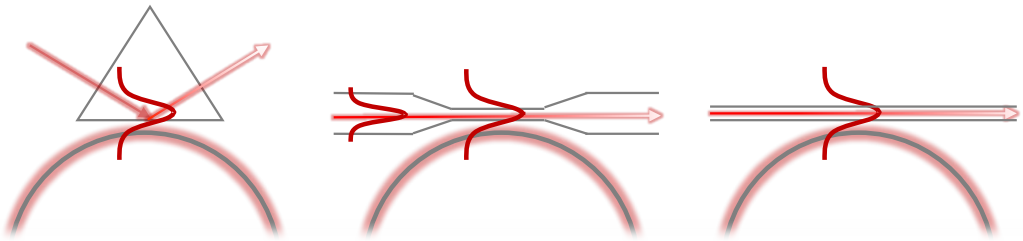

Figure 1.6: Schematic representation of different coupling techniques: (from left to right) prism, tapered fiber and waveguide based coupling.

1.2.3 Light coupling

In order to optically probe the properties of a resonator, a light signal is injected to and extracted from the resonator through a coupling element (a waveguide in our case). The coupling principle takes advantage of the evanescent field of guided modes, which propagates outside the coupling element. When the waveguide approaches the resonator, part of this evanescent tail couples to the cavity supported mode and the optical signal is transferred to the resonator or leaks out from it. At this point, when the resonance condition is met, the continuous external excitation from the coupling element leads to power enhancement inside the resonator. On the basis of this principle, several coupling configurations have been exploited (see Figure 1.6), each one presenting specific features that can be used in different applications. As an example, prism coupling has been proven to be a useful approach when silica microsphere resonators are used, because of its easy implementation in a freespace setup and its fine tuning of the coupling distances. [35]. Another very commonly adopted coupling scheme consists in moving a tapered silica fiber near to the resonator edge. In this way the low confinement obtained along the tapered region of the fiber combined with the short gap between the two elements allows light to be coupled to the resonator. This technique is frequently used in the test of freestanding devices, such as Silica microspheres, toroids or microdisks [36, 37]. Indeed, the possibility to move the coupling element both in the horizontal and vertical directions allows the best coupling configuration to be found with any freestanding device. However, this coupling technique presents also some drawbacks: for example, the circular crossection of the fiber makes the lateral coupling to a planar resonator difficult to be achieved. In addition, the possibility to move the fiber along the diverse directions is provided by piezo electric movimentation, which usually causes larger instability of the coupling element and represents an additional noise source. Finally, another relevant disadvantage is the not-integrated nature of the fiber, which prevents CMOS fabrication of the whole device to be achieved. A common alternative to this approach is the use of an integrated waveguide. In this case in-plane and vertical configurations provide excellent light coupling for both planar and freestanding devices, with nanometric precision on the gap size [9, 38]. Moreover, the stable coupling conditions produced with the integrated fabrication diminish the coupling related noise.

An important feature to take into consideration when coupling light to a microresonator is phase matching. This term refers to momentum conservation and it becomes particularly relevant in the case of nonlinear processes (e.g. in the case of Second Harmonic Generation (SHG) or Four Wave Mixing (FWM) processes) where it plays an important role in defining the efficiency of the nonlinear generation [39, 40, 25]. The phase matching condition for light coupling corresponds to require the wave vector of the photons into the waveguide and into the resonator to be identical. This is particularly important in racetrack resonators, where the long range coupling becomes effective only when the two waves propagating in the directional coupler travel at the same phase velocity, i.e. with matched phase profiles [41]. Also in the case of Silica spheres, coupling related phase matching has a relevant contribution to determine the final coupling coefficient. In this sense, an interesting and detailed treatment of phase matching for prism and tapered fiber coupling in microspheres can be found in [42]. For what concerns in-plane point coupling with integrated microresonators, the assumption of a point coupling region due to the low radius and the employment of similar resonator and waveguide materials reduces the dependence of coupling efficiency on phase matching. Actually, a more important coupling parameter in this configuration is the overlap between the waveguide mode and the resonator mode. Finally, phase matching in vertically coupled structures can be treated as in racetrack resonators: as explained in Chapter 3 light coupling occurs on a distributed region and can be described with similar terms used for a directional coupler.

1.2.4 Theoretical model

Regardless of the kind of coupling, the excitation of a microring resonator is described as a point interaction: the exchange of energy is thought to happen only at a given point, which is usually placed in the middle of the coupling region, where the gap is minimal. This fact is not true for the vertical coupling case, and Chapter 3 explains the origin of this difference.

A general model explaining the coupling and thus the dynamics of a singlemode microresonator was described by Stokes in 1982 [43], which considers the coupling region as a directional coupler with two input and two output ports (see Figure 1.7). Energy conservation at the coupling stage requires the coupling coefficient k and the transmittance coefficient t of the directional coupler to satisfy: $k^2 + t^2 = 1$, where negligible coupling induced losses are considered. Using Transfer Matrix Formalism [44] the electric field at the output ports of the directional coupler can be described as:

$$\begin{bmatrix} E_3 \\ E_4 \end{bmatrix} = \begin{bmatrix} t & ik \\ ik & t \end{bmatrix} \begin{bmatrix} E_1 \\ E_2 \end{bmatrix} \tag{1.6}$$

where $E_1 \neq 0$ indicates the waveguide excitation field amplitude. The presence of the resonator forces the power at the resonator output to be:

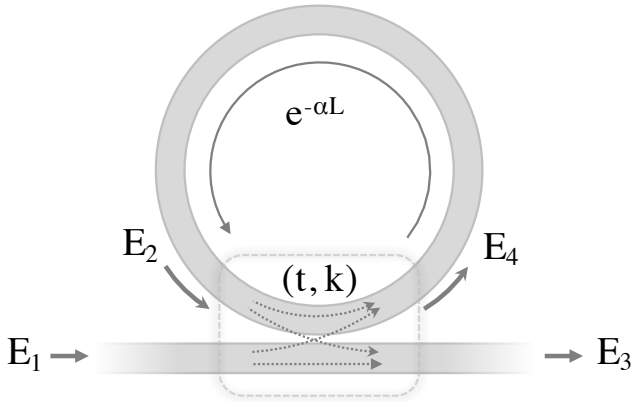

Figure 1.7: Sketch of the theoretical model of a coupled microresonator with the coupling region depicted as a 2x2 port directional coupler.

$$E_2 = E_3 e^{-\alpha L} e^{i\beta L}. \tag{1.7}$$

where $L = 2\pi R$ is the effective resonator length already described. Indeed, a wave propagating along the resonator diminishes exponentially its amplitude due to the intrinsic losses (the loss coefficient $\alpha(\lambda)$ being always positive[3]) and changes its phase depending on the propagation constant β. The parameters α and β in a more general form should be written as $\alpha_{m,l}$ and $\beta_{m,l}$ to evidence their dependence on the guided mode order m and on the azimuthal mode number l. Coupling light from the waveguide to the resonator does not only affects the spectral width and depth of the resonance, but also its spectral position: the propagation constant $\beta_{m,l}$ and, thus, the effective index n_{eff}, depend on the environment. As it will be shown in Chapter 4, the waveguide position modifies the propagation constant of the resonating mode: being made of a different material from the cladding it alters the refractive index of the resonator environment and it brings to a shift of the resonances which is as much large as the waveguide approaches the resonator.

The model is valid also for a racetrack resonator, with only few differences: the directional coupler length constitutes an additional parameter to tune the coupling coefficients k and $t$contained in Equation 1.6; the attenuation and propagation of the electric field along the resonator described in Equation 1.7 should be modified as follows: $E_2 = E_3 e^{-(\alpha_R L_R + \alpha_C 2L_C)} e^{i(\beta_R L_R + \beta_C 2L_C)}$, where two contributes are highlighted, one coming from the straight propagation along the directional coupler (C subscript) and one from the curved elements (R subscript). L_C and $L_R = \pi R$ are the length of the directional coupler and of one curved element, respectively. With these modifications also the results presented below can be applied to racetrack resonators.

Substituting Equation 1.7 into Equation 1.6, the solution for the field amplitudes

[3] $\alpha > 0$ is here assumed because passive and lossy devices are studied. For completeness, when $\alpha < 0$ (i.e. for active devices) power amplification occurs, which can bring to signal amplification and lasing [45].

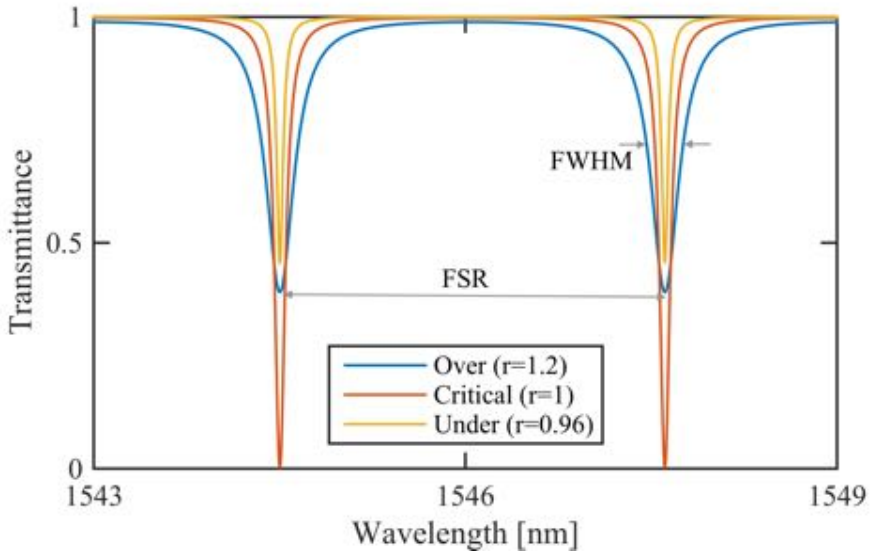

Figure 1.8: Transmittance spectrum of a $70\mu m$ radius SiN microresonator ($n_{eff} = 1.75$ at $1.55\mu m$) as obtained from Equation 1.8 for three different coupling regimes identified by the parameter $r = \tau/t$.

E_3 and E_4 in stationary conditions can be found. Then, the transmittance can be computed as:

$$T = \left|\frac{E_3}{E_1}\right|^2 = \left|\frac{\tau - te^{-i\beta L}}{1 - \tau te^{i\beta L}}\right|^2 \tag{1.8}$$

where $\tau = e^{-\alpha L}$ is the roundtrip attenuation coefficient. On resonance (i.e. for $\beta L = 2\pi$) Equation 1.8 becomes:

$$T = \left|\frac{E_3}{E_1}\right|^2 = \left|\frac{\tau - t}{1 - \tau t}\right|^2 \tag{1.9}$$

In Figure 1.8 the transmittance response obtained from Equation1.8 is shown with the typical peaks associated to resonator resonances. Depending on the ratio $r = \tau/t$ between the attenuation coefficient and the transmittance coefficient, three different coupling regimes can be identified (in Figure 1.8 the coupling coefficients are tuned and the roundtrip attenuation coefficient is fixed to $\tau = 0.95$). Indeed, when $r < 1$ the resonator is said to be in the *under* coupling regime. The word indicates the lower losses that are associated to the coupling process (extrinsic losses) with respect to the one associated to light propagation inside the microresonator (intrinsic losses). In this regime the device spectrum is mainly driven by the internal losses and its transmittance shows narrower resonances. The opposite case is found when major losses are associated to coupling ($r > 1$) and the spectrum results in wider resonances. The in between situation is found when the two channel of losses equals ($r = 1$) and the resonator falls in the *critically* coupled regime. This condition is

easily recognized from the spectrum, which shows dips with null transmission.

More in detail, the spectral shape of the resonances shown in Figure 1.8 is a Lorentzian lineshape (with a unity offset). This can be easily seen performing an expansion of Equation 1.8 near the resonance condition (i.e. for $\lambda = \lambda_r + \delta\lambda$, with λ_r satisfying Equation 1.5). The resulting transmittance is:

$$T(\delta\lambda) = 1 - \frac{(1-t^2)(1-\tau^2)}{\left(2\pi n_{eff}\frac{\delta\lambda}{\lambda^2}\right)t\tau + (1-t\tau)^2} \tag{1.10}$$

which is a Lorentzian function of $\delta\lambda$. The quantities $1-t^2$ and $1-\tau^2$ can be related to the coupling and intrinsic losses of the resonator, respectively. With some mathematical elaboration of the above equation, an expression for the resonator *Free-Spectral-Range (FSR)* and the resonance *Full-Width-at-Half-Maximum (FWHM)* $\triangle\lambda$ can be reached [46, 47]:

$$FSR(\lambda) \sim \frac{\lambda^2}{2\pi R n_g(\lambda)} \tag{1.11}$$

$$\triangle\lambda = \frac{(1-t\tau)\lambda^2}{\pi n_g(\lambda)\, 2\pi R\sqrt{t\tau}} \tag{1.12}$$

where n_g is the group index defined in Equation 1.2. The FWHM of a resonance allows to compute the quality factor Q of the device:

$$Q = \frac{\lambda}{\Delta\lambda} \tag{1.13}$$

which represents the average number of oscillations the propagating wave makes inside the resonator perimeter. Despite Equation 1.13 can be used to experimentally infer the Q factor of the probed structure, another description of the Q-factor allows a more clear connection of this quantity to the device properties. Indeed:

$$Q = \frac{2\pi c t_c}{\lambda} = \frac{2\pi c}{\lambda\alpha_c} \tag{1.14}$$

Thus, knowing the Q factor, one can obtain the average lifetime a photon spends inside the resonator t_c, or the attenuation rate $\alpha_c = 1/t_c$.

Several loss channels can contribute to increase the attenuation of a microresonator and they are usually divided into intrinsic and extrinsic ones. Intrinsic losses consist of material absorption, bending losses (also called radiation losses), scattering losses and surface absorption [27], while the extrinsic losses are mainly represented by coupling losses. Interestingly, when a resonator is found in critically coupled regime ($\alpha_i = \alpha_e$), an experimental value for the intrinsic losses can be achieved, being: $Q = [1/Q_i + 1/Q_e]^{-1} \underset{Q_i=Q_e}{=} Q_i/2$, where $Q_{i/e} \propto 1/\alpha_{i/e}$ are the intrinsic/extrinsic quality factors, respectively.

Another useful parameter to be computed is the Field Enhancement factor (FE), which indicates the field magnification occurring inside the resonator volume:

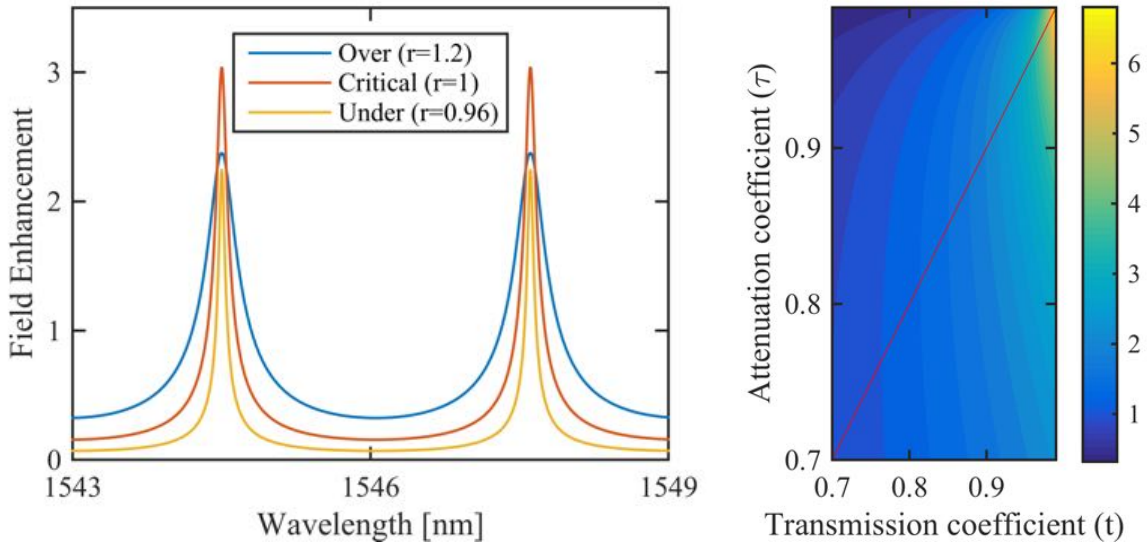

Figure 1.9: (left) Field Enhancement for a microresonator as found from Equation 1.15 for three coupling regimes already investigated in Figure 1.8 and (right) FE for different attenuation and transmission coefficient with the maximum values highlighted in red.

$$FE = \left|\frac{E_4}{E_1}\right|^2 = \left|\frac{it\tau e^{i\beta L}}{1 - k\tau e^{i\beta L}}\right|^2 \tag{1.15}$$

The presence of a strong field inside a small volume is a peculiar property of microresonators, which makes them suitable elements for the observation of nonlinear effects at low input powers [48]. In this sense, an essential step to properly exploit the optical power accumulation produced by the resonator is a correct selection of light coupling parameters. Indeed, coupling of light inside a resonator highly affects both the internal power enhancement and the obtained output power, and thus represents one of the most important parameters to take into account in the design and test of microresonators. In Figure 1.9 the FE occurring inside a SiN resonator is shown for the three different regimes (system parameters are the same used to create the data shown in Figure 1.8). As it appears from the three curves, the larger enhancement is achieved for critical coupling conditions; this fact is confirmed by Figure 1.9(right), where the FE at different coupling coefficients t and attenuation coefficient τ is represented: the maximum FE for every coupling coefficient is evidenced by the red line and it is obtained for $\tau = t$. The same result can be reached looking at the resonator stored energy [27]:

$$U_c = \frac{Q_i \lambda}{2\pi c}(1 - T)P_{in} \tag{1.16}$$

where the maximum energy for a fixed input power P_{in} occurs when the transmittance drops to its lowest value (i.e. 0 in critical coupling). From Equation 1.16 also

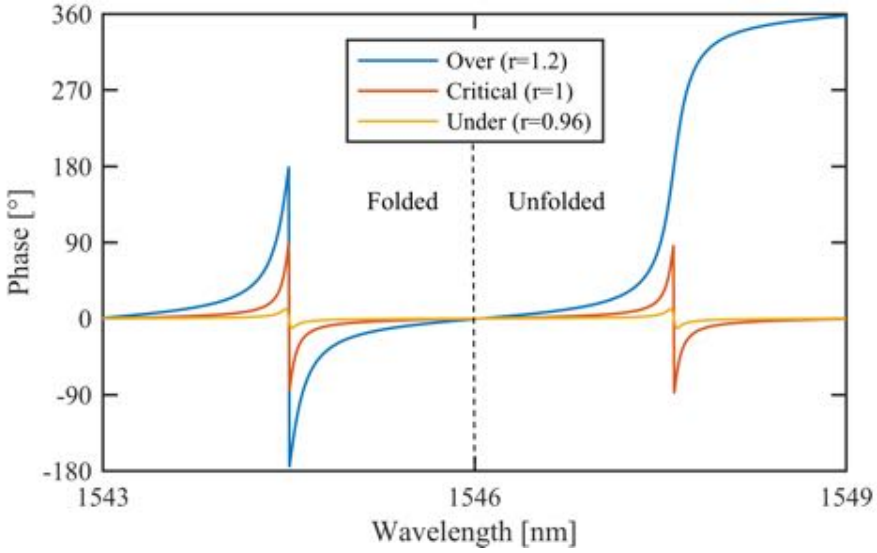

Figure 1.10: Folded and unfolded phase spectra of a microresonator as obtained from Equation 1.17 with the same system parameters used in Figure 1.8.

the role of the internal quality factor becomes clear. Indeed, a higher Q_i provides larger circulating energy, and thus favors the appearance of nonlinear phenomena and decreases their threshold power.

From these considerations the importance of a proper coupling is evident. In this sense, with the observation of the phase response of a resonator a deeper understanding of the coupling dynamics can be achieved. Indeed, the optical phase delay accumulated by the electrical field when travelling along the device can be easily computed as:

$$\varphi = arg\left(\frac{E_3}{E_1}\right) = \pi + \beta L + \tan^{-1}\left(\frac{t\sin(\beta L)}{\tau - t\cos(\beta L)}\right) + \tan^{-1}\left(\frac{t\tau\sin(\beta L)}{1 - t\tau\cos(\beta L)}\right) \quad (1.17)$$

Folded and unfolded phase spectra for three different coupling regimes are shown in Figure 1.10. The difference observed between the two visualizations is only apparent: an electromagnetic wave shifted forward in phase by $\pi$is identical to the same wave shifted backwards of the same quantity (i.e. $-\pi$); similarly, when the wave reaches 2π shift it regain its initial shape. In the following the folded visualization is used because experimental phase values are found in between $\pm\pi$, as explained in Section 2.2.5.

Looking at the folded spectra in the three coupling regimes, different behaviours can be recognized: the phase of an undercoupled resonator is always found between $\pm\pi/2$ and it feels no shift on resonance, while the overcoupled one shows values up to $\pi/-\pi$ on resonance. An explanation to this fact lays in the coupling dynamics, which brings to the final signal. Indeed, the waveguide output field E_3 is obtained

from the interference of two signals, the one transmitted from the waveguide and the one coupled back from the loaded resonator:

$$E_3 = rE_1 + itE_2 \tag{1.18}$$

the complex unity i at the resonator output being due to the additional $2(\pi/2)$ phase shift felt by the field when crossing (two times) the coupling region between the two elements. As a consequence to this additional shift, the two outgoing waves (from the resonator and from the waveguide) always interfere destructively. On resonance, in undercoupling regime the major contribution to the output intensity comes from the waveguide not shifted field, whose larger amplitude cancels the weaker field from the resonator. A null final phase shift between the on and off resonance signals is then found. In the opposite case (overcoupling) a greater contribution to the output field is coming from the resonator, thus showing a net $\pm\pi$ shift on resonance. In the boarder case of critical coupling, a precise value for the phase on resonance cannot be determined due to the absence of a signal ($T = 0$) and thus shows a discontinuity passing from $-\pi/2$ to $\pi/2$. The out of resonance response shows a more complicated behaviour because the not achieved resonance condition (Equation 1.5) produces a variable shift between the two outgoing waves, with the not coupled one increasing its weight as the input laser gets off resonance. Far from resonance the phase in the three regimes reaches the same null shift, as expected from a signal not coupled to the resonator.

This simple analysis evidences the advantages offered by phase measurements when a correct identification of the resonator coupling regime is needed. Indeed, the transmittance spectrum does not show an equal net difference between under and overcoupled peaks. As an example, a comparison between Figure 1.8 and Figure 1.10 shows that similar transmittance minima can be found even when the phase clearly indicates that opposite regimes are present.

Another important quantity that can be computed with a phase spectrum is the group delay $\tau_g = \frac{d\varphi(\omega)}{d\omega} = -\frac{2\pi\lambda^2}{c}\frac{d\varphi}{d\lambda}$, which physically describes the time delay accumulated by a light pulse when crossing the system. In Figure 1.11 the group delays for the three coupling regimes are shown. A larger delay is achieved when the resonance condition is met in critical/overcoupling condition due to the additional time spent by the light beam while propagating along the resonator. This property is currently exploited in the creation of integrated delay lines for coincidence measurements or in the implementation of all-optical buffers [49, 50, 51]. Interestingly, the phase delay found for an undercoupled device can assume positive and negative values: this is a counterintuitive result, which seems to suggest a superluminal propagation of the light beam. However, several debates on this subject brought to prove this odd observation as a manifestation of the wavy nature of light: the group and phase velocity of a signal (which can actually be higher than c) are not related to the information carried by that signal [52, 53, 54]. Despite this fundamental controversy, a more practical approach aiming at creating an efficient delay line requires a precise control

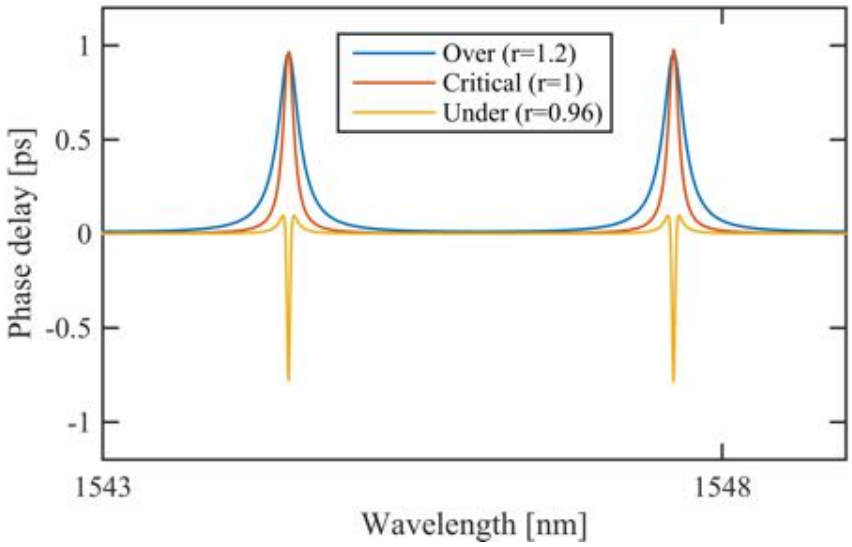

Figure 1.11: Phase delay of a microresonator for different coupling regimes.

of the bandwidth. Indeed, overcoupled resonances should be preferred to obtain a flat response due to their larger FWHM. In this sense, an additional parameter to consider are resonator intrinsic losses: low loss microresonators produce larger delay times and seem to be preferable structures. However, the small bandwidth associated to high Q resonators limits their application in delay lines. An already exploited solution is to use cascades of overcoupled resonators [49]: the bandwidth remains the single resonator bandwidth, but the total delay is increased by the multiplication of n single delay times (n being the number of cascaded resonators).

1.3 Phasor representation

When phase (φ) and transmission (t) responses of a device are simultaneously measured, an interesting representation can be exploited. The real and imaginary parts of the outcoming electromagnetic wave can be described as:

$$Re(E) = |t|\, cos(\varphi) \qquad Im(E) = |t|\, sin(\varphi) \tag{1.19}$$

and condensed in the phasor diagram representation widely used in electronics.

The phasor angle is related to the phase response of the device, while its transmittance is described by the phasor radius. This representation is useful in the analysis of several optical phenomena such as Fabri-Perot interference [55], but it becomes an even more interesting tool when resonating devices are studied. Indeed, the condensed information of phase and transmittance allows an ease discrimination of the different coupling regimes to be achieved.

The phasor plot in Figure 1.12 gathers the two spectra of Figure 1.8 and 1.10 (replotted for ease of visualization) through Equation 1.19. As it appears from the

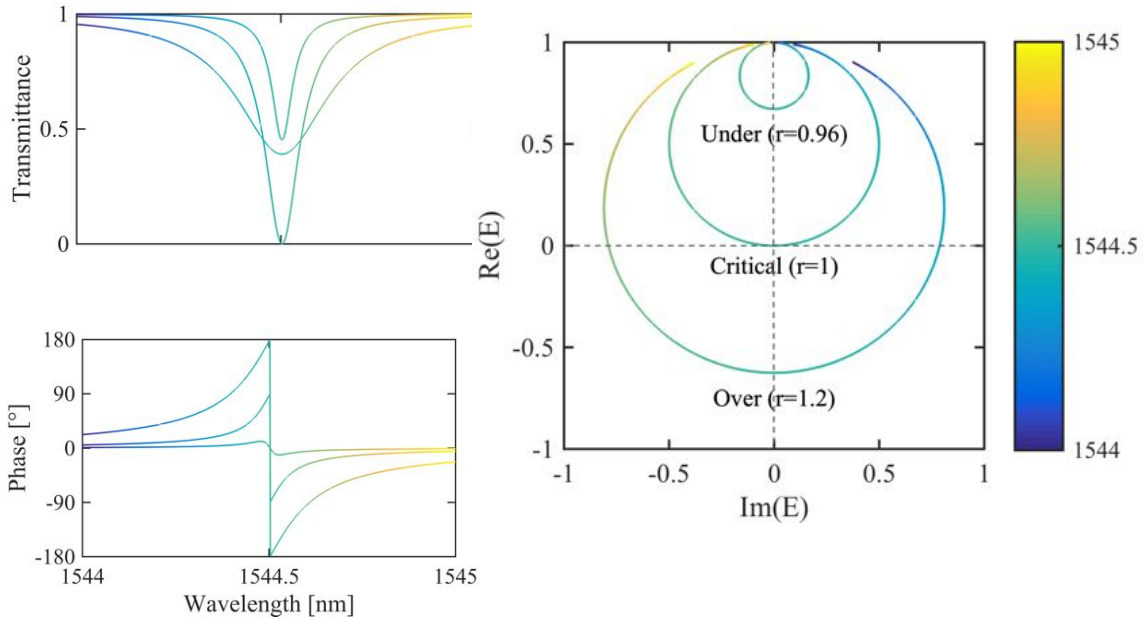

Figure 1.12: (left) usual separated transmittance and phase spectra of a microresonator and (right) condensed phasor plot in the three coupling regimes.

plot, a circular phasor curve is associated to each resonance. However, a more careful analysis highlights a clear difference between under and over coupled resonances. In the first case the related phasor shows an always positive real component, while in the second case the circle crosses the imaginary axis and a negative real component of the phasor is found (i.e. at a given wavelength). This simple analysis holds for any resonance, even in the case of multiple coupled modes (see Chapter 4 and 5) where a common spectrum representation becomes less intuitive. Actually, a relevant drawback of the phasor representation is the loss of information on wavelength, which can be roughly described by the color of the phasor curve, as in Figure 1.12.

This brief introduction on the properties of waveguide and resonators highlights the complementary information carried by phase and transmittance measurements on a microresonator, and makes clear the deeper investigation that is made possible when both these two quantities are observed. Before going into details on the physics that has been studied with this combined approach, we present in the following Chapter the experimental set up that has been specifically implemented to perform simultaneous phase and transmittance measurements.

Chapter 2

Interferometric setup

2.1 Phase measurement in integrated devices

Among the different techniques that can be used to obtain the phase of a propagating optical signal, interferometry is the most common one. Integrated Mach-Zehnder Interferometers (MZI) have been widely implemented in photonic integrated circuits for fast and ease test of the devices [56]. Moreover, the high phase sensitivity of interferometric measurements has been exploited also in biosensing devices, where integrated MZI constitutes mature sensing elements [57, 58, 59]. Despite commonly used, this integrated approach presents some drawbacks. At first, it requires preliminary design of the device, which should include an interferometer on each element that is going to be tested, with a consequent increase of the device footprint and an increment in the source of error for the fabrication process. Secondly, even if this approach allows phase and transmittance to be measured on the same device with proper use of splitters, it could suffer from bandwidth limitations due to the presence of directional couplers [60]. Y splitters can also be used to increase the bandwidth, but they usually introduce high losses in the photonic circuit. Actually, alternative techniques have been proposed to avoid the design of specific structures inside the tested devices. A solution proposed by Gifford et al. [61] relies on Fourier Transform analysis of orthogonally polarized optical signals in what is called an Optical Vector Network Analyzer. Another approach by Mas et al. [62] relies on modulation of the optical signal inside the interferometer arms. Slightly different modulation frequencies in the two arms produce beating of the interference signal, which can be analyzed with a lock-in amplifier to extract the phase information. Both these methods are suitable for passive characterization of photonics component and they can be used in a wide wavelength range.

In order to enlarge the features offered by interferometric measurements and deepen the investigation on resonating structures, we built a free-space setup able to capture simultaneously the phase (φ) and the amplitude (T) of a transmitted light beam, which propagates in a photonic device (Figure 2.1(center)).

In addition to this feature, the implemented setup is also provided with a filtering

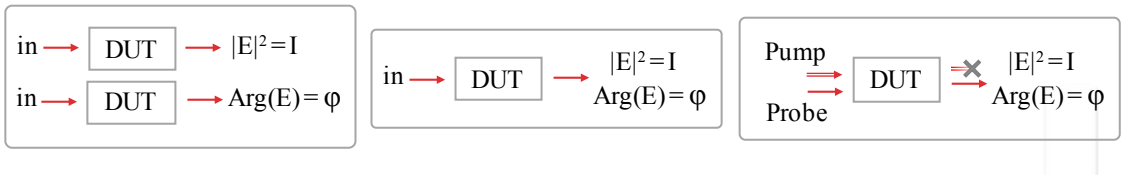

Figure 2.1: Schematic representation of the information available by interferometric measurements. The most common approach (left), where separate measurements are carried out to obtain amplitude and phase, is substituted with the presented one (center), which acquires phase and amplitude simultaneously and allows standard phasor representation to be exploited; (right) in addition, Probe phase and amplitude can be extracted in a degenerate Pump & Probe experiment without any optical filtering stage; DUT=Device Under Test.

stage which makes it an ideal platform for degenerate Pump & Probe experiments, i.e. when the Pump and the Probe signals have the same wavelength. The system is able to filter out a Pump beam three orders of magnitude stronger than a Probe signal (Figure 2.1(right)) without the need of specific optical filters.

In the following sections, a complete description of the features offered by this setup and the demonstration of the above mentioned properties are provided. In particular: in Section 2.2 a detailed description of the setup is given; Section 2.3 shows few experiments performed on different integrated waveguide samples and highlights the crucial features of the setup; finally, Section 2.4 summarizes the results of the characterization and presents some possible improvements.

2.2 Setup description

The different parts constituting the setup (see Figure 2.2), namely, the Preparation, Interference and Detection stages, are described in Section 2.2.1, 2.2.2, 2.2.3, respectively. The two acquisition modes used to extract the optical phase are explained in Section 2.2.4 and the influence of external unwanted sources of noise on the system is discussed in Section 2.2.5.

2.2.1 Preparation stage

The preparation stage (Figure 2.2(top)) creates and manipulates two optical signals: the Probe and the Pump signals.

In particular, the Probe signal is provided by a fiber pigtailed Continuous Wave Tunable Laser (CWTL) operating in the IR range (1490-1610 nm) at a maximum power of 10mW. The laser beam undergoes an intensity modulation by an optical chopper wheel at a modulation frequency of about 1kHz. This modulation allows the readout of the signal from a lock-in amplifier at the detection stage (see Section 2.2.3 below). To avoid mechanical noise from the motor, the chopper has been placed

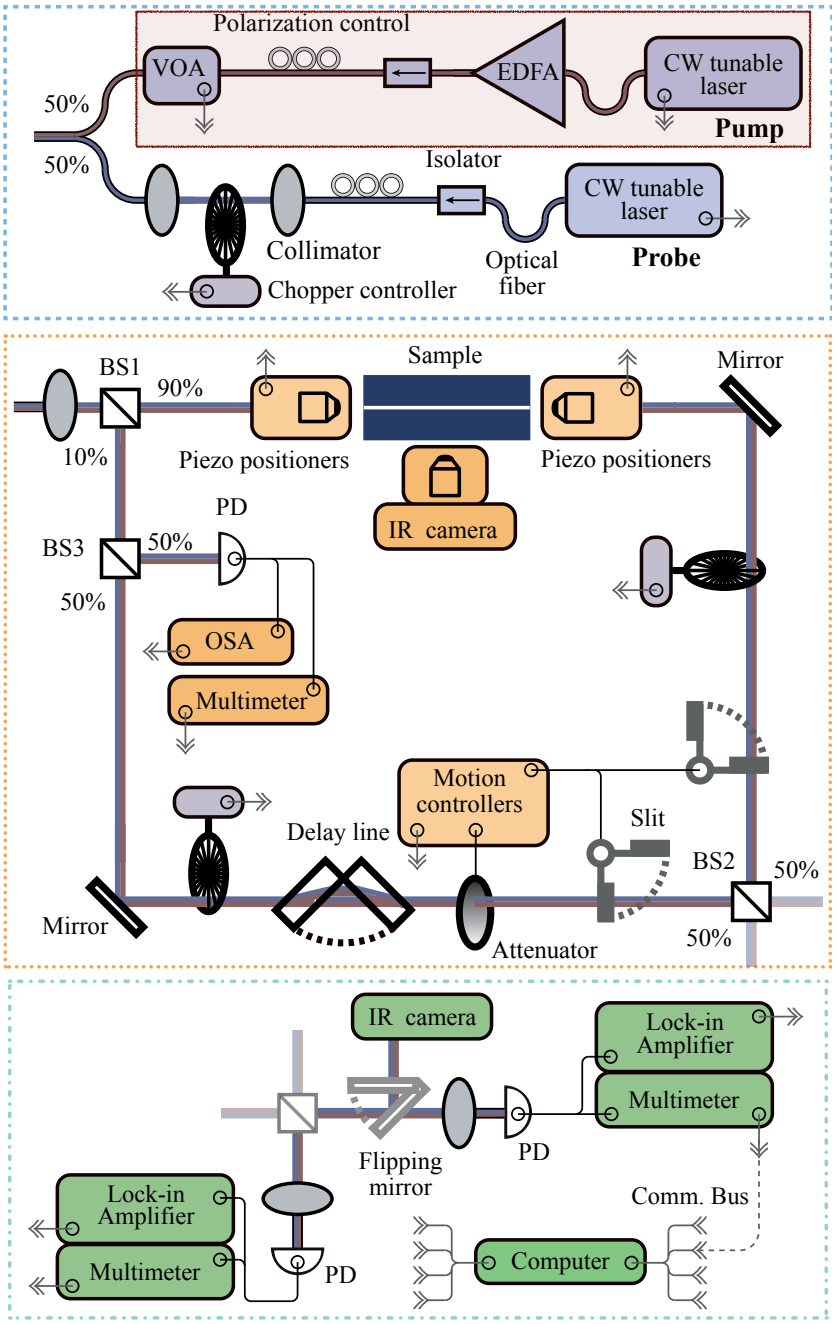

Figure 2.2: Sketch of the experimental setup; (top) Preparation stage: CW=Continuous Wave, EDFA=Erbium-Doped Fiber Amplifier, VOA=Variable Optical Attenuator; the Pump (shaded area) and Probe laser beams are polarized and then attenuated with the VOA (Pump) or modulated through the chopper wheel (Probe); (center) Interference stage: BS=Beam Splitter, OSA=Optical Spectrum Analyzer; PD=PhotoDetector; the beam coming from the preparation stage is split in two beams, one crossing the sample and one travelling in free space, both of them encountering modulation and attenuation components along their path to the second beam splitter where recombination occurs; (bottom) Detection stage: the combined beams are acquired by two Germanium PD (only one is shown) and the modulated Probe signal is revealed by the filtering action of the Lock-in Amplifier. Several communication buses allow to remotely control the instruments via computer. The connected instrumentation shows the symbol ↠

outside the optical table containing the interferometer.

Despite the setup can operate with only this Probe source, for example to characterize passive devices, a second laser beam can be coupled to realize Pump & Probe experiments. The Pump signal (shaded box in Figure 2.2) consists of a fiber pigtailed CWTL, whose output is amplified by an Erbium Doped Fiber Amplifier (working wavelengths 1535-1565 nm) resulting in a high power signal (5W maximum). This passes through a Variable Optical Attenuator (VOA), provided with remote control, and then it is coupled to the modulated Probe via an integrated 2x1 (50/50) fiber optic coupler.

Polarization and isolation stages are present for both the Pump and the Probe signals in order to select the desired optical mode polarization (TE/TM) and prevent laser damage, respectively.

The Probe beam can be used alone or with the Pump one, depending on the experiment. When only the Probe signal is used, the Lock-in amplifier basically contributes in reducing the noise of the measurements. When both the Pump and the Probe signals are sent through the interferometer, it acts as a filter for the Pump signal and it allows to isolate the information carried by the weak probe. Remarkably, the filtering efficiency does not depend on wavelength and the Pump can be filtered out also when degenerate in wavelength with the Probe signal (see Section 3.3, a result that can not be obtained with optical filters.

2.2.2 Interference stage

After the first stage, the two fiber coupled signals are sent through a collimator, which constitutes the starting point of the second stage. The interferometer is a MZI (Figure 2.2(center)). The device under test (DUT) is placed on one of the two arms of the interferometer, between two objectives equipped with xyz piezo-positioners for correct alignment. Objectives are here used since we mostly deal with silicon photonics where the waveguides have small cross-sections ($\backsim \mu m^2$). An IR camera on top of the sample allows for direct observation of the sample. Let us call the arm with the tested device *the sample arm* and the one without *the free arm*. Finally, a chopper wheel and an open/closed shutter are present on each arm. They allow two different acquisition modes to be used (see Section 2.2.4 below). A 90/10 cube beam splitter is used at the initial splitting stage of the interferometer to partially compensate for the coupling losses at the sample stage, which can be as high as 20dB depending on the sample. In order to minimize these losses, an active control of the alignment is also present: simultaneous movement of the objectives and acquisition of the transmitted Probe power allows to maximize the signal output and to find the best configuration for the measurement. Fine tuning of the optical power is possible also along the free-arm, thanks to a tunable attenuator provided with remote control. A third beam splitter (BS3) allows for continuous power measurement and spectrum acquisition by means of a photodetector and an Optical Spectrum Analyzer (OSA), respectively. In order

to balance the different dispersion in the two arms, a delay line made of a series of movable glasses is inserted. Indeed, the delay perceived by light when travelling along the sample arm is wavelength dependent due to the dispersion of the involved media. The same delay can be reproduced with the insertion of a similar material in the other arm, where precise dimensioning of the material thickness allows to reduce the phase dependency on wavelength. A detailed explanation of this phenomenon and a simple model to describe it are given in Appendix A.

Total losses occurring to the Probe and to the Pump along the optical line up to the sample alignment stage account for 18dB and 12dB, respectively, the Probe making an additional free-space step at the preparation stage to be modulated by the chopper wheel.

2.2.3 Detection stage

Once the signal is recombined by the second beam splitter, it enters the detection stage where it is acquired by two Germanium PhotoDetectors ((PD), only one shown in Figure 2.2(bottom) for ease of visualization). At this point, the Pump continuous beam, when used, generates the DC component of the electrical signal, which is measured with a multimeter; at the same time, the modulated Probe creates a modulated electrical signal, which can be extracted with a Lock-in Amplifier and measured with an oscilloscope. Alternatively, a flipping mirror can deviate the optical signal to an IR camera to verify the correct superposition of the two beams coming from the free-arm and from the sample arm. This is a necessary condition to optimize interference and, thus, reduce phase errors.

2.2.4 Acquisition modes

The system output consists in three different signals: one coming from the sample (I_S), one from the free-arm (I_0) and one from the interference between the two (I). From these quantities the phase difference ($\Delta\varphi$) accumulated by light when travelling through the sample with respect to the free arm can be obtained. Indeed one can easily see that:

$$I = I_0 + I_S + 2\sqrt{I_0 I_S}\cos\Delta\varphi \tag{2.1}$$

Manipulation of the above equation allows to evidence the relevance of an accurate power balancing of the two arms. Indeed, being:

$$\Delta\varphi = cos^{-1}\left(\frac{I - I_0 - I_S}{2\sqrt{I_0 I_S}}\right) \tag{2.2}$$

it comes out that a system with equal powers for I_0 and I_S minimizes the experimental error on $\Delta\varphi$. Moreover, the larger slope of the $\cos^{-1}$ function at the boarder of its domain (i.e. -1 and 1) brings to a lower accuracy of the extracted phase values when $\Delta\varphi$ is about 0 or 180 degree. The above considered equations are valid for the

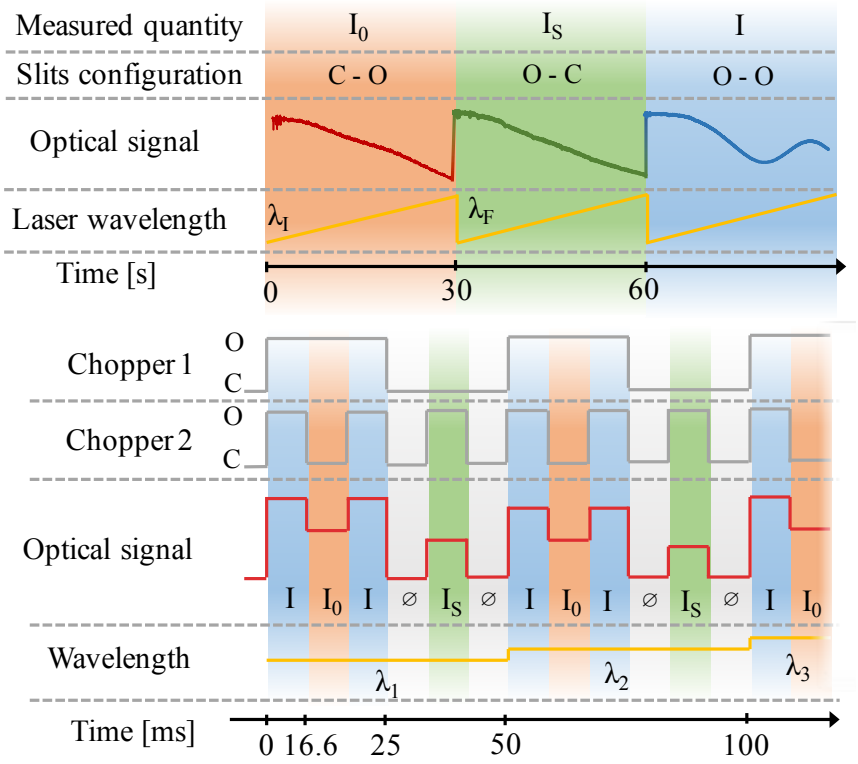

Figure 2.3: (top) acquisition procedure in *normal* mode: the three different quantities I_0, I_S and I are acquired along three identical continuous scans of the laser wavelength thanks to the different configuration of the two shutters; O=Open C=Close; (bottom) acquisition procedure in *choppered* mode: proper configuration of the two chopper wheel frequencies (20Hz and 60Hz for Chopper 1 and Chopper 2, respectively) provides a modulation of the optical signal which contains information about the three required quantities; wavelength step scan (one per each period of Chopper 1) allows recreating the phase and transmittance spectra.

in-phase component of the Probe signal. The presence of two Ge detectors allows to observe also the quadrature component of the Probe signal; in this case the *cos* function should be substituted with the *sin* function in Equation 2.1, due to energy conservation.

In the described setup, the three signals I_0, I_S and I can be acquired with two different methods, called *normal* and *choppered*, whose operating principles are schematically represented in Figure 2.3. In *normal* mode operation (Figure 2.3(top)) three repeated scans of the laser wavelength are performed and different configurations of the two movable shutters (open-closed, closed-open and open-open) are used to select at each scan the desired quantity I_0, I_S or I. Measurement of closed-closed configuration is also possible if a reference noise spectrum is needed. In this acquisition method, the two chopper wheels inside the interferometer stay in open position and do not play any role in the measurement. On the other hand, in *choppered* mode the two wheels are driven at multiple frequencies (20 Hz and 60 Hz in our system)

and the movable shutters are fixed in the open-open configuration. This working configuration allows the acquisition of the three signals for each wavelength while slowly scanning the Probe wavelength, as depicted in Figure 2.2(bottom). Indeed, the choice of multiple frequencies creates a final signal which brings information on all the three quantities.

Both methods present advantages and limitations. In *normal* mode, on one hand, fast and wide range wavelength scans can be performed. For reference, 100 nm scan with 20 pm resolution takes less than 3 min. On the other hand, accuracy on wavelength and power is not assured because the laser response can vary within the three repeated scans, thus introducing an error source in the system. This effect becomes detrimental when unstable lasers are used or when small features, such as narrow resonances, are studied, because they are highly influenced by wavelength variations. In these situations, the *choppered* mode constitutes a better measurement procedure. Indeed, the simultaneity of the measurement is assured within one chopper period (50ms in our case), increasing accuracy in wavelength and power. Simultaneity reduces also the influence of the environment conditions (mainly air temperature and flux), whose variation can be considered negligible within 50ms. The drawback of this procedure is the time needed for the acquisition which can be up to 20 times longer than the normal one (for the same wavelength range and resolution). In the case of unstable laser wavelength, the Optical Spectrum Analyzer can be used to reconstruct the correct spectrum, with the disadvantage of a longer time for the acquisition. As a consequence, in order to exploit the good features of the two methods, long scans are usually performed in *normal* mode to observe the phase spectrum in its entirety, while its small interesting parts are studied in *choppered* mode.

2.2.5 System isolation

As it can be seen from Figure 2.2, many components of the setup are remotely driven by a PC. This fact makes the system able to perform measurement in a completely automatized mode, with several optional step on the measurement process, such as auto alingment of the sample, movement of the shutters, tuning of the *free arm* power, etc. This computer driven measurement does not only constitute a simpler tool for the experimentalist, but also allows for exact and repeatable experimental parameter selection providing stable operating conditions at each stage of the measurement.

Another important advantage connected to the use of remote control is the possibility to physically isolate the setup from external unwanted sources of noise, such as air fluxes or room temperature variations, through a closed box. This feature is essential for interferometric measurements, where even a small variation of the room temperature can influence the results. An experimental evidence of this fact is shown in Figure 2.4, where the phase signal of a resonating structure taken in isolated and non-isolated conditions is shown. From the figure, it clearly appears that a non isolated system presents larger fluctuations of the signal with respect to the isolated

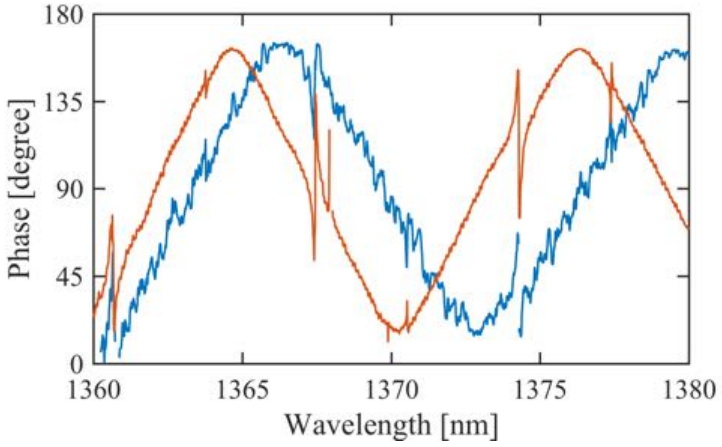

Figure 2.4: Phase spectrum of a resonating structure in (red) isolated (i.e. a closed box is placed around the optical table where the setup is mounted) and (blue) non-isolated (i.e. open box) conditions. Weak resonances are evidenced at 1364nm and 1377nm only in isolated conditions. Sample details are given in Section 2.3.2.

system. This results in a scarce or null visibility of the sharp features that characterize a device spectrum, as it happens for the resonances of the resonator, in particular at 1364 nm and 1377 nm. The slow oscillation that is observed in both signals comes from the wavelength dependent optical path, as explained in Figure 1.4. The introduction of a glass delay line reduces the phase dependence on wavelength but it is not able to cancel it completely (waveguide dispersion cannot be perfectly reproduced, apart with an equal waveguide). As a consequence, a continuous shift is observed in the measured phase, which appears as an oscillation in a real measurement. Indeed, the experimental phase is obtained from Equation 2.2 and the cos^{-1} function returns values in between 0 and π. A simple model for the description of these oscillation is explained in Appendix A. The shift in the phase between the two curves is due to the different temperature and air conditions before and after the opening of the isolating box. It is worth notice that the observed wavelength range is not covered by the CWTL commonly used in the setup and presented in the preparation stage. Indeed, the acquisition has been performed with a different low power CWTL to demonstrate the versatility of the system, which can be used over a wide wavelength range.

2.3 Setup characterization

In order to characterize the setup, we performed a series of measurements on a channel waveguide and on a disk resonator (Figure 2.5). Low and high power regimes have been investigated and time stability has been tested.

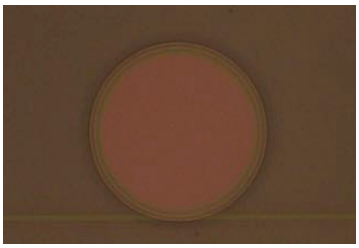

Figure 2.5: Optical image of the tested resonator with the bus waveguide visible in the bottom part of the figure; coupling of the waveguide to the resonator can be canceled out by increasing the horizontal displacement between the two structures (see 3.4 for further details). In this way the isolated waveguide response can be investigated.

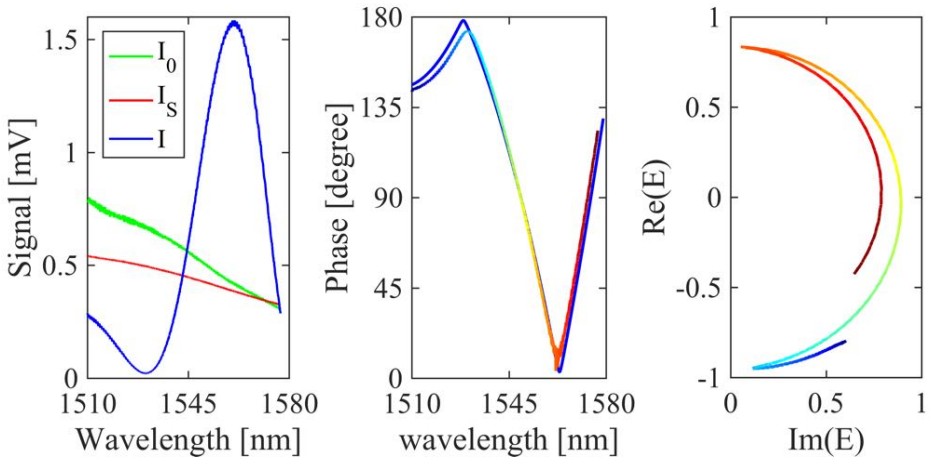

Figure 2.6: (left) Free-arm, transmittance and interference signals as obtained with the normal mode for a SiON waveguide; (center) Phase variation as found from Equation 2.2 (blue line) and from experiment (rainbow line); oscillation of the signal comes from phase folding at 0 and 180 degrees due to cos^{-1} function; (right) Phasor plot as obtained from the experimental data using Equation1.19; phasor radius is normalized to its higher value.

2.3.1 Waveguide: low power

In particular, as a first example, low power measurements have been carried out on a SiON channel waveguide with a cross section of 2.5μm x 250nm and a length of 6mm. Details on the sample can be found in [12]. In this first experiment, only the Probe signal was used with a fixed power of 5mW and the normal operating mode was selected. Indeed, the three signals presented in Figure 2.6(left) show only broad oscillating features, thus justifying the employment of the faster operating mode. The reconstructed phase difference is shown in Figure 2.6(center), together with the theoretical curve coming from the simple model described in the Appendix A, which takes into account the different dispersions and the different optical paths encountered along the two arms. Remarkable accordance between the two curves is found, with slight deviations mainly due to inexact estimation of the glass dispersion.

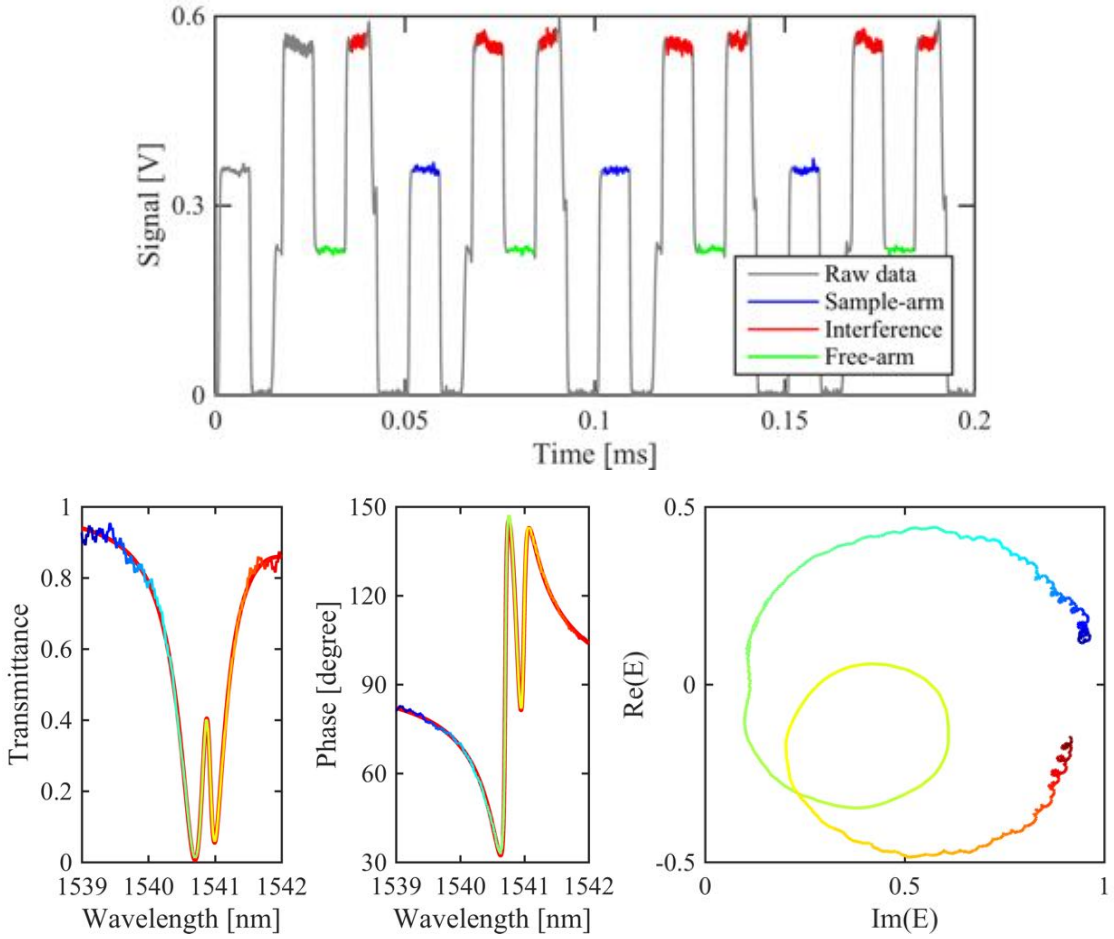

Figure 2.7: (top) Time signal measured in the *choppered* mode; the different acquisition windows are clearly visible and the three interesting quantities (I_S, I_0, I) are highlighted in different colours; (bottom-left) Transmittance spectrum, (bottom-middle) phase spectrum and (bottom-right) phasor plot of a vertically coupled SiN resonator as measured with the *choppered* mode. Fitting from the analytical model [63, 13] is also shown for the transmittance and the phase spectra (red colour).

Combining the information given by the phase and transmittance spectra through Equation 1.19, the phasor plot presented in Figure 2.6(right) can be obtained. An oscillating semicircular behaviour is characterizing the phasor plot. This is expected from a waveguide structure, where only phase variation with wavelength should be observed. Decrease of the phasor radius (i.e. transmittance intensity) is mainly due to lower sensitivity of the detector, lower power of the laser and higher propagation losses of the waveguide at longer wavelengths.

2.3.2 Resonator: low power

Maintaining a low power regime, i.e. with only the Probe laser switched on, a second measurement has been carried out to test the setup in its *choppered* mode.

The chosen device consists of a Silicon Nitride ring resonator vertically coupled to a SiON bus waveguide. Indeed, resonating structures typically show narrow resonances [64], which must be studied with great wavelength accuracy. Moreover, the peculiar intermodal coupling mechanism that has been demonstrated in these samples [13] generates a sharp Fano lineshaped response [65] which makes the device response highly dependent on small wavelength fluctuations. In Figure 2.7(top) a portion of the optical signal filtered by the lock-in amplifier is shown and the four chopper conditions for the acquisition of the interesting quantities (I_S, I_0, I) are clearly visible. Instantaneous processing of the raw data cuts the rising and falling edges of the signal, recognizes the important windows and makes the average on the values related to each quantity, providing a final set of three values for each scanned wavelength. These values allow the transmittance spectrum to be obtained (Figure 2.7(left)), the phase spectrum to be reconstructed (Figure 2.7(center)) and the phasor diagram to be represented (Figure 2.7(right)). Clear spectra are obtained thanks to the high acquisition rate, which provides more than one thousand points per each of the three signals at each wavelength. Good agreement between the fitted curve and the experimental data demonstrates the accuracy provided by the acquisition method, which is able to faithfully capture the narrow features of coupled resonating families. From the transmittance spectrum two radial families of resonating modes are clearly distinguishable, with quality factors as high as 15000. On the other hand, the phase spectrum contains information on the coupling regime of the two modes with the bus waveguide: the phase undergoes a phase shift below π ($\sim$120°) when passing the transmittance dip of the wide family indicating an undercoupling regime for that family [44]; moreover, the narrower family produces an even smaller variation of the phase, well below π, thus revealing an undercoupled regime. This analysis is also revealed by the phasor plot, where the two circles indicates the presence of the two families and the always positive values of $Im(\boldsymbol{E})$ indicates that only undercoupled resonances are present (the *sin* being lower than 0 for arguments between π and 2π, i.e. in overcoupling regime [63]). Red lines in Figure 2.7(bottom) are fitted curves based on the model described in [63, 13] which takes into account the peculiar nature of the vertical coupling. The good agreement between the two curves demonstrates the accuracy of the acquisition setup, which is able to faithfully capture the small features related to multiple resonance coupling.

2.3.3 Waveguide: high power (Pump & Probe)

In order to explore the properties of the system in the high power regime, Pump & Probe experiments have been performed on the sample studied in Section 2.3.1. The Probe laser was the same used in the low power characterization (Section 2.3.1) and its power was fixed at 5mW; the Pump wavelength was 1550 nm while its power was varied between 0mW and 2W with the *Pump power variation step* included in the pipeline. In Figure 2.8(top-left) the Pump output power, coming from the sample

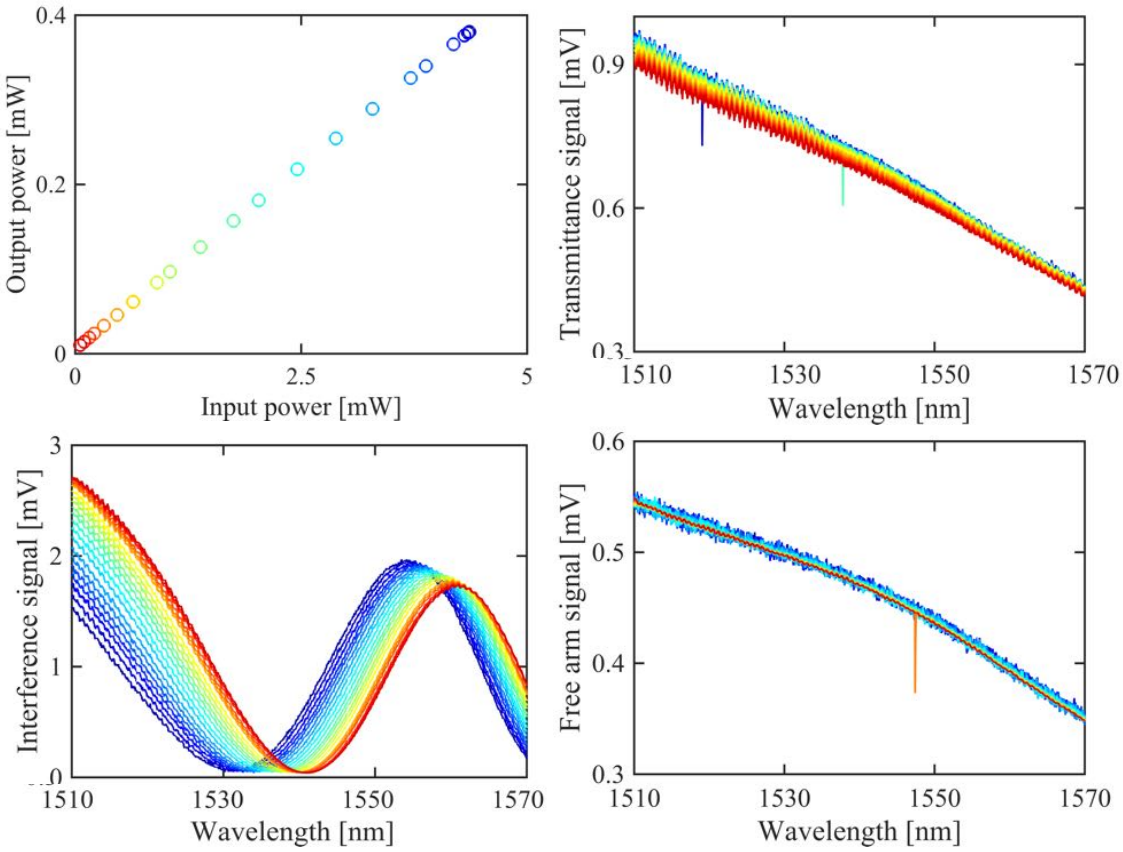

Figure 2.8: (top-left) Pump power input vs Pump power output; the input is registered from the multimeter after BS3, the output is acquired with the Germanium detector after BS2; Pump losses at BS3 and BS2 account for 23dB and 37dB respectively, where the difference between the two comes from the sample alignment stage; Probe interference (bottom-left), sample arm (top-right) and free arm (bottom-right) signals; stability of the free and sample arms allows to discard misalignment of the system as a source of phase instability; it is worth noticing that the small misalignment observed at the sample arm is not related to the Pump power.

arm and acquired at the interferometer output, is represented in its dependence on the Pump input power, as registered by the OSA. A linear behaviour is observed indicating the absence of relevant nonlinear effects induced in the sample by the high propagating power, and a stable operation of the setup. Observation of the free arm and of the sample arm signals (Figure 2.8(right)) allows to confirm the stability of the system under high power operation. Indeed, both these arms are barely influenced by the power variations. On the other hand, the interference signal (Figure 2.8(bottom-left)) shows a clear dependence on the Pump Power.

This is directly transferred to the measured Probe phase, which is shown for different Pump input powers in Figure 2.9(top). No signature of the strong Pump signal can be recognized around 1550 nm, thus demonstrating the good filtering action provided by the lock-in amplifier for Pump power as high as 200 mW (at the alignment

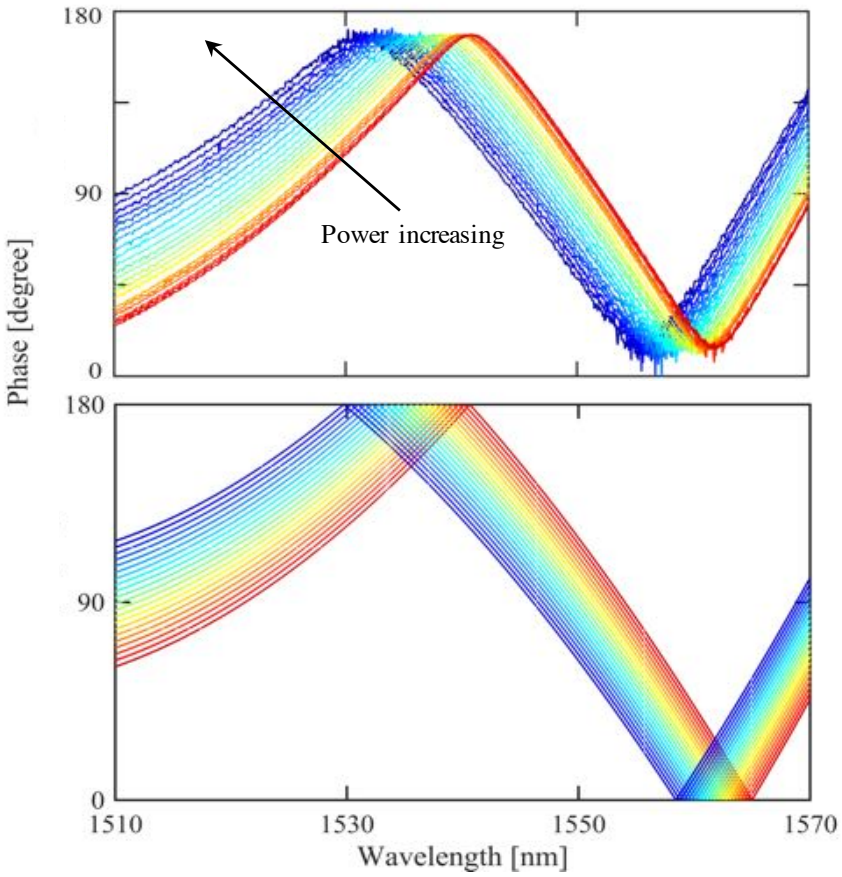

Figure 2.9: Probe phase signal at different Pump powers revealing a pronounced dependence on Pump input power: (top) experiment and (bottom) simulation from the model described in Appendix A considering a temperature increase of the sample of 2°C.

stage). At the same time, the variation of the phase for different Pump powers indicates that some power dependent phenomenon is occurring inside the sample. Some considerations on the system under study (namely: the low nonlinear coefficient of SiON and the slow increase in the power propagating along the waveguide) suggests the thermo optic effect [66] as the most probable candidate. Indeed, the simulation presented in Figure 2.9(bottom), which takes into account the effect of a temperature variation (of about 2°C) inside the waveguide, confirms this hypothesis. The clear shift observed in the experiment is correctly reproduced by the simulated data with a slight difference in the wavelength dependence that can be ascribed to the imperfect information on the glass dispersion. A more pronounced discrepancy arises at phase domain extremes (0° and 180°) where the experimental data do not reach the upper and lower theoretical limits. This fact is likely due to the high sensitivity of the cos^{-1} function around 0° and 180° combined to a residual and spurious signal not coupled to the fundamental mode of the waveguide and not filtered by the setup. This effect is more pronounced at lower wavelengths (see Figure 2.8) due to the

higher number of guided modes. This fact is a clear limitation and improvements in this direction are ongoing. Nonetheless, it is worth notice that an accurate and precise phase measurement should not involve the extreme parts of the phase domain because the high sensitivity of the cos^{-1} function to small perturbations among the I_S, I_0 and I causes a particular increase of the noise and a decrease of the accuracy of the phase measurement. In this sense, careful positioning of the glasses in the delay line allows to change the observed value and choose the best operating condition. From a practical point of view, this is achieved with a first rough manual positioning of the glass elements. Afterwards, with the isolation box closed, a stepper motor allows to perform a fine tuning of the glass positions up to the desired phase value.

2.3.4 Time stability

The time stability of the system is tested on the waveguide already investigated in Section 2.3.1. Acquisition of the Probe phase at different times for fixed conditions on laser wavelength (1555nm) and power (5mW) allows to obtain an average phase variation in low power condition. The acquired data are shown in Figure 2.10(top) and they result in a constant phase drift of about $0.25^o/min$ and average noise of about 1^o. The time stability of the system in the Pump & Probe regime is also tested: in Figure 2.10(bottom) the time variation of the Probe signal is shown for Pump power and wavelength fixed at 1W and 1550nm respectively. The arrow at about 18min indicates the time when the Pump wavelength has been moved to 1555nm, in degenerate configuration with the Probe laser. No apparent variation on the phase behaviour is found, nor in resolution neither in time drift. Indeed, a resolution of about 1^o is observed along the whole measurement and a constant average drift of about $1^o/min$ can be recognized. This more pronounced phase variation with respect to the one found in the low power regime can be attributed to thermal responses of the sample when high power beams are injected. Indeed, a lengthening of the waveguide due to thermal expansion of about 0.3‰ per hour is sufficient to explain such a large drift.

2.4 Conclusion and perspectives

In the present Chapter an experimental characterization of an automatized interferometric setup is carried out. The setup is suitable for simultaneous phase and transmittance characterization of photonic devices both in low and high power regimes. A detailed description of the system and of its operating principle has been provided, together with its characterization in low and high power experiments. In particular, the filtering action during degenerate Pump & Probe experiments has been tested and clear extraction of the Probe signal from a three order of magnitude stronger Pump signal has been proven. As a result to these measurements, an average noise of about 1° and a phase variation below 0.25°/min have been found in low power

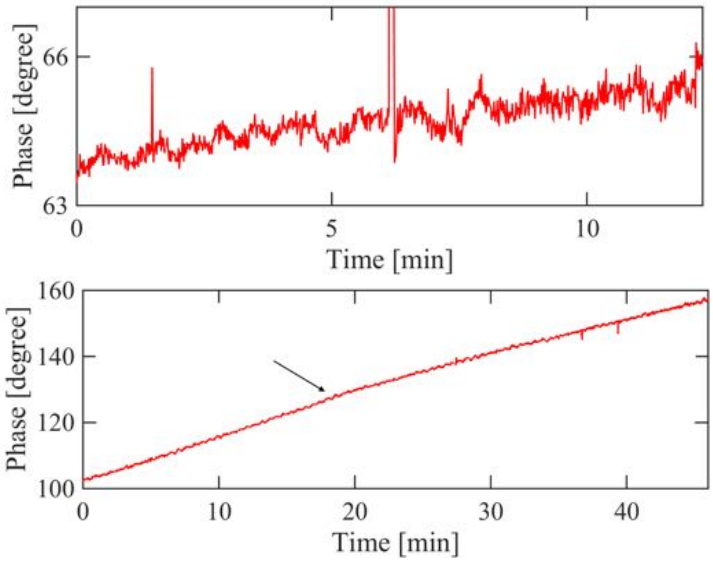

Figure 2.10: (top) Time dependence of the Probe phase in the low power regime with null Pump power incident on the sample; (bottom) high power regime measurement during Pump & Probe experiment: degenerate Pump and Probe wavelength condition occurs at $t = 18min$, with no apparent variation in phase value, resolution and drift.

regime, the latter increasing to 1°/min when high optical powers are used. Possible noise sources can be the movement of the objectives at the alignment stage and/or a not perfect isolation from the environment, which brings to weak air fluxes (in a similar way to what is observed in Figure 2.4). For what concerns the continuous phase drift, the cause of this phenomenon has not been identified yet. Temperature fluctuations of the room and, hence, of the sample can be a possible candidate, which is compatible with the large timescale of the effect. In this sense, the implementation of temperature measurement during the experiment is an important step to understand the influence of thermal fluctuations on the system response.

Some useful developements aimed at improving the efficiency of the system are also possible. These are mainly directed towards the implementation of a free-space delay line. Indeed, the glass delay line has been initially chosen as the dispersion compensating element because of its characterizing features, such as the alignment simplicity and reduced dimensions, which permit its fast and easy re-positioning in any position along the optical path. However, it carries also some drawbacks, which makes it one of the most important source of noise and accuracy in the system: in particular it is responsible for Fabri-Perot fringes in the phase spectrum and its dispersion constitutes an additional parameter in the fitting model presented in Appendix A. The free-space delay line could be a solution to these drawbacks: the absence of Fabri-Perot cavities (only reflecting mirrors are used) should diminish the delay-line associated noise and, being the dispersion of air well known in literature, the wavelength dependent interference could be easily lead back to the sample dispersion, thus resulting in a more accurate observation of the absolute phase variation

inside the tested device. Despite these possible improvements, the diverse options already offered by the experimental pipeline and the possibility to use the system with any input-output element make the system a very versatile one. Moreover, the low phase noise and the wide and tunable spectral domain (between 1100nm and 1600nm, limited by the chosen laser source and the spectral response of the employed BS) surpass those of commercially available optical vector analyzers[67]; in addition, the possibility to perform high power measurements without need of optical filters enlarges the information that can be extracted from the investigated device. Indeed, several physical phenomena have been already observed when measurements are performed with vertically coupled resonators: in particular, the new information carried by the optical phase helped to highlight the dynamics of the reactive-coupling model (see Chapter 4), to propose a model for the backscattering phenomenon (see Chapter 5) and to investigate the bistable regime occurring at high input powers (see Chapter 6).

Chapter 3

Vertically coupled microresonators

As already pointed out in the introduction, coupling of light to and from a microresonator is a crucial step for the integration of this photonic structure in a photonic integrated circuit. Indeed, the transfer function of the device is highly influenced by the interaction between the resonator and its coupling element (bus waveguide), and the possibility to fully exploit the properties of a microresonator is strongly dependent on the accurate control of the position of the coupling element. Moreover, a correct comprehension of the physical phenomena observed in a vertically coupled microresonator (see Chapters 4, 5 and 6) cannot neglect the basic coupling dynamics that drives the system. Indeed, the transfer of light to and from the resonator in a vertically coupled structure shows very different behaviour from the one observed in in-plane coupling and it deserves a detailed analysis to be carried out. Therefore, in this Chapter the peculiar geometry and the theoretical model describing light coupling in a singlemode vertically coupled resonator are presented, and an experimental validation of this model is given.

3.1 In-plane coupling model

As a first step, a more detailed explanation of the common in-plane model already presented in Chapter 1 is given, with specific attention on its dependence on waveguide-resonator distance and wavelength. Indeed, these are the more evident features that distinguish the vertical coupling from the in-plane configuration, and their discussion helps to understand the dynamics of the two systems.

As a reference model for the in-plane coupled geometry, the one proposed by Spillane et al. [68] is considered here. This model describes the coupling of light from a multimodal waveguide to a microresonator laying on the same plane. A weak coupling between the two elements is assumed and a high Q resonator is considered. Moreover, it describes the influence of the non ideal tapered fiber (due to its multimodal nature) on the resonator response by addition of a loss channel (radiative loss) at the coupling stage. In order to simplify the description, this last term (ideality) is neglected in the following analysis, considering only a single mode tapered fiber. This approximation

does not affect the results on an in-plane coupled system.

The model starts from the equation of motion for a resonating cavity proposed by Haus in 1984 [69]:

$$\frac{da}{dt} = -i\omega_0 a - \left(k_0^2 + \sigma_0^2\right) a + ik_0 s \tag{3.1}$$

An excitation field $s \propto e^{i\omega t}$ at frequency ω is coupled to the resonator via the coupling coefficient k_0. The resonator is characterized by an intrinsic loss coefficient σ_0, a resonating frequency ω_0 and a field amplitude a. As described in the introduction, the system response is obtained as the superposition of the two signals coming from the resonator and from the waveguide:

$$p = |st_0 + ik_0 a| \tag{3.2}$$

This results in a transmittance:

$$T = p/s = |t_0 + ik_0 a/s| \tag{3.3}$$

In steady state condition the on resonance transmittance, from now on called Extinction Ratio (ER), can be written as:

$$T_{res} = \left(\frac{1-K}{1+K}\right)^2 \tag{3.4}$$

where $K = k_0^2/\sigma_0^2$ is the ratio between the resonator coupled power and the resonator loss.

Depending on K, the system falls in the under ($K<1$), over ($K>1$) and critical ($K=1$) coupling conditions that have been already discussed in the introduction. From an experimental point of view, the parameter K can be tuned with two main knobs: the wavelength and the gap. Indeed, since k_0 describes the amount of light that passes from the waveguide to the resonator and vice versa, a variation in the distance of the two elements can tune this quantity[1]. More formally, the parameter k_0 depends on the distance x between the two elements as:

$$k_0^2 = \bar{k}_0^2 e^{-\gamma_0 x} \tag{3.5}$$

where $\bar{k}_0$ is the coupling coefficient at $x=0$ and γ_0 is the spatial decay rate of the system, with respect to gap variations. As it can be deduced form Equation 3.5, an increase in the distance produces a decrease in the coupling constant, as one can expect. Moreover, the exponential form of the equation makes the sensitivity of the system highly dependent on the gap and justifies the fabrication constraints that these structures require.

In Figure 3.1(left and center) the ER, and the parameters k, σ_0 are shown in their

[1]Variation of σ_0 can also affect the coupling regime and cause the same alterations produced with k_0, but an accurate tuning of this parameter in a real device is a less controllable process.

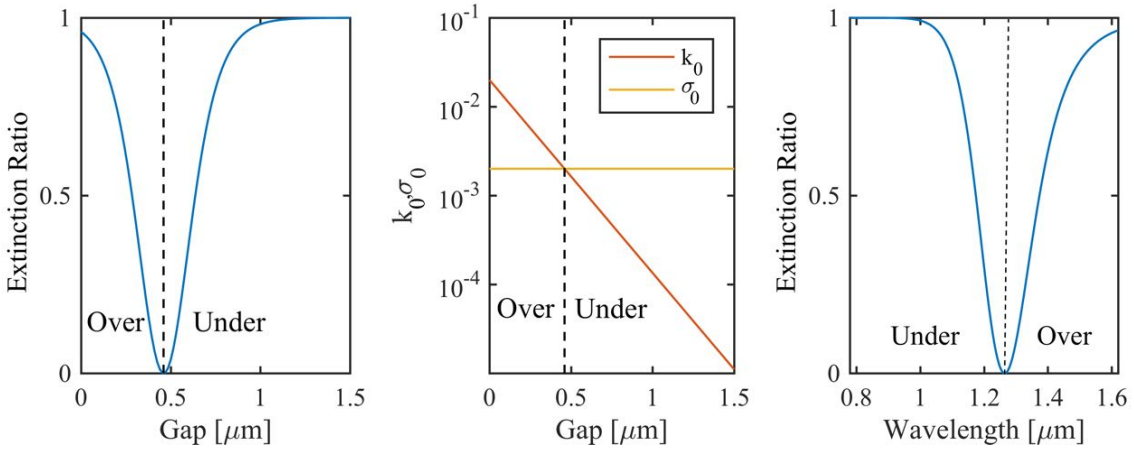

Figure 3.1: Gap dependences of the ER (left) and of the system parameters k and σ (center) for an inplane coupled resonator as obtained from Equation 3.4 and 3.5; (right) wavelength dependence of the ER for the same system; (coupling regimes are shown for clarity).

dependence on the waveguide-resonator distance, as described in Equation 3.4 and 3.5. It is important to notice here that the monotonic dependence of k_0 on the gap makes the critical coupling condition ($T_{min} = 0$) to be achieved only at a single well defined gap value. This fact is true for any coupled mode order and for any excitation wavelength, and it is a result connected to the intrinsically point like (local) nature of the coupling dynamics. A similar behaviour is found for what concerns the wavelength dependence of the coupling. In Figure 3.1(right) the simulated ER at different wavelengths is shown and it resembles the same behaviour observed for the gap variation. An intuitive picture to explain the similarity between the gap and the wavelength dependences relies on mode confinement. Indeed, the lower confinement found at higher wavelengths makes the guided mode more sensible to the environment. As a consequence, the ability to couple light inside a microresonator at a fixed distance is increased if higher wavelengths are used in a similar fashion to what happens for gap reduction. This means that an increase in the coupling strength can be achieved both by moving the waveguide towards the resonator or by increasing the incident wavelength. FEM simulation of two inplane coupled SiN waveguides (dimensions: $2.5\mu m \times 250nm$) confirms this description: in Figure 3.2 the effective index difference (Δn_{eff}) between the symmetric (n_e) and antisymmetric (n_o) supermodes of the system is represented as a function of gap (left) and wavelength (right). An exponentially decaying/growing behaviour is found for increasing gap/wavelength. As expected from the intuitive picture above presented, larger gaps or lower wavelengths weakens, exponentially, the coupling between the waveguides. The two degrees of freedom (gap and wavelength) constitute an advantage of the in-plane coupling scheme because they provide useful coupling tuning parameters, but they bring also intrinsic drawbacks to the system. Namely, the need of a very

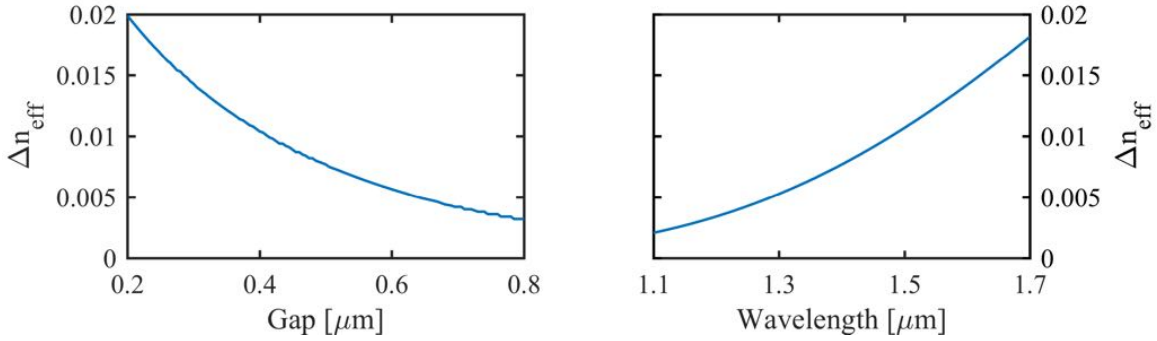

Figure 3.2: Gap and wavelength dependences of the effective index difference between symmetric and antisymmetric supermodes of two identical inplane coupled SiN waveguides (dimensions: $2.5\mu m \times 250nm$). Exponential tendencies are found in both the panels, thus justifying Equation 3.5. Wavelength and gap fixed at $1.55\mu m$ and $0.4\mu m$ for the left and right panels, respectively.

precise gap control and the lack of an efficient excitation of the resonant modes in a broad spectral region. To avoid this wavelength dependent behaviour other integrated structures have been proposed. T. Carmon et al. [70] proposed a bent fiber as the bus element to match the wavelength dispersion of the WGMr over a wide wavelength range. They demonstrate to achieve coupling at extreme wavelengths of 682 and 1540 nm, albeit with a difference of about 50% in the transmission.

Another possible solution to wavelength and gap dependences lays in racetrack resonators. In these structures a directional coupler is used as the coupling element between the bus waveguide and the resonator. The coupling coefficient of the resonator k coincides with that of the directional coupler, that is [26]:

$$k^2 = \sin^2\left(\frac{\pi}{2}\frac{L}{L_c}\right) \tag{3.6}$$

where L and L_c are the coupler length and transfer length, respectively. The latter is computed as:

$$L_c = \frac{\lambda}{2\,|n_e - n_o|} \tag{3.7}$$

and represents the needed length to completely transfer a light signal from one waveguide of the coupler to the other. The quantities n_e and n_o are the symmetric and antisymmetric supermodes of the coupler (also called *even* and *odd* from the parity of the electric field profile along the horizontal axis). In Figure 3.3, the obtained coupling coefficient for a SiN racetrack resonator at fixed coupler length is shown in its dependence on gap and wavelength (blue line). An oscillating behaviour is observed, with k reaching 0 and 1 multiple times, both in gap and wavelength. This dependence is transferred to the racetrack transmittance: in the same figure the minimum transmittance for the racetrack, computed using Equation 3.4, is shown as a function of gap and wavelength ($\sigma_0 = 0.05$). In both cases the critical coupling condition is

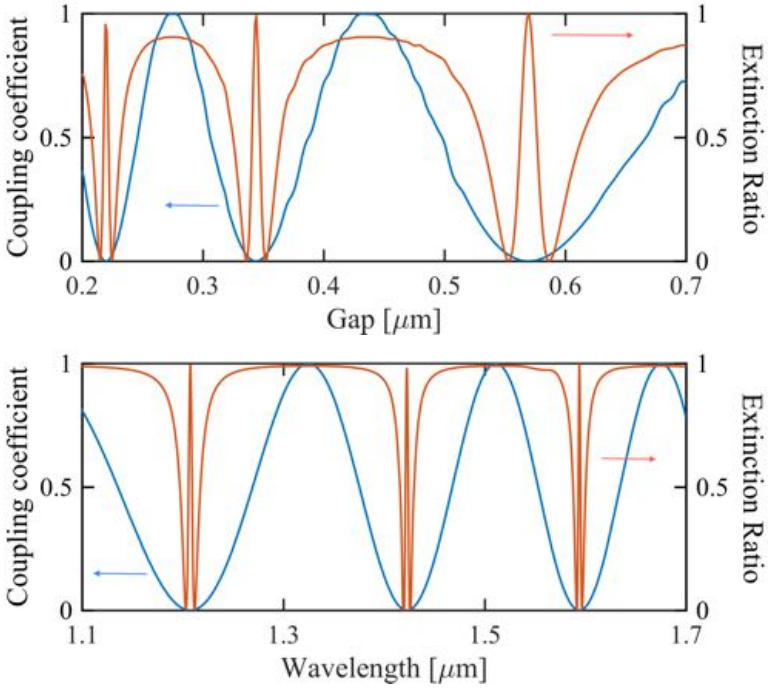

Figure 3.3: Simulated coupling coefficient (blue line) and transmittance (red line) of a racetrack resonator as computed from Equation 3.6 and 3.4 (with $\sigma_0 = 0.05$), respectively: (top) gap and (bottom) wavelength dependences for coupler length of $250\mu m$ and $340\mu m$, respectively; $1.5\mu m \times 250nm$ SiN symmetric waveguides have been considered for the resonator and the coupler.

reached multiple times, thus providing efficient coupling at multiple wavelengths and for diverse gap values. However, very sharp features are observed near the critical coupling regions, indicating low tolerance to gap and wavelength variations. Moreover, in order to achieve this situation of oscillating transmittance, a large coupling length is needed. As an example, data shown in Figure 3.3(bottom) are obtained with a coupler length of $340\mu m$, almost five times larger than the transfer length needed at $\lambda = 1.5\mu m$ ($65\mu m$). As a consequence, a marked increase in the device footprint is observed, resulting in lower FSR and requiring a more accurate fabrication process. A consistent model for directional couplers, describing the peculiar oscillating transmittance, can be obtained also from a point coupling model with a frequency dependent coupling coefficient. However, this last approach does not describe the physical insight of the directional coupler. Indeed, the observed oscillations are manifestation of the physical process ongoing in the device: a mode injected in one of the two waveguides actually oscillates back and forth between the two waveguides and the selected gap/wavelength determine the final intensity dropped in the two output. Therefore, to describe the actual system with the most faithful model, an elongated coupling region seems a more suitable choice. As a last remark, the coupling coefficient described in Equation 3.6 and the consequent transfer length do not take into account boarders effects. An accurate calculation should consider two point coupling

region, one at the input and one at the output of the directional coupler.

In the following section we present an alternative approach to in-plane structures, based on a fully integrated vertically coupled resonator. This configuration presents the bus waveguide buried below the microresonator and shows peculiar features that are not present in the common in-plane point coupling. In particular, a long range interaction is found in this structure and it results in an oscillating coupling strength both for gap and wavelength variations. This fact allows several critical coupling gaps to be present and efficient coupling of both visible (800nm) and IR (1550nm) resonant modes to be achieved on the same device. The dimensions of the system are comparable to those of common in-plane microresonators and the vertical position of the waveguide allows precise definition of the gap even without high-resolution lithography. In addition, the horizontal displacement of the waveguide is demonstrated to result in a selective excitation of high order resonator modes.

3.2 Vertical coupling: geometry and fabrication

In Figure 3.4 the fabrication process for a vertically coupled resonator is schematically represented. The device substrate consists of a Si wafer with a thick thermally grown SiO_2 layer ($> 4\mu m$) on it. (a) As a first step the waveguide layer is deposited with precise calibration of the waveguide thickness and (b) a dry etching process defines the waveguide width. (c) The successive grown of a cladding layer results in a lifted geometry due to the presence of the waveguide which prevents any planar structure to be correctly fabricated. (d) To avoid this problem, by using BoroPhosphoSilicate-Glass (BPSG) as the cladding material, repeated high temperature thermal treatment of the wafer allows the planarization of the device to reach 96%. (e) After that, a precise definition of the waveguide-resonator vertical gap and a perfect planarization can be obtained by Reactive Ion Etching (RIE) of the BPSG layer. (f) Finally the resonator layer can be grown up to the wanted thickness and its geometry can be defined with a photoresist mask and a dry RIE. (e') A similar fabrication process, with a sacrificial layer of amorphous Silicon (a-Si) above the BPSG cladding, (f') allows a free-standing device to be created. (f") A wedge resonator can also be obtained by substituting the final dry etching with a wet chemical etching in HF buffered solution.

The fabrication process allows to evidence some positive features directly related to the use of vertically coupled resonators. At first, the definition of the waveguide-resonator vertical distance by means of RIE provides an extremely precise control on the gap value (at the nanometer level), without the employment of any high resolution lithography [9]. Secondly, waveguide and resonator materials are independently chosen, thus allowing different configurations to be exploited. In addition, wedge resonators can be obtained without affecting the bus waveguide geometry [12]. These last two possibilities are not possible with common in-plane coupling, where the material of all the guiding elements is the same and only dry etching processes can be performed to preserve waveguide shape, unless very complicated processes are used.

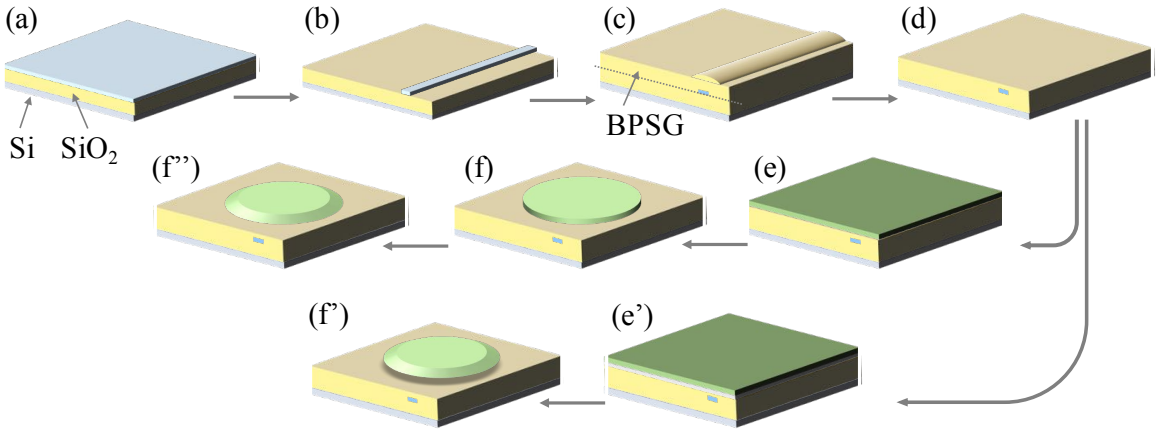

Figure 3.4: Fabrication process for the creation of a normal, free-standing (') and wedge (") vertically coupled resonator.

Finally, the realization of a freestanding device coupled to a fixed waveguide diminishes the vibration related noise that occurs when optomechanical experiments are performed.

3.3 Vertical coupling: theoretical model

In contrast with in-plane structures, in a vertically coupled geometry the interaction between the two elements does not take place in a single point. Indeed, the placement of the bus waveguide under the resonator enlarges the area of interaction as depicted in Figure 3.5(a). In particular, it comes out from geometrical considerations that the distance between the guided modes of the two elements is kept almost constant over a wide area, called flat zone Λ (Figure 3.5(b)), which can be considered as the effective interacting region of the system [14]. The existence of this flat zone makes the system very similar to a directional coupler and suggests to adopt this structure as an approximation of the vertically coupled device.

Starting from this assumption, the waveguide and resonator output fields (a_3 and a_4) can be related to the input fields (a_1 and a_2) as [41]:

$$\begin{aligned} a_3 &= a_1 e^{i\frac{\Delta\beta}{2}z}\left[\cos(\gamma z) - i\frac{\Delta\beta}{2\gamma}\sin(\gamma z)\right] + a_2 e^{i\frac{\Delta\beta}{2}z}\frac{C_{12}}{i\gamma}\sin(\gamma z)\,, \\ a_4 &= a_2 e^{-i\frac{\Delta\beta}{2}z}\left[\cos(\gamma z) + i\frac{\Delta\beta}{2\gamma}\sin(\gamma z)\right] + a_1 e^{-i\frac{\Delta\beta}{2}z}\frac{C_{21}}{i\gamma}\sin(\gamma z) \end{aligned} \tag{3.8}$$

where

$$\gamma = \left[(\Delta\beta)^2 + C_{12}\,C_{21}\right]^{1/2} \tag{3.9}$$

is a system parameter depending on the propagation constant mismatch between the resonator and the waveguide $\Delta\beta = \beta_1 - \beta_2$ and on the mode overlap coefficients C_{12}, C_{21}. Considering the resonant condition linking the resonator input and output fields:

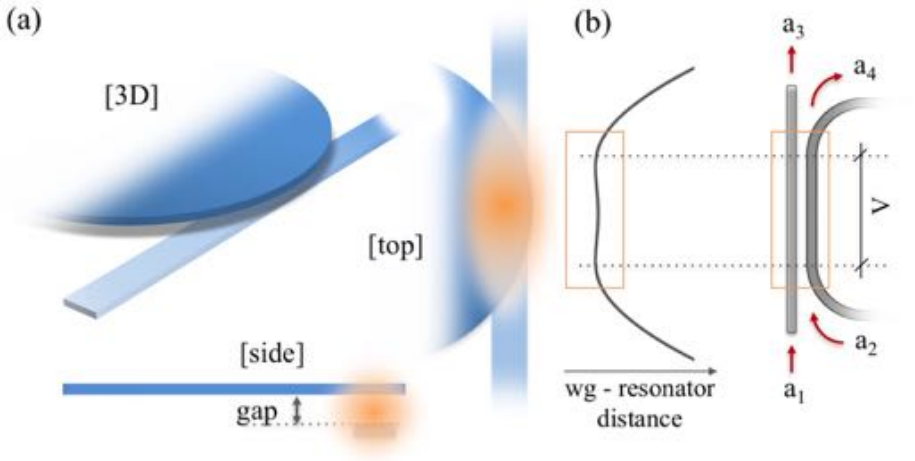

Figure 3.5: (a) schematic representation of a microdisk-bus waveguide system with the coupling region highlighted by orange circles; (b) effective distance between the two coupling elements in a vertically coupled system (left) compared to the distance between waveguides in a directional coupler (right).

$$a_2 = a_3 e^{-i\frac{2\pi n_{eff1}}{\lambda}(2\pi r - \Lambda)} e^{-\alpha L} \tag{3.10}$$

a solution to Equation 3.8 can be computed and the transmittance of the system in the vicinity of a resonance can be described by a Lorentzian function of the form:

$$T(\lambda) = \left|\frac{a_3}{a_1}\right|^2 = \left| A + i\,\frac{\frac{c}{n_{eff1}L} B e^{-\alpha L}}{(\frac{2\pi c}{\lambda} - \frac{2\pi c}{\lambda_0}) - i\,\Gamma/2} \right|^2 \tag{3.11}$$

with:

$$A = exp\left(i\,\frac{\Delta\beta}{2}\Lambda\right)\left[cos(\gamma\Lambda) - \frac{\Delta\beta}{2} sin(\gamma\Lambda)\right] \tag{3.12}$$

$$B = \left[\frac{C_{12}\,C_{21}}{\gamma^2}\right]\, sin^2(\gamma\Lambda) \tag{3.13}$$

$$\Gamma = \frac{2c}{n_{eff1}L}(1 - |A|e^{-\alpha L}) \tag{3.14}$$

The new quantities that appear in Equation 3.11, 3.12, 3.13, 3.14 are: c the light speed in vacuum, L the length of the resonator, λ_0, n_{eff1} and α the resonant wavelength, the effective index and the intrinsic loss coefficient of a given resonator mode.

In the on resonance condition (i.e. with $\lambda = \lambda_0$) the transmittance reaches its minimum value, corresponding to the ER parameter already introduced. Therefore, from Equation 3.11 the ER can be written as:

$$ER = \left| A - \frac{\frac{c}{n_{eff1}L} B e^{-\alpha L}}{\Gamma/2} \right|^2 \tag{3.15}$$

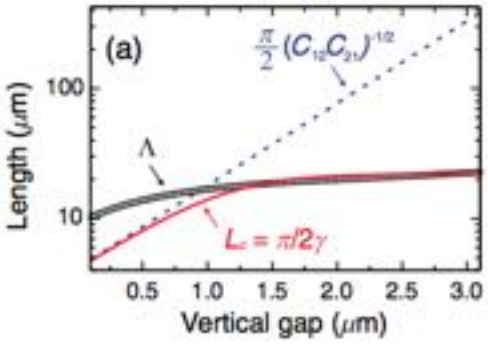

Figure 3.6: Flat zone Λ, directional coupler coupling length and coupling coefficients ($C_{12}C_{21}$) as a function of gap. (Figure from [14]).

At this point the dependences of ER on the different system parameters can be investigated. In particular, in order to give a comprehensive view of the system, a brief description of the dependence on the vertical gap is firstly given in (see Section 3.3.1). This analysis presents the results described in [14] and it constitutes the starting point for the further theoretical and experimental investigation on wavelength dependence presented in Section 3.3.2 and Section 3.4.

3.3.1 Gap dependence

For what concerns the gap dependence, the relevant variations that must be taken into account are the effective interaction length (i.e the flat zone Λ) and the overlap coefficients C_{12}, C_{21}. Indeed, other parameters, such as the resonator effective refractive index or the resonator intrinsic losses, are barely affected by the waveguide vertical movement.

The flat zone is defined from geometrical considerations as the distance between two inflection points of the quantity dL_v/dz (i.e. when $d^2L_v/dz^2 = 0$). An example of its dependence on the vertical distance is depicted in Figure 3.6, with the interaction length doubling its value as the gap is increased. The considered geometry consists of a $40\mu m$ radius disk resonator 400nm thick vertically coupled to ist bus waveguide ($2.5\mu m \times 250nm$). The overlap coefficients [23] describe the superposition between the waveguide and the resonator mode fields within the waveguide cross section (C_{12}) or the resonator area (C_{21}) [2], and they show an exponential dependence on gap variations [71]. An example of this dependence is shown in Figure 3.6, where the two coefficients for coupled slab waveguides are represented. In the same figure the flat zone elongation is compared to the coupling length of a common directional coupler predicted by coupled mode theory $L_c = \pi/2\gamma$. Thicknesses of 400nm and 250nm for the coupled waveguides have been used to compare with the flat zone calculations.

Adding these dependences to Equation 3.11, the system ER can be computed

[2]These two coefficients are considered to be constant along the coupling length (border effects are negligible).

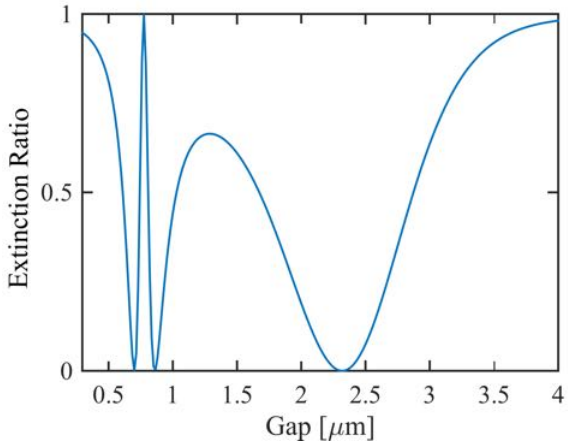

Figure 3.7: ER dependence on gap for a vertically coupled resonator as obtained from Equation 3.15 .

for different gap values (see Figure 3.7). From the figure, an oscillating response is evidenced, with the system reaching complete transparency ($ER = 1$) and complete absorption ($ER = 0$) at multiple gap values, in a very different fashion to what is commonly observed for in-plane resonators.

3.3.2 Wavelength dependence

The similarity between a vertically coupled structure and a directional coupler, which is demonstrated for gap variations, can be verified also for wavelength dependences.

Indeed, the Coupled Mode Theory (CMT) applied to directional couplers shows that coupling of light from one waveguide to the other depends on wavelength with a periodic behaviour [41] and light can be completely transferred from one waveguide to the other at different wavelengths. Therefore, in a vertically coupled system the same coupling factor should be achieved at several wavelengths, generating several critical coupling scenarios.

To verify this qualitative concept, we extend here the above described model to wavelength variations. In particular, in the equation for the ER (Equation 3.15), several wavelength dependent quantities can be found. In order to take into account the different variations, a simplified model based on two slab waveguides is exploited, thus resembling the behaviour of common directional couplers. As a consequence, the explicit dependence of the different quantities on wavelength is described by only few parameters: the geometrical parameters of the system (waveguide thickness, width and separation), the refractive indexes of the materials, the resonator effective mode radius r and its attenuation coefficient α. Indeed, the approximation allows to derive all the other quantities from analytical calculations.

From ellipsometric measurements, the refractive index of the three materials constituting the system (resonator n_1, bus waveguide n_2 and cladding n_c) can be found at varying wavelengths. Then, the first waveguide mode can be obtained by solving

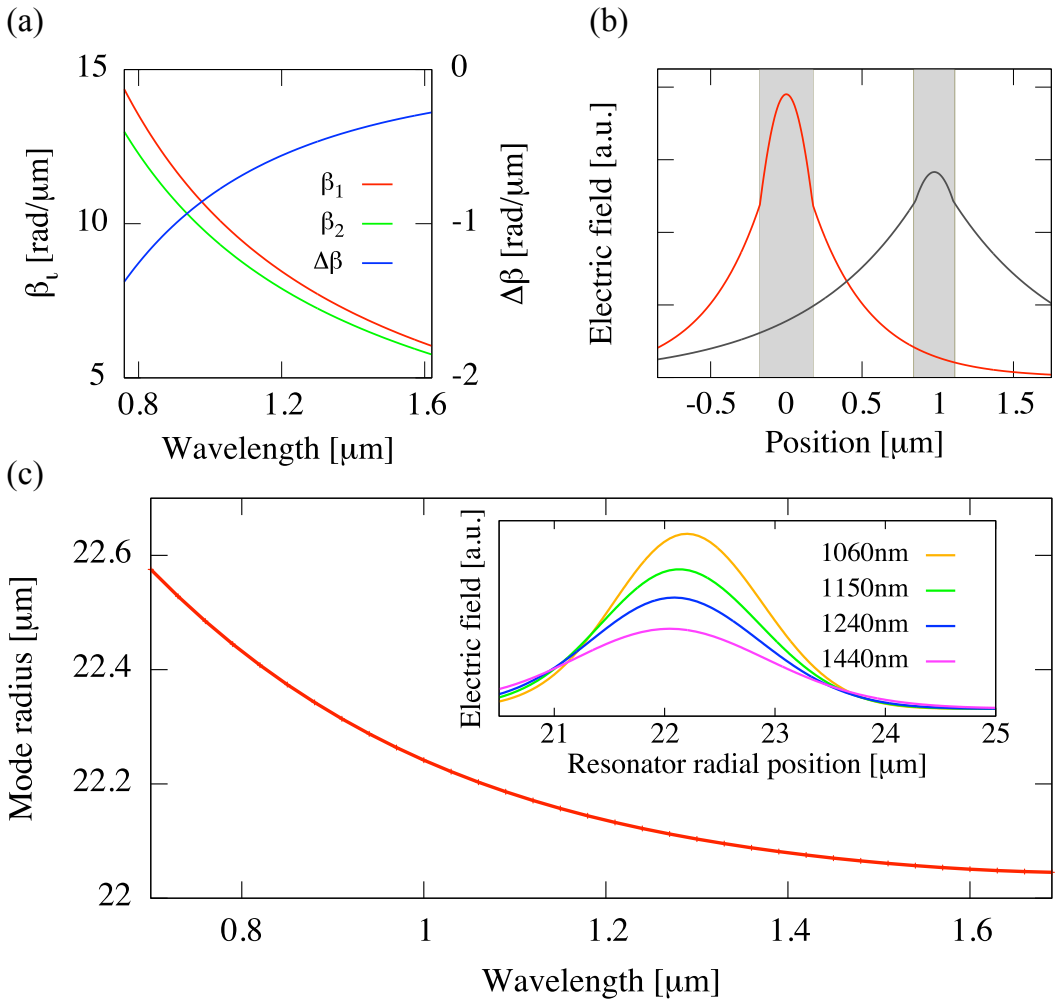

Figure 3.8: (a) Propagation constants and propagation constant mismatch in the IR domain from (3.17); (b) normalized mode profiles calculated for the two waveguides at fixed wavelength ($1.55\mu m$); the shaded areas defines the actual position of the two elements; (c) the radial position of the maximum of the electric field and (inset) radial shape of the mode inside the resonator at different wavelengths; a resonator radius of $25\mu m$ and thickness of 350nm has been considered.

the transcendental equation [23]:

$$tan\left(\frac{\pi\ d\ sin(\theta_i)}{\lambda}\right) = \sqrt{\left(\frac{sin(\frac{\pi}{2}-\theta_c)}{sin(\theta_i)}\right)^2 - 1} \tag{3.16}$$

where d is the thickness of the considered waveguide, θ_i is the propagation angle, $\theta_c = n_c/n_i$ and $n_i = n_1$ or n_2 depending on whether the resonator or the bus waveguide is considered. The propagation constant β_i and the extinction coefficient τ_i are obtained from the angle θ_i as:

$$\beta_i = n_i\left(\frac{2\pi}{\lambda}\right) cos(\theta_i); \quad \tau_i = n_c\frac{2\pi}{\lambda}\sqrt{\frac{cos(\theta_i)^2}{cos(\pi/2-\theta_c)^2} - 1} \tag{3.17}$$

In Figure 3.8(a) the propagation constants for two slab waveguides and the propagation constant mismatch $\Delta\beta = \beta_2 - \beta_1$ is shown (thicknesses: 350nm and 250nm). With τ and β known for both waveguides, the mode profiles along the coupling direction can be found (Figure 3.8(b)) and the overlap coefficients C_{12}, C_{21} can be extrapolated from the overlap of the two fields inside the waveguides [23].

The effective index n_{eff} comes out directly from the propagation constants as $n_{eff} = \beta(2\pi/\lambda)$.

The length of the resonator is $L = 2\pi r$ with r the resonator radius, while the size of the flat zone Λ depends on the vertical distance between the waveguide and the resonator L_v as described in Section 3.3.1. Since in the experiment described below (see Section 3.4 [12]) only wedge resonators are used, particular attention should be paid to the different radial modes. Indeed, a univocal definition of the resonator radius is not possible due to the fact that the different modes circulate on different circumferences. As a result, the parameter r represents an effective radius, which describes the system position where the field inside the resonator reaches its maximum intensity (Figure 3.8(c)), and it can be easily extrapolated from 2D finite element simulation (the actual resonator radius has been fixed to $25\mu m$ to mimic the real system). From this assumption the L value is directly obtained, and also Λ can be derived once the relative positions of the microresonator and the bus waveguide are given. The last unknown quantity needed for the computation of Equation 3.15 is the intrinsic loss of the resonator, which can be obtained from FEM simulations.

Inserting the values for the different parameters in Equation 3.15 the wavelength dependence of the on resonance transmittance (ER) for a vertically coupled structure is obtained. An example of this is shown in Figure 3.9, together with the transmittance of a symmetric directional coupler and the ER coming from a laterally coupled device obtained from Equation 3.4. In particular, in the vertical coupling geometry and in the directional coupler there are multiple critical coupling wavelengths ($T_{min} \sim 0$). The similarity between the two curves comes from the elongated coupling region that characterize both these structures. This behaviour contrasts to what is observed for a point coupling geometry, i.e. for a lateral coupling configuration, where

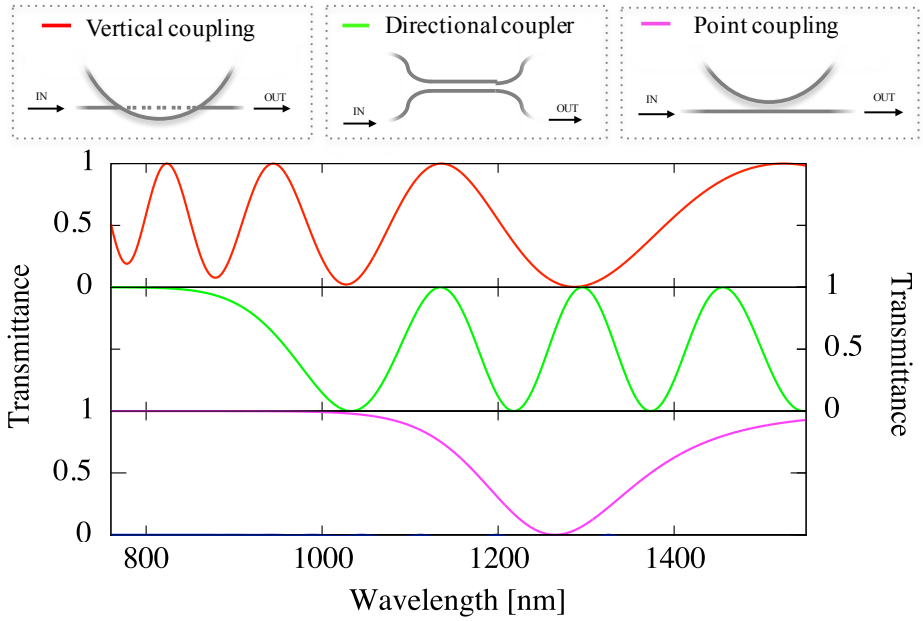

Figure 3.9: Bus waveguide coupling scheme (top) and ER dependence on wavelength (bottom) for a vertically coupled resonator, as resulting from Equation3.15, for a directional coupler, as obtained from the coupling coefficient described in Equation 3.6, and for a point coupled resonator, as resulting from Equation 3.4; a $75\mu m$ long symmetric SiN coupler have been used for the directional coupler, with waveguide dimensions of $2.5\mu m \times 250nm$; $25\mu m$ radius $350nm$ thick SiN resonator and $250nm$ SiON bus waveguide have been considered for the simulation of microresonators, with $20\mu m$ flat zone length in the vertical coupling case.

the critical condition occurs for a single wavelength only.

3.4 Wavelength dependence: experimental results

3.4.1 Device description

In order to verify the wavelength dependence of the model described above, some experimental measurements were performed on a real system. The system is composed by a 350 nm-thick and $24\mu m$ radius SiN wedge disk resonator vertically coupled to a 250nm-thick and $2.5\mu m$-wide SiON bus waveguide (Figure 3.10(a)). The employed fabrication process is the one described in Section 3.4, with a final isotropic wet etching resulting in a wedge angle of 7°. Complete characterization of the resonator dimensions and shape has been carried out through Atomic Force Microscope (AFM) measurements [72]. As a consequence of the wedge geometry, the optical mode radius is retracted from the external rim with respect to the one of an anisotropic dry-etched disk-resonator (Figure 3.10(b)). The extent of retraction depends on the considered wavelength (see Figure 3.8(c)) and on the observed optical mode [12]. The resonator vertical position is fixed 677 nm above the waveguide with BoroPhosphoSilicateGlass

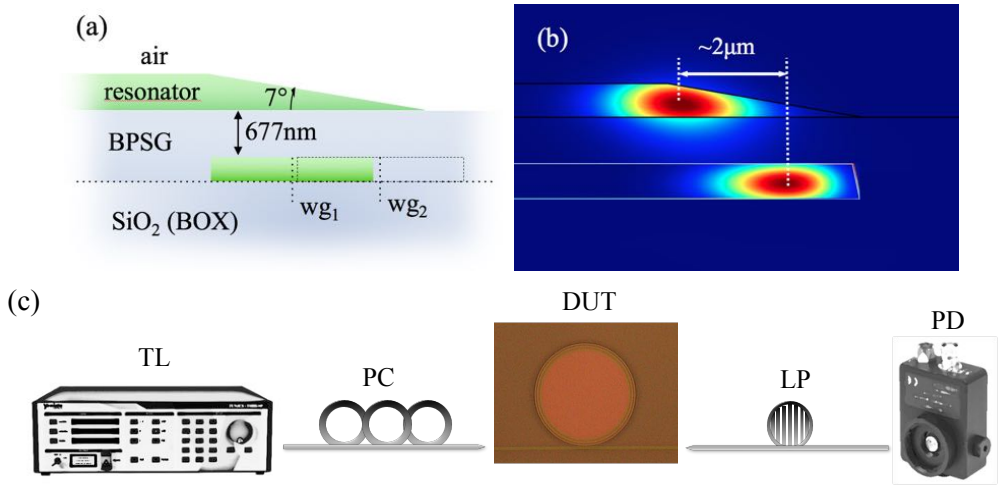

Figure 3.10: (a) sketch of the device (cross-section); vertical dashed lines show the central position of the waveguide in the two configurations; (b) simulated 1^{st} order radial mode cross section for wet (top) and dry (bottom) etched disk resonators showing $2\mu m$ difference in the mode radial position; $24\mu m$ external radius and $\lambda = 1.55\mu m$ have been considered in the simulation; (c) experimental setup for the optical characterization of the device: IR or visible light from two different tunable laser (TL) is sent in the polarization controller stage (PC) and coupled into the sample through tapered fibers; tapered fiber and polarization controller are also used to extract transmitted signal from the sample and to send it to the photodetector (PD).

(BPSG) cladding placed in between. Figure 3.10(a) shows the two possible configurations corresponding to horizontal distances of 2 or 1 μm between the centre of the waveguide and the outer rim of the disk. Henceforth we label these alignments wg_1 and wg_2 respectively. A $2\mu m$ thick SiO_2 cladding layer below the waveguide allows to isolate the optical modes from the Si substrate at the bottom of the wafer.

Optical measurements have been carried out in the visible and in the IR range: specifically from 760nm to 795nm and from 1440nm to 1630nm, with resolution of 3pm and 1pm, respectively[3]. While the IR measurements have been performed on the interferometric setup described in Chapter 2, the characterization in the visible range required a specific setup, which is schematically presented in Figure 3.10(c). Light from a tunable laser source has been coupled in and out from the sample using tapered lensed fibers and the transmitted signal has been acquired with a Ge photodetector. In both IR and visible measurements, a polarization controller in the input stage and a linear polarizer at the output one have been inserted in order to ensure the excitation and detection of a TE mode propagating in the bus waveguide. All experiments have been carried out at room temperature under stable and controlled conditions.

[3]Laser linewidth is below 1fm for both the laser.

3.4.2 Results

We first focus on the results coming from the wg_2 configuration, whose visible and IR spectra are shown in Figure 3.11. Both spectra show the typical periodic peaks related to resonant guided modes, with several order family modes coupled in the visible spectrum and only two modes in the IR one. Despite Free Spectral Range (FSR) analysis allows to identify the 1^{st} and the 2^{nd} TE radial modes as the coupled families in the IR range, the same analysis cannot be done in the visible range. Indeed, even though periodic peaks associated to different radial families can be recognized, they show very similar FSR and they cannot be identified within the experimental uncertainty. For this reason, we focused our attention on the brightest order family in the visible range, labeled by squares in Figure 3.11(top), showing transmittance and Q up to 20% and 20000, respectively. The IR spectrum, on the other hand, is mainly characterized by complex resonance line shapes where the 2^{nd} order family modes ($Q \sim 1000$) are reactively coupled to the 1^{st} order family modes ($Q \sim 20000$) [13].

The two spectra constitute a first confirmation of the theoretical model described in Section 3.3, which will be recalled here as *oscillatory model*, due to the multiple oscillations of the transmittance minima. The existence of peaks in the visible and IR spectra for the same device demonstrates that light over a 900nm range can be coupled simultaneously to a resonator just by using the vertically coupled configuration. This feature cannot be explained by the point coupling models [73, 68], which allow only a single wavelength for the critical coupling condition (Figure 3.9).

Also the fine feature of the visible spectrum supports the model: oscillations of the resonance depth are present, resembling those of a directional coupler [41]. The oscillations are explained by the oscillatory coupling model as shown by the dashed line in Figure 3.11. Simulation has been done by using the parameters reported in Table 3.1. Even though the simulated curve does not fit perfectly the experimental one, a qualitative agreement can be observed, showing that the results derived from the model are consistent with the experiment.

A similar analysis on the transmittance cannot be performed for the IR spectrum, because the 1^{st} and the 2^{nd} order families strongly affect each other by a reactive coupling mechanism (see Chapter 4 and [13]).

However, by using the wg_1 configuration we are able to preferentially excite the first order radial family in the IR range (Figure 3.12). In fact, when the waveguide is shifted $1\mu m$ inside the resonator edge, optimal overlap between the waveguide mode and the WGMr modes occurs for the first order radial mode [9]. With this wg_1 geometry, no signature of coupling in the visible range is observed, because the more confined visible modes do not overlap effectively with the bus waveguide mode.

Nonetheless, observations on the IR spectrum can still bring to a richer understanding of the physics of the system. The 1^{st} family in Figure 3.12, well isolated from the 2^{nd} family, shows a peculiar shape describing a clear oscillation with a contrast of about 30%. An alternative possible explanation to this feature could rely

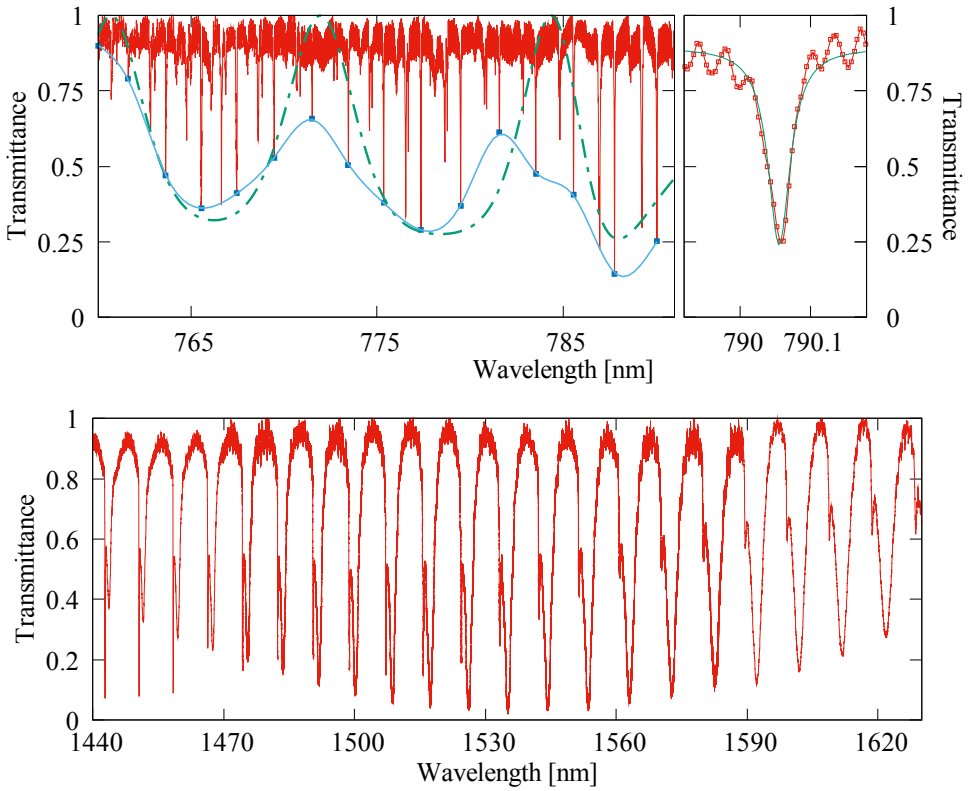

Figure 3.11: (top-left) visible spectrum for wg_2 configuration; the transmittance minima of the investigated family of resonances from the experiment (square symbols and interpolation line) is compared to the transmittance minima obtained from the model (dashed line); (top-right) detail of an isolated resonance with a Lorentzian fit (with laser resolution of about 3pm); (bottom) IR spectrum for wg_2 configuration with 1^{st} and 2^{nd} order family mode resonances.

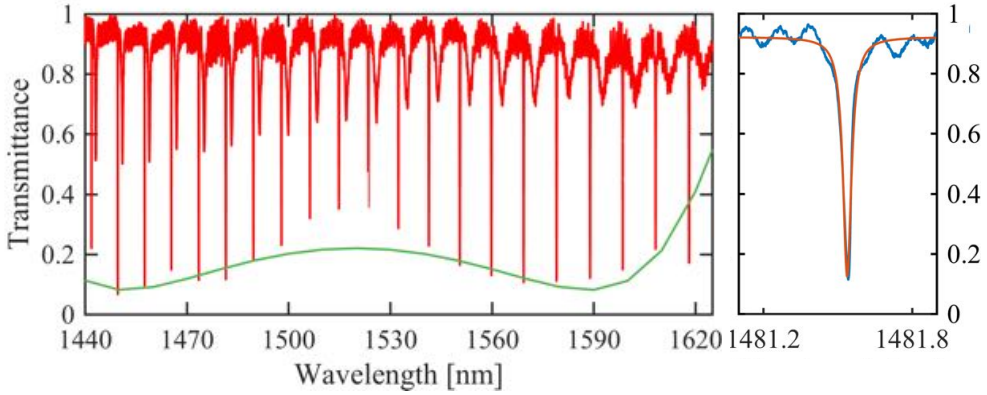

Figure 3.12: (left) IR transmission spectrum of the wg_1 configuration and a fit of the model (line); (right) detail of an isolated resonance with Lorentzian fit (with laser resolution of about 1pm).

	Λ [μm]	thickness [nm]	α [$1/cm$]	gap [nm]
vis	20±10	100±20	0.4±0.1	670±20
IR	12±5	350±50	0.6±0.1	700±50

Table 3.1: Fitting parameters as found for Figure 3.11(top) and Figure 3.12.

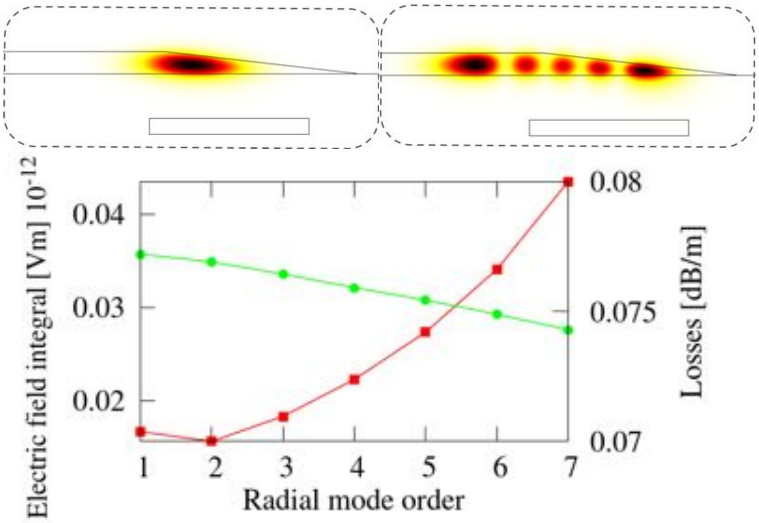

Figure 3.13: (top panel) Mode profiles at $\lambda = 780nm$ for the 1^{st} order radial mode and for the 5^{th} order radial mode. (bottom panel) Integral of the electric field of the different resonator optical modes computed in the bus waveguide region (red line and squares) and propagation losses (green line and disk) for $\lambda = 780nm$.

on different material absorption channels (as for instance: Si-H bondings produced as residuals of the fabrication precess). However, the ellipsometry characterization revealed negligible material losses in this spectral region. As already pointed out, also the effect of a point coupling interaction cannot bring to such a behaviour, since the only oscillation that is expected from the model consists of a single dip in the transmittance. Actually, a reasonable explanation to this issue can be given by the oscillatory coupling model described above. Indeed, as found for the visible spectrum of wg_2, the ER obtained from the model (line in Figure 3.12) qualitatively follows the oscillating behaviour of the experimental curve and, thus, confirms the oscillatory coupling model as a good description of vertically coupled systems.

The parameters resulting from the fit in the two regimes are shown in Table 3.1.

Despite the uncertainty on the Λ values due to the approximations in the model, we notice that Λ and thickness are significantly different in the VIS and IR. In particular the thickness in the VIS range is not compatible with the experimental one ($\sim 350nm$). However, this apparent discrepancy can be solved by considering two peculiarities of the system: the geometry of the resonator and the coupling of higher order modes in the visible range. Indeed, the wedge shape of the resonator causes the thickness of the resonator in its external part to be strongly dependent on the radial position, starting from $350nm$ at $21.5\mu m$ radius and decreasing to $0nm$ at $24\mu m$.

In order to take this evidence into account in the model, we consider the parameter thickness as an effective parameter, which corresponds to the resonator thickness felt by the optical modes along the coupling region. In addition to this, higher order modes in the visible range are pushed at larger radii by the wedge geometry (Figure 3.13(top)) and they show a stronger electric field in the waveguide region (Figure 3.13(bottom)) where the resonator effective height can be substantially lower than 350nm. As a consequence to these considerations, an effective thickness as low as $0.1\mu m$ can be assumed in the visible range. The same geometrical argument (resonator optical modes propagating at larger radii) justifies the larger flat zone found for the visible modes with respect to the IR ones. Indeed, in the IR range only the 1^{st} and 2^{nd} order family of TE modes should be taken into account, since higher order modes are absorbed by the Si substrate (see Appendix B for details on substrate absorption). TM modes in the IR range are also absorbed by the substrate, due to their lower confinement. Losses and gap values are in agreement with values found in [14] and with Scanning Electron Microscope measurements respectively. This analysis does not consider a possible contribution from TM modes propagating in the resonator. This is because the bus waveguide does not support TM modes and it works as a filter for the excitation and extraction of TM modes propagating in the resonator. However, given the peculiar geometry of the coupling and of the resonator there could be a polarization rotation mechanism at the coupler region. Despite this seems a weak effect with respect to direct excitation of TE modes, it should be verified with some measurements or 3D simulations. At this point it is also worth noticing that the developed model takes into account only first order modes for both the waveguide and the resonator, while higher order modes are present in the real structures at visible and IR wavelengths. The model contains another important approximation on the relative position between the waveguide and the resonator modes along the coupling region: due to the different shape of the two elements (straight and circular, respectively) the interaction occurs at always different angles, with the mode in the resonator changing its phase velocity with respect to the waveguide mode. In this sense the model is an approximate one and the parameter describing the actual device (such as the flat zone, the propagation constants, the resonator radius, etc.) should be considered as effective/mean parameters. These considerations can explain the difference between experimental data and simulated ones. The fitting curve presented in Figure 3.12 shows that the model is not able to perfectly match the real system, yet. In particular, for long wavelengths the model predicts an increase in the transmittance which is not experimentally observed. For this reason, the use of full 3D simulations of the real system, similar to those shown in [13], the possibility to acquire data in different spectral regions (e.g. NIR) and the developement of a position dependent model (i.e. a model which takes into account the relative position between the two elements along the coupling region) could constitute important thrusts for a more accurate modeling of the investigated device.

Other interesting information about the studied system can be extracted from a

comparison of the Q of the 2^{nd} order family in the IR spectra for the wg_1 and wg_2 configurations. These are discussed in Appendix B.

3.5 Conclusion and perspectives

In this Chapter the theoretical model describing coupling of light inside a singlemode vertically coupled resonator has been proposed and its experimental validation has been presented. In particular, the oscillatory behaviour of the resonance transmittance predicted by the model has been observed both for gap and for wavelength variations. From an experimental point of view, a deeper analysis on gap dependence has been performed, and simultaneous coupling of visible and IR light in a WGM wedge resonator has been demonstrated. These results evidence the inadequate description provided by the point coupling model and justify the formulation of a different model for the coupling process of the vertically coupled geometry. The proposed model and its dependences on gap and wavelength constitute a remarkable tool for the application of this structure to a wide range of fields, from biosensing to telecommunication. Indeed, in the biosensing area the possibility to exploit a wedge shaped resonator and to selectively expose the resonator to the outer environment, burying the waveguide under a cladding layer, constitutes a remarkable feature which increases the detection sensitivity of the device [72]. In addition, the oscillating coupling strength allows a device to be tested at multiple frequencies. This represents an important condition to efficiently probe diverse biological components, each one with a specific spectral response, with only one resonator. In the telecommunication area, the observed wavelength dependence allows the design of large bandwidth resonators, a feature which constitutes a desirable basis for the development of a multichannel technology [74], opening the possibility to further increase the number of operation per device. Also the selective excitation of a specific radial mode order that has been shown in this Chapter (compare Figure 3.11 with Figure 3.12) can be exploited to reach multiple channel operation within the same device, for example by coupling a single resonator to distinct waveguides placed at different horizontal positions with respect to the resonator edge. The oscillating coupling observed for wavelength variations allows also to create a device where critical coupling of the various signals of a frequency conversion process can be obtained, resulting in an overall increase of the efficiency. Finally, all these applications must be joined and added to other interesting features related to the vertical coupling, such as low cost CMOS compatible fabrication process and stable coupling with free-standing structures [9, 75], which make the employment of vertically coupled structures a close and desirable goal for the design of compact and cost-effective photonic chips.

Chapter 4

Reactive coupling in microresonators

Beyond the great number of applications that can be enabled with a vertically coupled resonator, there are also several interesting physical phenomena that can be observed thanks to the peculiar features of this structure. In particular, the possibility to balance the excitation of different radial mode orders and the peculiar coupling process described in Chapter 3 help to highlight the presence of a reactive component in the mutual coupling between different resonator modes.

The present Chapter investigates this phenomenon both with theoretical model and experimental results and it is divided as follows: a brief introduction to the phenomenon of reactive coupling in the context of open systems is firstly given in Section 4.1; the theoretical model proposed in [13] for a vertically coupled resonator is discussed in Section 4.2 and a further development of the model is also presented, which provides a different view for the system response; finally, Section 4.3 contains the experimental validation of the model through transmittance and phase measurements.

4.1 Introduction

The effect of coupling a physical system to its environment constitutes the key point of open systems. The interaction of a system with an external element creates both dissipative and reactive channels, which lead to energy decay and shift, respectively [76]. This effect has been firstly observed in atoms, where the coupling of the discrete atomic levels to a continuum of states by radiative decay channels modifies the spontaneous decay rates of the system [77, 78] and a shift in its transition frequencies, namely, a Lamb shift [79]. Similar results have been reported in nanoparticles, with asymmetric scattering observed when plasmon excitations interact with radiative decay paths [80]. In the field of photonics, the coupling of light to and from a resonator by its bus waveguide is associated to a shift and a spectral broadening of the resonance [81, 82]. Indeed, even though it is needed to probe the resonator properties, the waveguide constitutes a perturbation to the environment perceived by the resonator and it modifies consequently the resonator modal spectrum Actu-

ally, also the coupling between different resonator modes has been demonstrated to modify the system response: the interference between different optical modes of two side coupled resonators system creates a transparency window in their spectrum [83]; this effect, called Coupled Resonator-Induced Transparency (CRIT), is the all optic analog to the Electromagnetic Induced Transparency (EIT) effect observed in the atomic context [84] and it is a widely studied effect for its many fundamental and practical implications, such as tunable delay lines and filters [85]. Recently, investigation on optomechanical resonating systems showed an Optomechanically Induced Transparency (OIT) effect [86], where the coupling of optical modes (photons) with mechanical ones (phonons) produces a transparency effect similar to the one observed in EIT. Interestingly, most of the studies and investigation on coupling induced effects have been mainly devoted to the action of the dissipative component, the reactive one not being similarly discussed. In the present Chapter both the dissipative and the reactive components associated to light coupling in a multimode vertically coupled resonator are investigated from a theoretical and an experimental point of view. In particular, a waveguide mediated intermode coupling is observed, with great influence on the system response: depending on the relative detuning between the coupled modes, the reactive component of the coupling is demonstrated to enhance or suppress the appearance of resonances in the spectrum. The interference between resonator modes brings to EIT-like effect and to asymmetric Fano lineshapes, thus confirming the analogy between photonic and atomic systems.

4.2 Model description

In this Section the theoretical model describing the intermodal coupling in a vertically coupled resonator is proposed. Following the experimental results, only two modes belonging to different radial families of the resonator are here considered. Nonetheless an extension to an arbitrary number of modes is possible. Starting from a discussion on the original model demonstrated in [13], a new formulation of the equations is proposed. This allows to identify two different contributions in the system response: the first representing the average between the two excited modes and the second containing information on the differences between the two coupled modes. The new formulation is demonstrated to be particularly useful in the case of quasi degenerate modes, i.e. when small differences in resonance wavelength, intrinsic losses and coupling coefficients between the modes are present.

As a first step, it is useful to start from the most simple case of a single mode resonator coupled to a bus waveguide, (schematically represented in Figure 4.1(left)), whose equation of motion can be obtained from Temporal Coupled Mode Theory [87]:

$$i\frac{d\alpha(t)}{dt} = \left[\omega_0 + \Delta - i\frac{\gamma^{nr} + \Gamma^{rad}}{2}\right]\alpha(t) + gE_{in}(t) \tag{4.1}$$

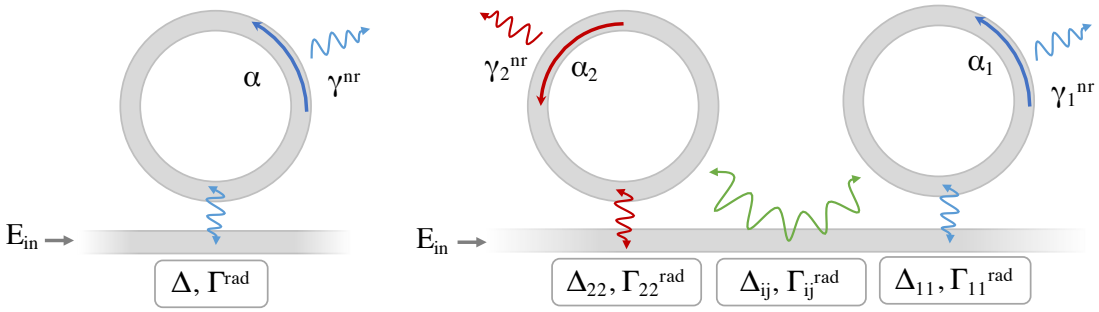

Figure 4.1: Schematic representation of a single mode resonator (left) and of a multimode resonator (right) with waveguide mediated intermode coupling.

where α is the amplitude of the electromagnetic field propagating along the waveguide and ω_0 is the unperturbed resonant frequency. Δ is the reactive term due to the presence of the waveguide, which causes a spectral shift of the resonance. The dissipative counterpart to Δ is described by Γ^{rad}, which represents the radiative losses related to the coupling with the waveguide. This last term, together with the intrinsic (non-radiative) loss term γ^{nr}, determines the overall losses of the waveguide-resonator system. The excitation source, needed to load the resonator, is described by the last term in Equation 4.1. It is an incident field, $E_{in}(t)$, weighted by the coupling coefficient g. As it is expected, Equation 4.1 resembles Equation 3.1 already presented for an in-plane coupled resonator and produces the already investigated Lorentzian shaped resonance. The three regimes of under, over and critical coupling described in Section 1.2 are here driven by the ratio between γ^{nr} and Γ^{rad} .

Let us now consider a resonator with more radial modes, e.g. two. Then, two copropagating modes, with different radial mode orders, can be considered to travel simultaneously along the resonator. Since the bus waveguide breaks the system symmetry, the two modes interact. Addition of a complex term to the single mode equation takes into account the coupling between the two traveling fields. The two coupled mode equations can then be written as:

$$\begin{cases} i\frac{d\alpha_1(t)}{dt} = \left[\omega_1 + \Delta_{11}^{rad} - i\frac{\gamma_1^{nr}+\Gamma_{11}^{rad}}{2}\right]\alpha_1(t) + \left[\Delta_{12}^{rad} - \frac{i\Gamma_{12}^{rad}}{2}\right]\alpha_2(t) + g_1 E_{in}(t) \\ i\frac{d\alpha_2(t)}{dt} = \left[\omega_2 + \Delta_{22}^{rad} - i\frac{\gamma_2^{nr}+\Gamma_{22}^{rad}}{2}\right]\alpha_2(t) + \left[\Delta_{21}^{rad} - \frac{i\Gamma_{21}^{rad}}{2}\right]\alpha_1(t) + g_2 E_{in}(t) \end{cases} \tag{4.2}$$

In Figure 4.1(right) a schematic representation of the system described by the equation is sketched. The two Hermitian (2x2) matrices Δ^{rad} and Γ^{rad} take into account the presence of the loading waveguide in its reactive and dissipative effect on the resonator response, respectively. Diagonal elements Δ_{jj}^{rad} and Γ_{jj}^{rad} come from the direct action of the waveguide and they are present also in Equation 4.1 for a single propagating mode. Off-diagonal terms Δ_{ij}^{rad} and Γ_{ij}^{rad} count for the intermode

interaction that is mediated by the waveguide, which allows to transfer optical power between the two modes at the coupling stage [1]. Therefore, absence of Δ^{rad} and Γ^{rad} matrices corresponds to the case of unperturbed singlemode resonators, where no waveguide is present, whereas absence of diagonal terms only, describes the case of two propagating modes not interacting between each other.

In this analysis, only the fundamental mode of the bus waveguide is considered to play a significant role in the system dynamics. This assumption is based on the large overlap between the fundamental mode of the waveguide and the gaussian mode that is used to excite it (coming from an objective or from a tapered fiber), which should produce a minor excitation of higher order modes. Consequently, the contribution of higher order waveguide modes to the non-diagonal reactive term is neglected ($\Delta_{ij}^{other} = 0$) and the related diagonal element Δ_{jj}^{other} is reabsorbed in the observed resonant frequency $\omega_j = \omega_j^0 + \Delta_{jj}^{other}$.

Following what has been proposed in [13], Δ^{rad} and Γ^{rad} matrices can be rewritten as:

$$\Delta^{rad} = \begin{pmatrix} \eta_1^2 & \eta_1\eta_2 \\ \eta_2\eta_1 & \eta_2^2 \end{pmatrix} \bar{\Delta}^{rad} \qquad \Gamma^{rad} = \begin{pmatrix} \eta_1^2 & \eta_1\eta_2 \\ \eta_2\eta_1 & \eta_2^2 \end{pmatrix} \bar{\Gamma}^{rad} \tag{4.3}$$

where $\bar{\Delta}^{rad}$ and $\bar{\Gamma}^{rad}$ are overall frequency shift and dissipation rate, respectively. The new coupling coefficients, η_1 and η_2, are relative weights for the coupling of the incident field $E_{in}(t)$ to the two resonator modes (they correspond to the coefficients g_1 and g_2) and they characterize the diagonal elements Δ_{ii}^{rad} and Γ_{ii}^{rad} , thus governing the waveguide-resonator coupling strength for the two modes. Moreover, as a consequence to the waveguide-mediated intermode coupling, η_1 and η_2 also mediate the off-diagonal elements Δ_{ij}^{rad} and Γ_{ij}^{rad} of the reactive and dissipative matrices. Energy conservation requires that $\eta_1^2 + \eta_2^2 = 1$, which basically means that light can only be coupled to one of the two modes and no coupling related losses are present.

Equation 4.2 can be reformulated in matrix form as:

$$i\frac{d}{dt}\begin{pmatrix} \alpha_1(t) \\ \alpha_2(t) \end{pmatrix} = \begin{pmatrix} \sigma_1 & -a \\ -a & \sigma_2 \end{pmatrix}\begin{pmatrix} \alpha_1(t) \\ \alpha_2(t) \end{pmatrix} + \begin{pmatrix} \eta_1 \\ \eta_2 \end{pmatrix} E_{in}(t) \tag{4.4}$$

where:

$$\begin{aligned} \sigma_i &= \omega_i + \eta_i^2\bar{\Delta}^{rad} - \tfrac{i}{2}\left(\gamma_i^{nr} + \eta_i^2\bar{\Gamma}^{rad}\right) \\ a &= \eta_1\eta_2\left(\tfrac{i\bar{\Gamma}^{rad}}{2} - \bar{\Delta}^{rad}\right) \end{aligned} \tag{4.5}$$

As it can be seen from this new formulation, the diagonal elements σ_1 and σ_2 contain the perturbation produced by the waveguide on the resonator mode, both in resonance shift and losses. Similarly, the non diagonal element a describes the effect

[1] This interaction has been already observed in microspheres [88], where only a dissipative component is considered.

of an intermode coupling and it needs both the resonator modes to be excited ($\eta_1 \neq 0$ and $\eta_2 \neq 0$).

When a monochromatic wave is considered as the input source ($E_{in} = E_0 e^{-i\omega_{in}t}$), a stationary solution to Equation 4.4 can be found and the mode amplitudes results:

$$\bar{\alpha}_i(\omega_{in}) = \frac{\delta_j \eta_i - a\eta_j}{\delta_i \delta_j - a^2} E_0 \tag{4.6}$$

where $\delta_{i,j} = \omega_{in} - \sigma_{i,j}$.

In the case of non interacting modes ($a = 0$), the *i-th* mode field depends only on the direct excitation provided by the waveguide ($\bar{\alpha}_i(\omega_{in}) = \frac{\eta_i}{\delta_i} E_0$). Conversely, an additional source of excitation appears when the a term is different from 0: it represents coupling of light from the j-th mode to the i-th mode through the waveguide and it is responsible for many interesting effects that appear in the transmittance.

This last can be computed as the superposition between the input signal and the two mode fields $\bar{\alpha}_1$ and $\bar{\alpha}_2$:

$$t(\omega_{in}) = 1 - i\bar{\Gamma}^{rad} \left(\eta_1 \bar{\alpha}_1 + \eta_2 \bar{\alpha}_2\right) \tag{4.7}$$

where $\bar{\alpha}_1$ and $\bar{\alpha}_2$ are weighted by their coupling coefficients in order to obtain the field amplitude at the waveguide output. Considering Equation 4.6, the transmittance can be rewritten in a more explicit form:

$$t(\omega_{in}) = 1 - i\frac{\bar{\Gamma}^{rad}\eta_2^2}{\delta_2} - i\frac{\bar{\Gamma}^{rad}\eta_1^2}{\delta_1 - \frac{a^2}{\delta_2}} \left(1 - \frac{a}{\delta_2}\frac{\eta_2}{\eta_1}\right)^2 \tag{4.8}$$

As expected, cancelling the excitation source for one mode (i.e. $\eta_2 = 0$) results in a single mode transmission, which resembles the usual Lorentzian shape:

$$t(\omega_{in}) = 1 - i\frac{\bar{\Gamma}_1^{rad}}{\Delta\omega - \bar{\Delta}_1^{rad} + \frac{i}{2}\left(\gamma_1^{nr} + \bar{\Gamma}_1{}^{rad}\right)} \tag{4.9}$$

where $\Delta\omega = \omega_{in} - \omega_1$ is the laser to resonance detuning and $\bar{\Delta}_1^{rad}$, $\bar{\Gamma}_1{}^{rad}$ are the reactive and dissipative coupling related components.

Examples of the transmittance T as obtained from Equation 4.8 ($T = |t|^2$) are shown in Figure 4.2 for different coupling regimes (different rows) of the two coupled modes and for different values of the reactive term ($\bar{\Delta}^{rad} = -25$, 0, 25 GHz for left, center and right panels, respectively).

In order to obtain an easy comparison with the experimental results presented in Section 4.3, one narrow and one broad resonant modes are considered. Each panel shows the response for different relative detuning $\delta = (\omega_2 - \omega_1)/\gamma_2$ between the two resonances (δ values are shown in the right side of each spectrum): in particular, the narrow mode resonance is fixed to a given frequency and it is crossed by the broad one, which passes (from bottom to top of the panel) from negative detunings ($\delta = -3$) to positive ones ($\delta = 3$). It is worth to note that, while the reactive term $\bar{\Delta}^{rad}$ can be

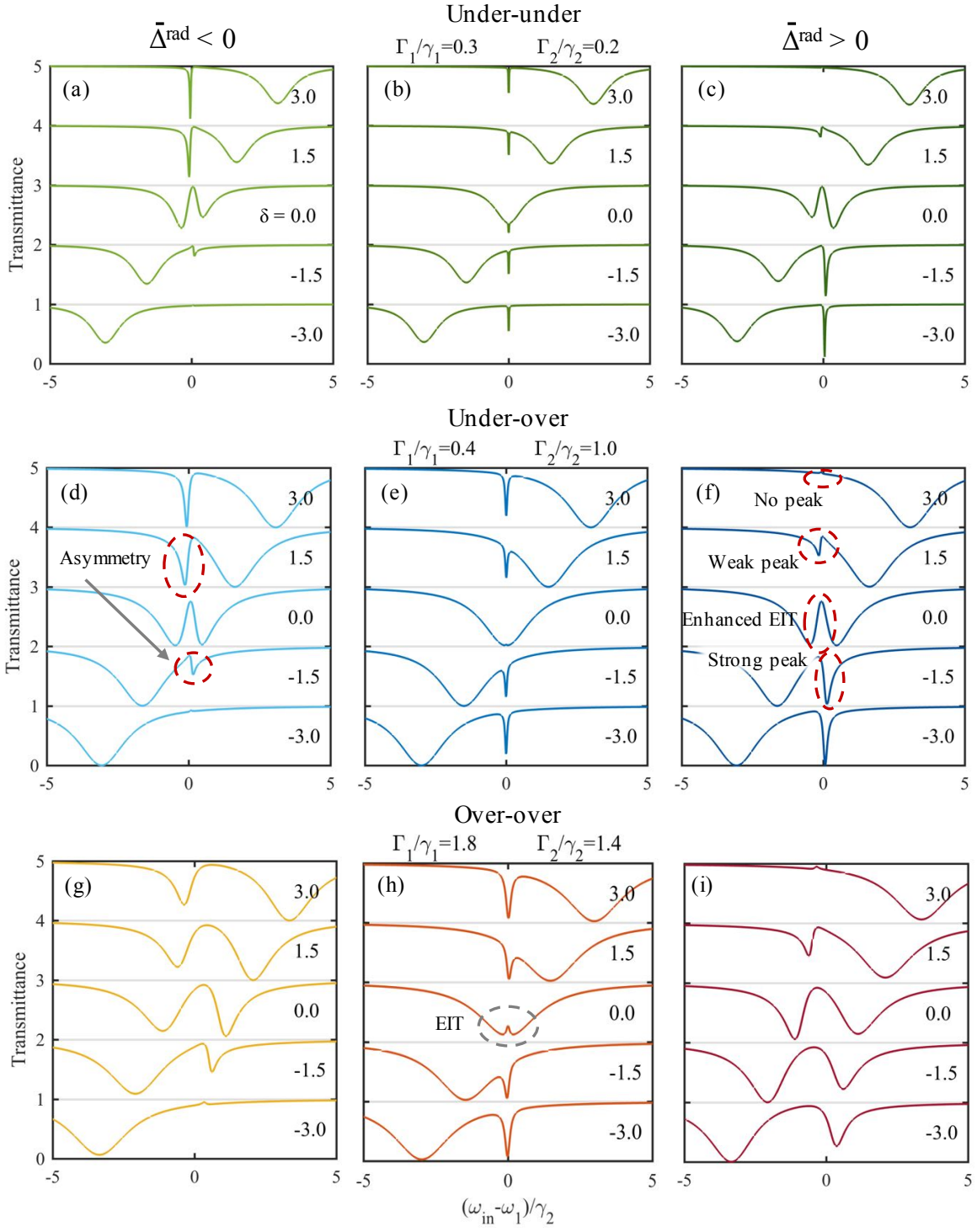

Figure 4.2: Simulated transmittance spectra for two coupled resonator modes as obtained from Equation 4.8 for different values of the reactive term: $\bar{\Delta}^{rad} = -25, 0, 25$GHz in the left, center and right panels, respectively; and for different coupling regimes (top, middle, bottom panels): the extrinsic over intrinsic coupling ratio for the two modes is shown above the central panels (left/right value for the narrow/broad mode); each panel contains spectra for five different detunings between the two families (successive spectra are offset by 1 for clarity and δ values are specified on the right side of each spectra); specific phenomena discussed in the text are highlighted in panels (d) and (f).

set to 0 value, the term $\bar{\Gamma}^{rad}$ needs always to be present to avoid unphysical results such as $T > 1$.

A first evidence that is verified in all the panels is the occurrence of asymmetric lineshapes associated to the narrow family (see panel (d) as the most evident case). This effect comes from the interference between the narrow and the broad coupled modes, and it can be thought as an all optical manifestation of Fano resonances commonly observed in atomic physics [89, 90]. According to this view, the narrow mode plays the role of the discrete level of an atomic system, while the broad mode behaves as the continuum of states, showing an almost constant amplitude within the narrow mode resonance width [91]. In the case of small detunings this effect turns out in a EIT one, as it is observed in panel (h) for a null detuning between the two families.

Despite the presence of Fano resonances is independent from the values of the reactive component, other interesting effects are enabled by this term. In the following, the case of Under-over coupled narrow-broad families is used as a reference example since it more fathfully follows the experimental observations, but the same results can be also found in the other coupling configurations. In the case of no reactive coupling (panel (e) and all other central panels, $\bar{\Delta}^{rad} = 0$), the transmittance shows symmetric behaviour with respect to detuning between the two families: when the detuning is fixed to the same absolute value, the narrow dip at frequency ω_1 (center of the spectra) shows the same extinction ratio (i.e. on resonance transmittance) and shape, no matter on the sign of the detuning. Once the reactive component is added to mode coupling ($\bar{\Delta}^{rad} \neq 0$) the behaviour with respect to the detuning δ is no more symmetric and the transmittance shape that is found for positive detunings is no more regained for negative detunings. An interesting evidence of this fact is the different extinction ratios found for the narrow family when three different detunings are considered. As an example, a positive ractive term can be considered (i.e. $\bar{\Delta}^{rad} > 0$). Comparison of the spectra presented in panel (f) for the different detunings shows the narrow resonance dip to become more pronounced for negative detunings, with respect to the $\bar{\Delta}^{rad} = 0$ case, and, conversely, to decrease its intensity for positive detunings. Remarkably, when the detuning is decreased to $\delta = -3$, an almost critically coupled narrow mode is observed, while it completely disappears from the transmittance spectrum when $\delta = 3$. Similar behaviour is found for $\bar{\Delta}^{rad} < 0$, with properly switched detuning values. The absence of similar phenomena for $\bar{\Delta}^{rad} = 0$ represents a peculiar signature of mode interference and it is mathematically described by the term $A = \left(1 - \frac{a}{\delta_2}\frac{\eta_2}{\eta_1}\right)$ in Equation 4.8, which is a multiplicative factor for the amplitude of the first mode. Written in explicit form it reads:

$$A = \frac{\omega_{in} - \omega_2^0 + \frac{i}{2}\gamma_2^{nr}}{\omega_{in} - \left(\omega_2^0 + \eta_2^2\bar{\Delta}^{rad}\right) + \frac{i}{2}\left(\gamma_2^{nr} + \eta_2^2\bar{\Gamma}^{rad}\right)} \tag{4.10}$$

and considering the response of the system at the bare frequency of the broad mode $\omega_{in} = \omega_2^0$, it becomes:

$$A^* = \frac{\gamma_2^{nr}}{2i\eta_2^2\bar{\Delta}^{rad} + \gamma_2^{nr} + \eta_2^2\bar{\Gamma}^{rad}} \tag{4.11}$$

In the case of a reactive term larger than the intrinsic decay rate of the broad mode γ_2^{nr}, the following approximation can be applied:

$$\xi = \frac{2i\eta_2^2\bar{\Delta}^{rad}}{\gamma_2^{nr}} \gg 1 \tag{4.12}$$

and the term A^* consequently drops to low values. In this situation, when the spectral position of the first mode resonance coincides with the broad mode bare frequency $\omega_1 = \omega_2^0$, the amplitude associated to the first mode becomes negligible and no evidence of its excitation is found in the waveguide output. A physical explanation to this suppression is obtained by looking at the two terms in $A = \left(1 - \frac{a}{\delta_2}\frac{\eta_2}{\eta_1}\right)$. The first term, which is multiplied by η_1 in Equation 4.8, describes the direct excitation of the narrow mode from the waveguide, while the second term describes the excitation of the first mode by the broad resonance through the waveguide. When these two factor equals A=0, therefore the narrow resonance vanishes in the spectrum. As it has been already discussed, this happens for $\omega_1 = \omega_2^0$. This effect is observed for all the three investigated regimes (panels (c), (f) and (i)), where $\xi \sim 6$ and $\omega_1 = \omega_2^0$ at $\delta = 3.1$ for all the three cases. Indeed, a strong mode suppression is found for $\delta = 3$. The phenomenon is found for both positive and negative values of the reactive term, the only difference being an inverted sign for the detuning ($\delta = -3$ for $\bar{\Delta}^{rad} < 0$) to obtain $\omega_1 = \omega_2^0$.

The vanishing narrow resonance is not the only evidence of intermode reactive coupling. The same term A is responsible also for the EIT effect observed for $\delta = 0$ when $\bar{\Delta}^{rad} \neq 0$. Indeed, the term A evaluated at the center of the broad peak ($\omega_{in} = \omega_2^0 + \eta_2^2\bar{\Delta}^{rad}$) results in:

$$A^{**} = \frac{\eta_2^2\bar{\Delta}^{rad} + \frac{i}{2}\gamma_2^{nr}}{\frac{i}{2}\left(\gamma_2^{nr} + \eta_2^2\bar{\Gamma}^{rad}\right)} \tag{4.13}$$

Exploiting the condition expressed in Equation 4.12 on the reactive term, the A^{**} term becomes:

$$A^{**} \sim \frac{2\eta_2^2\bar{\Delta}^{rad}}{i\left(\gamma_2^{nr} + \eta_2^2\bar{\Gamma}^{rad}\right)} \tag{4.14}$$

which becomes much larger than 1, in modulus, when the reactive term is larger than the overall losses of the broad mode. This is the case of the three simulated regimes, where the reactive term is about six times the resonator losses for the broad family. Therefore, when the narrow mode resonant frequency approaches the broad mode frequency (i.e. null detuning), its contribution to the output signal is enhanced with respect to the $\Delta = 0$ case. This is clearly visible in all the coupling regimes (highlighted in panel (f)), where the tiny feature observed for the first mode at $\delta = 0$

in the $\bar{\Delta}^{rad} = 0$ case becomes a strong mark in the overall transmittance shape when $\Delta \lessgtr 0$.

A different insight on the system response can be found by considering two new variables:

$$\beta_1 = \frac{\eta_1\alpha_1+\eta_2\alpha_2}{2} \quad , \quad \beta_2 = \frac{\eta_1\alpha_1-\eta_2\alpha_2}{2} \tag{4.15}$$

The transmittance is then computed as (see Equation 4.7): $t(\omega_{in}) = 1-2i\Gamma^{rad}\beta_1(\omega_{in})$. This transformation can be seen as a change in our system basis: the two past variables α_1 and α_2, each one defining an individual resonator mode, are now condensed in a single variable, which takes into account both the modes and their interaction. Starting from Equation 4.2, an equation of motion for the new variables can be obtained:

$$\frac{d}{dt}\begin{pmatrix}\beta_1\\ \beta_2\end{pmatrix} = \begin{pmatrix} \Omega^+ + 2\bar{\Delta}^{rad} - i\left[\bar{\Gamma}^{rad}+\gamma^+\right] & \Omega^- - i\gamma^- \\ \Omega^- + 2\eta\bar{\Delta}^{rad} - i\left[\eta\bar{\Gamma}^{rad}+\gamma^-\right] & \Omega^+ - i\gamma^+ \end{pmatrix}\begin{pmatrix}\beta_1\\ \beta_2\end{pmatrix} + \begin{pmatrix}1\\ \eta\end{pmatrix}E_{in} \tag{4.16}$$

with $\Omega^+ = \omega_1 + \omega_2$, $\Omega^- = \omega_1 - \omega_2$ and $\gamma^{\pm} = \frac{\gamma_1 \pm \gamma_2}{2}$. These quantities can be thought as the frequencies and intrinsic losses of supermodes, in a similar description to the standing modes found in the backscattering theory for microresonators (see Chapter 5 or [92]). The parameter $\eta = \eta_2^2 - \eta_1^2$ describes the unbalance in the two mode excitations. Considering an external excitation source $E_{in} = E_0 e^{i\omega_{in}t}$, with few mathematical steps an explicit form for β_1 is found:

$$\beta_1 = \frac{i}{\chi - \psi} \tag{4.17}$$

where:

$$\begin{aligned} \chi(\omega_{in}) &= i\left(\Omega^+ + 2\bar{\Delta}^{rad} - 2\omega_{in}\right) + \left(\bar{\Gamma}^{rad} + \gamma^+\right) \\ \psi(\omega_{in}) &= \frac{\left[i\Omega^- + \gamma^-\right]\left[i\Omega^- + \eta\left(\Omega^+ - 2\omega_{in}\right) + \gamma^- + \eta\gamma^+\right]}{i[\Omega^+ + \eta\Omega^- - 2\omega_{in}] + \gamma^+ + \eta\gamma^-} \end{aligned} \tag{4.18}$$

The transmittance becomes then:

$$t(\omega_{in}) = 1 - \frac{\bar{\Gamma}^{rad}}{\chi(\omega_{in}) - \psi(\omega_{in})} = 1 - \frac{\bar{\Gamma}^{rad}}{\chi(\omega_{in})\left(1 - \frac{\psi(\omega_{in})}{\chi(\omega_{in})}\right)} \tag{4.19}$$

In this new form the transmittance is described as a perturbed Lorentzian: the term χ, without the perturbation ψ, produces the typical Lorentzian dip associated to resonant processes and it embodies the properties of a mean resonator mode with resonance frequency and intrinsic losses in between those of the two coupled modes. The second term, ψ/χ, introduces a perturbation to the mean field and it constitutes

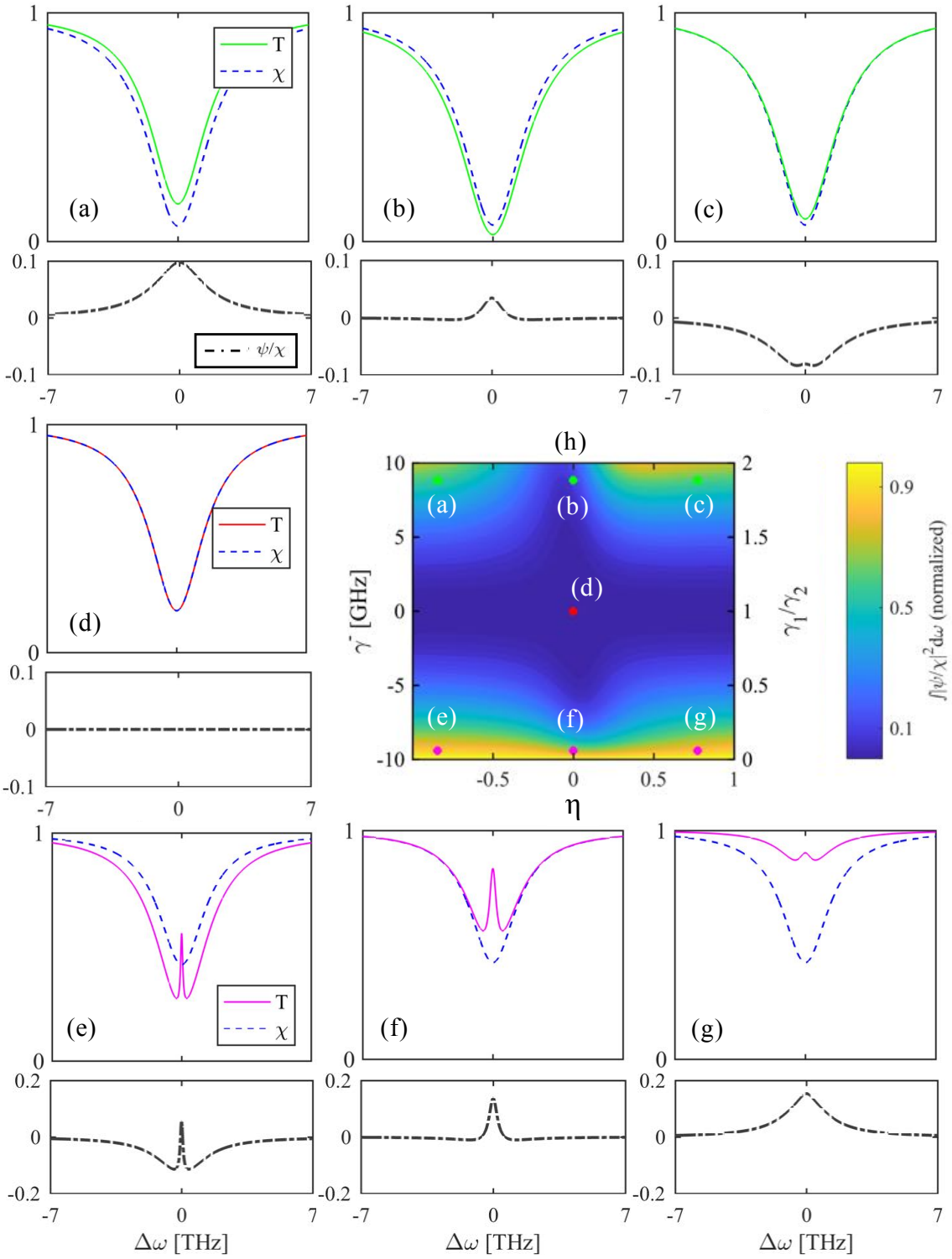

Figure 4.3: (a)-(g) (top): transmittance spectra as obtained from Equation 4.19 (solid line) and mean Lorentzian shape obtained from the same equation for $\psi = 0$ (dashed blue line) for different values of γ^- and η; (a)-(g) (bottom): perturbative term ψ/χ obtained with the same simulative parameters; (h) contour plot of the quantity $\int |\psi/\chi|\, d\omega$ as a function of γ^- and η; coloured circles refer to the parameters used in panels (a)-(g); lighter values in panel (h) refers to larger discrepancy between T and χ curves (as an example, compare panels (e)-(g) with panels (a)-(c)); $\bar{\Gamma}^{rad} = 5GHz$, $\bar{\Delta}^{rad} = 0$ and $\omega_1 = \omega_2$.

the field component related to the difference between the modes. This view becomes particularly useful when the two coupled modes have similar properties: when the intrinsic losses, the resonating frequencies and the excitation strength are equal for the two modes, these are indistinguishable and only the χ term is needed to describe the system response. However, as the two modes differentiate ($\omega_1 \neq \omega_2$, $\gamma_1 \neq \gamma_2$ or $\eta_2 \neq \eta_1$) the perturbative term ψ/χ becomes more and more relevant. In Figure 4.3 panel (h), the amplitude of this perturbative term is computed in its dependence on γ^- and η . In this context, $\omega_1 = \omega_2$ and $\bar{\Delta}^{rad} = 0$ are used to simplify the description of the results provided by the model. As it appears from the contour plot, the intensity of the perturbation is null when $\gamma^- = 0$ and $\eta = 0$ (i.e. when modes are identical). Conversely, its strength is increased as these two parameters get far from 0. A similar result is obtained also by changing the relative detuning between the two families $\omega_1 \neq \omega_2$. The effect of the perturbative term can be observed also in the different spectra related to different γ^- and η values (panels from (a) to (g)). In particular, in the top figure of each panel the actual transmittance computed from Equation 4.19 is compared to the one obtained with the only χ term (labeled χ in the figure). The difference between these two curves is due to the presence of a non null perturbative term ψ/χ, which is represented in the bottom figure of each panel.

Interestingly, the new description of the system response that is obtained in this formulation is complementary to the one discussed above and represented by Equation 4.8. Indeed, this new tool allows to recognize the presence of coupled modes in the case of quasi degenerate modes, when the Lorentzian shape is barely influenced by the mode interaction. Conversely, when the two coupled modes show markedly different parameters the term ψ/χ is no more negligible with respect to the χ term associated to the mean Lorentzian and the description of the system response becomes less intuitive. Therefore, in this last case the description through Equation 4.8 is more useful.

4.3 Experimental results

In order to verify the results predicted by the theoretical model presented in the previous Section, transmittance and phase measurements on a vertically coupled resonator have been performed. The system consist of a $20\mu m$ radius SiN disk microresonator similar to the wedge investigated in Chapter 3 [2]. Schematic representation of the system is provided in Figure 4.4 (left).

In Figure 4.5, the transmittance spectrum of the device is shown and the periodic resonances of three different TE polarized radial mode families are found. A FSR analysis allows to identify them as the 1^{st}, 2^{nd} and 3^{rd} order families as indicated in figure. The effective refractive index and the electric field distribution of these three modes are shown in Figure 4.4. In the following we focus our attention on

[2] the resonator is very similar to the one presented in Section 3.4, with the only difference laying in the final (dry) etching process.

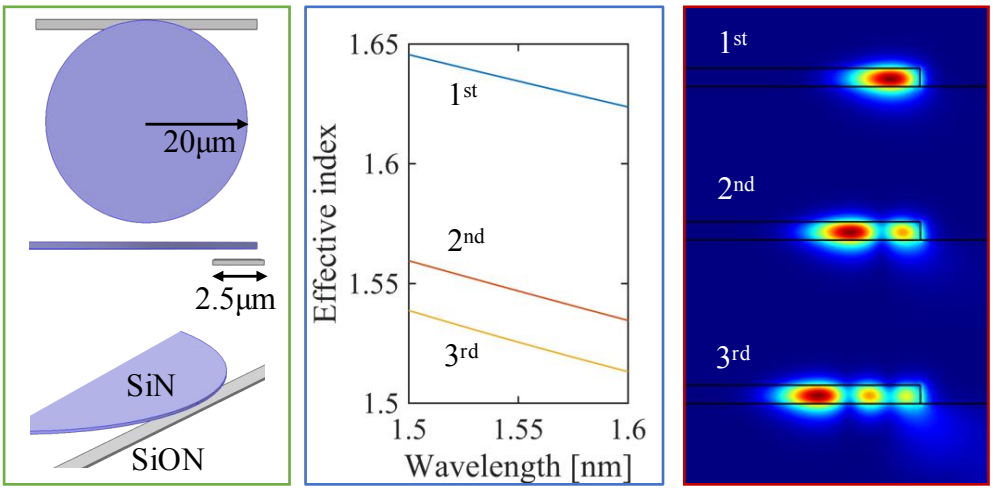

Figure 4.4: (left) Schematic representation of the investigated structure; waveguide and resonator height are 250nm and 350nm respectively; (center) resonator TE mode effective refractive indexes and (right) electric field profiles at $\lambda = 1.5\mu m$.

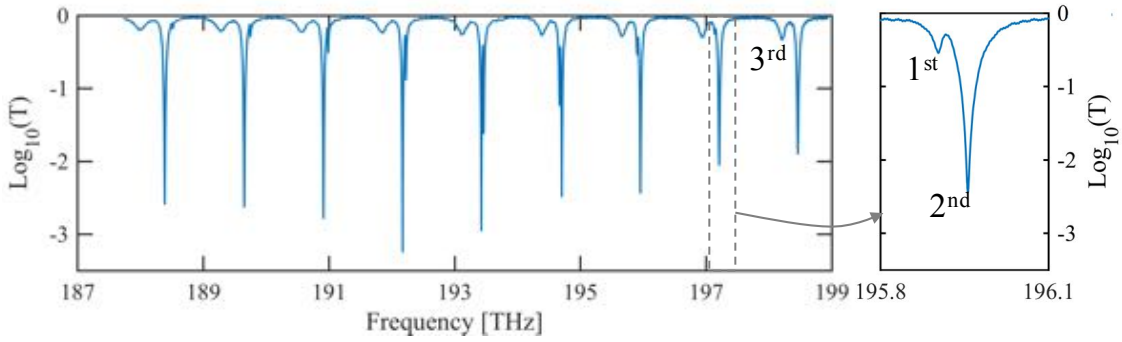

Figure 4.5: (left) transmittance spectrum of the investigated device showing broad and weak features related to the 3^{rd} radial family and much stronger signatures of a critically coupled 2^{nd} radial family; (right) zoomed view of the 2^{nd} family resonance revealing a weakly coupled resonance associated to the 1^{st} radial family.

the first two radial orders, whose small resonance detuning allows to investigate the predicted intermode coupling. The selective excitation provided by vertical coupling is here a fundamental property, which allows the efficient excitation of multiple modes to be tuned. In this case, the simultaneous excitation of a critically coupled broad family and of a narrow undercoupled family allows a more clear observation of the fine features predicted by the model. Moreover, in order to obtain a more accurate insight on the system, the interferometric setup presented in Chapter 2 is used to acquire both the transmittance and the phase spectra of the two resonances. These are shown in Figure 4.6 for nine consecutive azhimutal numbers ($m_1 = 122 : 130$, $m_2 = 115 : 123$). Fortunately, the slightly different FSR of the two involved families allows to investigate the doublet in different configurations. Indeed, skimming the different panels of Figure 4.6 from left to right (i.e. looking at successive resonance peaks) the narrow peak associated to the first order mode is observed to completely cross

the larger peak of the second mode, thus resulting each time in a different frequency detuning between the two modes [3]. As a first evidence, different extinction ratios of the narrow mode are observed when it lays on the blue or on the red part of the broad mode (compare for example panels (a-b) with panels (h-i)). This asymmetric behaviour indicates the occurrence of a reactive interaction between the two modes. A definitive signature of reactive coupling is observed in the central panels (d-e-f), where the amplitude of the narrow mode is greatly enhanced with respect to initial and final panels. This experimental configuration, with an almost critically coupled broad family crossed by a narrow undercoupled one corresponds to the top panels of Figure 4.2. In particular, the simulation for $\bar{\Delta}^{rad} > 0$ (panel (c)) qualitatively matches the experimental data, with an enhanced interference between the two modes for null detuning and a vanishing narrow dip for positive detunings, when it lays on the red part of the broad family. Comparison with panel (b) of the same figure confirms that such a strong alterations in the transmittance cannot be explained without a reactive component in the coupling.

In this context, phase measurements allows a definite evaluation of the coupling regime for the two families. In particular, the narrow family is always found in undercoupled configuration, its phase shift being limited to π. On the other hand, the broader second family crosses the critical condition in between panel (d) and (e). In these panels the phase variation associated to the second mode decreases from about 2π to less than π indicating a change of coupling regime. This evidence is confirmed by transmittance analysis: the 2^{nd} family in Figure 4.5 shows a net oscillation in its extinction ratio, with the lowest value reached at about 192 THz. This is a clear evidence for a change in the coupling regime. Actually, the phase response remains a more reliable tool, and it becomes essential in the case of vertically coupled structures, where an oscillation in the ER can be related to a mode going to both under or over coupled regime (see Chapter 3).

The information brought by transmittance and phase measurements can be also combined in a phasor plot to evidence the occurring physical phenomena: looking at the three phasor plot shown in Figure 4.6 two circles can be identified, a larger one and a smaller one, related to the broad and narrow resonances, respectively. The small circle is observed to increase its radius in the central plot: this means an enhanced excitation of the 1^{st} radial mode, which confirms the results obtained from transmittance analysis.

Another improvement given by phase acquisition is the possibility to perform simultaneous fitting of transmittance and phase data, with an increased accuracy on the results. Simultaneous fitting of the transmittance and phase data shown in Figure 4.6 with Equation 4.8 results in the red curves. The almost perfect superposition of the two curves confirms the correctness of the model and the great accuracy of the setup used for the acquisition of the data. From the fit some system parameters can

[3] A similar crossing phenomenon driven by thermo-optic effect has been demonstrated in the same device [93].

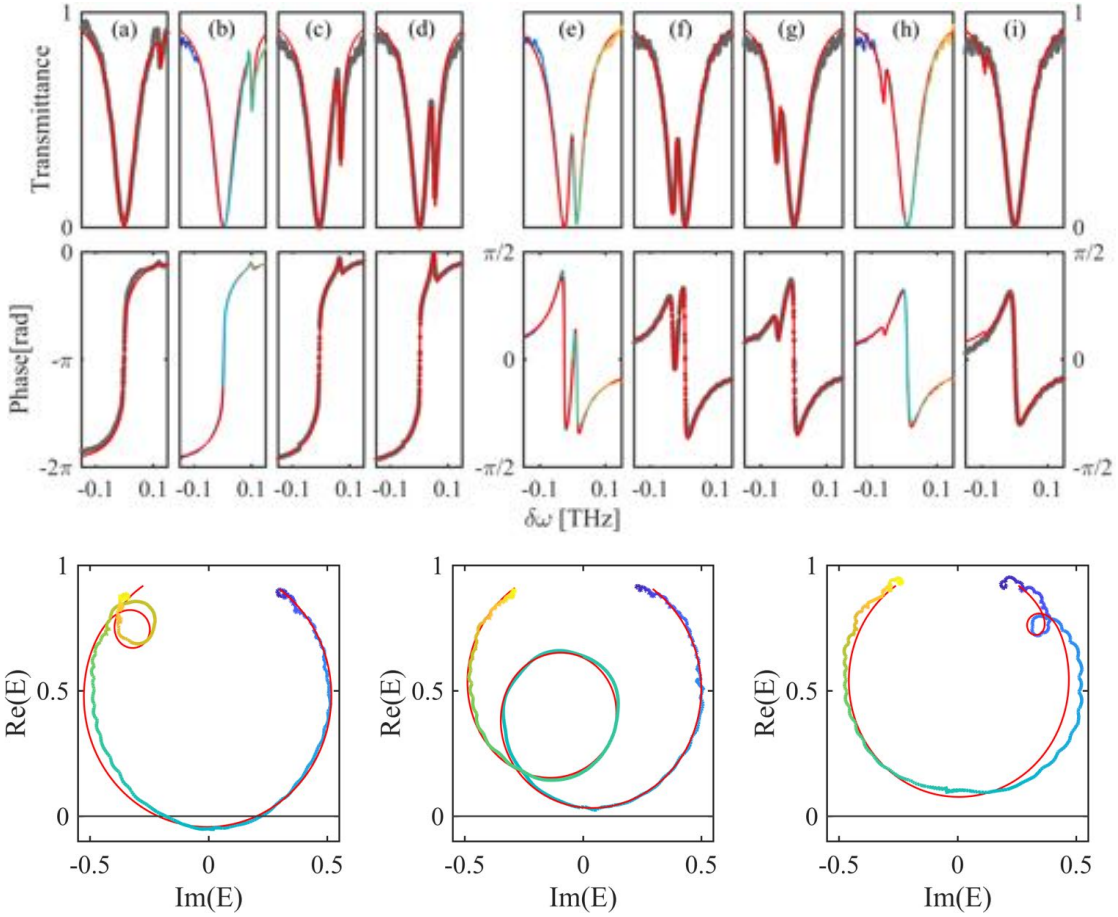

Figure 4.6: Transmittance and phase of the tested disk microresonator: (top) experimental (grey) and fitted (red) curve as obtained from Equation 4.19; (bottom) phasor plot (experimental and fitted curves) of panel (b)-(e)-(h); black horizontal line helps to distinguish between under and over coupled modes.

be obtained in their evolution with frequency. In Figure 4.7 the extrinsic over intrinsic losses parameter Γ_i^{rad}/γ_i for the two coupled families and the reactive term Δ_{12}^{rad} are depicted. As expected, the coupling ratio decreases with frequency for the 2^{nd} mode and it crosses the critical coupling condition at about 193 THz (corresponding to panels (d)-(e) of Figure 4.6). Interestingly, the coupling of the 1^{st} mode increases with frequency, thus indicating a more coupled condition at higher frequencies. This should bring to an increasing signature of the narrow family with frequency. Conversely, comparing panels (a-b) with (h-i) the 1^{st} mode weakens with frequency. This is another evidence of the mode suppression provided by the reactive component of the coupling. Indeed, as expected from a comparison between simulated and experimental data, a positive off-diagonal reactive component (Δ_{12}^{rad}) of about 15 GHz is found from the fitting procedure. Actually, fitting of the data with negative values for the reactive term is possible, with similar values for the Sum of Squared Errors. However, the lack of physical interpretation of a negative term allows to discard them as unrealistic results.

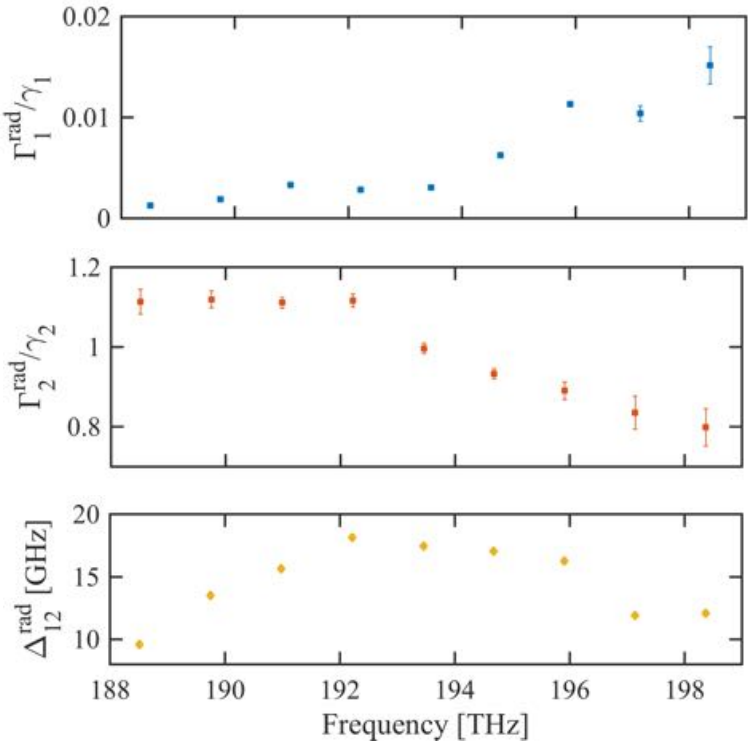

Figure 4.7: Extrinsic over intrinsic decay rates for the 1^{st} (top) and 2^{nd} (middle) modes as obtained from fitting of the experimental data shown in Figure 4.6; (bottom) off-diagonal reactive term Δ_{12}^{rad} as obtained from the same fitting procedure (error bars not shown because too small to be visible).

A final measurement is presented to stress the importance of acquiring also the phase response of a device. In Figure 4.8 the transmittance and phase of a microring resonator similar to the one investigated before is shown. The transmittance spectrum contains only one resonant peak at about 1575nm, thus indicating a single mode operation of the device. However, looking at the phase spectrum, the feature of a second coupled mode arises as an additional 2π shift at about 1577nm. This information is completely hidden in the transmittance due to the strongly overcoupled regime of the mode. Fitting of the experimental data with Equation 4.19 confirms this hypothesis, returning an extrinsic over intrinsic loss ratio much larger than one ($\Gamma_1^{rad}/\gamma_1 \sim 16$). With this simple evidence, phase measurements are demonstrated to give remarkable information on a resonator-waveguide system and they justify the acquisition of data through interferometric setup to extract not only the amplitude but also the phase of the outcoming signal.

4.4 Conclusion and perspectives

In the present study the mutual coupling between different radial mode orders of a vertically coupled microresonator has been investigated. The theoretical model pre-

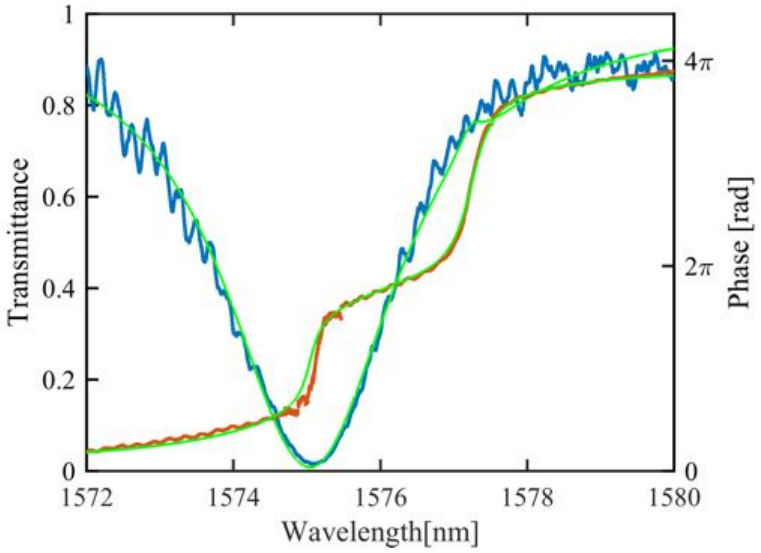

Figure 4.8: Experimental and fitted (with Equation 4.19) transmittance and phase of a SiN vertically coupled microring resonator: a single mode spectrum in the transmittance turns out to contain two resonant modes when the phase spectrum is observed.

sented in [13] has been discussed in the case of a resonator supporting two modes, with one narrow and one broad family of resonances in its spectrum. The introduction of dissipative coupling between modes showed asymmetries in the narrow features, which can be explained as Fano lineshaped resonances in analogy to the Fano resonances observed in the atomic context. Coupling has been characterized also by a reactive component, which is demonstrated to strongly perturb the system response: it brings to enhanced EIT effect when a small detuning between the two families occurs and it leads to complete suppression of the narrow family when this resonates at the broad mode bare frequency. Explanation to these effects has been provided and their manifestation in a real device has been experimentally proven. In this sense, the experimental choice of a vertically coupled structure had been fundamental to observe the coupling related effects. Indeed, the vertical coupling configuration allowed two different modes to be effectively excited over a wide spectral range. This fact, together with the variable detuning between the two families due to their different free spectral range, provided an optimal experimental platform to test the theoretical model. Both mode enhancement and suppression had been observed and good agreement between experimental data and simulated one has been found. Experimental acquisition of the phase response of the system increased the accuracy of the fitting procedure and, moreover, it gave a much more reliable insight on the coupling regime of each coupled mode.

The increased resonance slope that is found in Fano resonances and the sharp variation of transmittance observed in EIT effect suggest several potential applications for the device. Indeed, EIT/Fano based biochemical sensors, low power switching

devices and all optical delay lines had already been proposed [85, 94, 95, 96, 97, 98][4]. Some of the proposed platforms exploiting microresonators suffer from lack of integration, as it is the case of microspheres [91], or they need coupling of multiple cavities [83], with consequent complications in the fabrication process and/or a low production yield. Moreover, tuning of mode resonating frequencies is accomplished by moving the tapered fiber or by changing the separation between resonators, which bring to impractical devices. In this sense, the investigated vertically coupled platform offers an all-integrated device where all optical tuning of the mode interference can be accomplished: by change of the azimuthal mode number (as shown in Section 4.3) or exploiting the thermo optic effect (as demonstrated in [93]). In addition, different displacement of the waveguide can change the excitation of the involved modes (Section 3.4.2) and constitutes an additional degree of freedom in the design of the device. Despite the variety of application, intermode coupling and the consequent perturbation of the spectrum can become detrimental effect for a proper use of the device. Unfortunately, intermodal coupling seems to be a phenomenon intrinsically tied to vertical coupling, as it appears anytime two guided modes are found at similar frequencies; neither the use of different resonator geometries, such as wedge resonators, nor the movement of the waveguide to different vertical and horizontal gap seems to modify the strength of this phenomenon (see results described in 3). In this sense, the most practical solution to mitigate this effect is to excite only one resonator mode by tuning the waveguide horizontal position. In order to maintain multimode operation of the resonator, another more complicate approach can be used, based on the thermo optic effect: by means of selective heaters the relative position between resonances can be tuned, in a similar fashion to what is described in [93], and spectra with isolated resonances can be obtained.

Future experiments should regard devices with coupled modes showing similar characteristic parameters (intrinsic/extrinsic losses and resonant frequency), to verify the model based on a perturbative approach (see Equation 4.19) and to evidence the contribution of the reactive and dissipative components for nearly degenerate modes. Interestingly, a similar analysis on coupled counterpropagating modes is proposed in the next Chapter 5, where the parameters $\Omega^{\pm}$ and $\gamma^{\pm}$ are used to describe the properties of symmetric and antisymmetric supermodes.

[4]Noticeably, the research for an effective delay line requires accurate phase measurements, to monitor the change in group delay that is introduced by EIT/Fano effects.

Chapter 5

A model for backscattering in microresonators

5.1 Introduction to backscattering

Despite the complex dynamics that have been described in the previous chapters (see Chapter 3 and 4), only one direction of propagation for the resonating mode was considered (the one excited by the waveguide). However, the always present sidewall roughness causes excitation of a resonator mode travelling in the opposite direction with respect to the waveguide excited one [99, 100]. This phenomenon is commonly referred as backscattering and it has largely been observed in microresonators [101, 102]. The presence of two propagating modes with opposite direction creates two standing modes inside the resonator, which are usually labeled as *symmetric* and *antisymmetric* modes [92]. The roughness mediated coupling of clockwise (*cw*) and counterclockwise (*ccw*) modes lifts the degeneracy of the symmetric and antisymmetric standing modes [92]; this results in a resonance frequency split and gives rise to what is called a *backscattering doublet* (Figure 5.1). From an experimental point of view, this resonance splitting is usually not visible in high loss microresonators; indeed, despite this roughness induced degeneracy is present in all microresonators, the large resonance width produced by other loss channels hides the small frequency split caused by backscattering. Conversely, in a high-Q resonator the narrow resonance width makes the observation of backscattered modes a more probable event. On one side, the presence of split resonances becomes useful for several on-chip applications, from fast light propagation [101] to second order filtering [103, 104] and particle detection [105]. On the other side, it can represent a detrimental and unwanted source of loss for a resonator and it can severely affect its properties [106]. In this sense, promising results to avoid backscattering signatures have been obtained: tuning of the mode frequency splitting up to an entire free-spectral range allows to pass from half FSR spaced doublets to the complete degenerate counter-propagating modes [107, 108]. The drawback of this solution is the presence of a large integrated loop mirror element, which decreases the resonator FSR and increases the

device footprint.

In order to design devices able to cancel or to take advantage of the backscattering, a proper theoretical model is needed. Indeed, several models have been proposed to fully characterize this phenomenon [109, 110, 111, 112]. However, only symmetric resonance doublets are predicted by these models, while experiments show clear asymmetry in the doublet [27, 113]. Recently, the backcoupling occurring at the waveguide-resonator coupling region has been proven to be a possible source for this asymmetry [92, 114]. However, asymmetric resonances are observed also in large radii resonators [12], where the backcoupling term is considered to be negligible and can not be solely the source for the asymmetry.

The present Chapter contains a theoretical, simulative and experimental investigation on a new general model of backscattering in microresonators. The model is able to describe both the presence of symmetric doublets and the appearance of the more elusive doublet asymmetry even in low power conditions and for large radii resonators. Based on the strong analogy between the coupling dynamics of multiple copropagating modes in a microresonator (Chapter 4) and the mutual coupling of counterpropagating modes through sidewall roughness, the model contemplates both imaginary and real components of the mode coupling coefficient. A more in depth description of the model is provided in Section 4.2, where the approximations, the mathematical and physical meaning of the different terms and the predictive results are explained. Section 5.3 shows the results of FEM 2D simulations to verify the assumptions and the approximations contained in the model. Experiments on a vertically coupled microresonator showing backscattering doublets are presented in Section 5.4 to validate the model predictions. In Section 5.5, the discussion moves to the different issues related to doublets identification and classification. In particular, a new tool for the analysis of resonance doublets is proposed. Starting from the acquisition of phase and transmittance spectra, an inverse phasor representation is used to identify the existence of mode splitting with extreme sensitivity. In addition, different methods for the classification of doublet asymmetry are proposed.

5.2 Model description

The theoretical model developed to describe the dynamics of *cw* and *ccw* modes takes into account the main backscattering sources already proposed in literature and introduces new channels to explain the doublet properties. In particular, the considered platform is a microresonator coupled to its bus waveguide; following the model proposed in Chapter 4 no specific coupling configurations are here considered. This choice allows to simplify the mathematical treatment of the subject by exploiting TCMT and returns a general model, which can be applied to both in plane and vertically coupled resonators. Indeed, as it will be explained, the backscattering process mainly originates inside the resonator volume and it is not affected by the coupling dynamics.

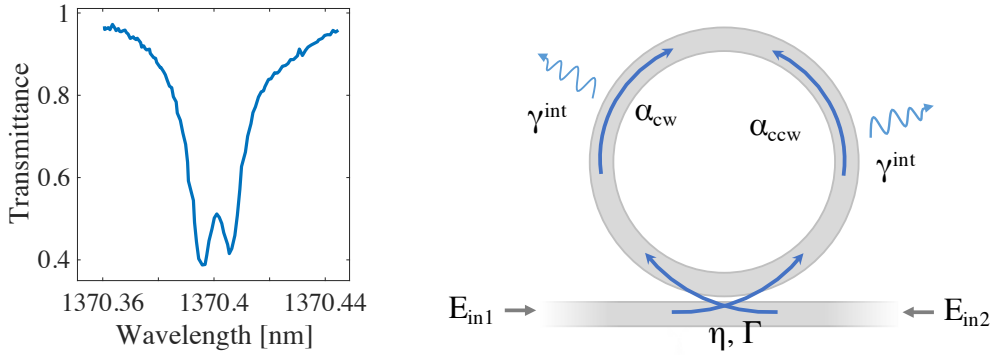

Figure 5.1: (left) Experimental doublet in a microresonator transmittance spectrum and, (right) schematic representation of the considered resonator model: a two port excitation sustains clockwise (cw) and counterclockwise (ccw) modes inside the microresonator, which are characterized by intrinsic losses γ^{int} and external coupling coefficient η.

As a first step, it is useful to recall the most simple equation for a singlemode resonator already described in Section 3.1:

$$\frac{d\alpha}{dt} = \left(i\omega_0 - \gamma^{int} - \Gamma\right)\alpha + i\eta E_{in} \tag{5.1}$$

The evolution of the resonator field α is dependent on the resonating frequency ω_0, on the intrinsic and extrinsic decay rates (γ^{int} and Γ, respectively) and on the coupled input field ηE_{in}. Generalization of this formula to the case of two excitation ports (Figure 5.1) and two propagating fields (the *cw* and *ccw* modes) results in:

$$\begin{cases} \frac{d\alpha_{cw}}{dt} = \left(i\omega - \gamma^{int} - \Gamma\right)\alpha_{cw} + i\eta E_{in1} \\ \frac{d\alpha_{ccw}}{dt} = \left(i\omega - \gamma^{int} - \Gamma\right)\alpha_{ccw} + i\eta E_{in2} \end{cases} \tag{5.2}$$

The same equation condensed in matrix form becomes:

$$\frac{d\boldsymbol{\alpha}}{dt} = \left(i\boldsymbol{\omega} - \boldsymbol{\gamma^{int}} - \boldsymbol{\Gamma^{ext}}\right)\boldsymbol{\alpha} + i\boldsymbol{K}\boldsymbol{E_{in}} \tag{5.3}$$

where the different matrices are:

$$\begin{gathered} \boldsymbol{\alpha} = \begin{pmatrix} \alpha_{cw} \\ \alpha_{ccw} \end{pmatrix}, \ \boldsymbol{\omega} = \begin{pmatrix} \omega & 0 \\ 0 & \omega \end{pmatrix}, \ \boldsymbol{\gamma^{int}} = \begin{pmatrix} \gamma^{int} & 0 \\ 0 & \gamma^{int} \end{pmatrix} \\ \boldsymbol{K} = \begin{pmatrix} \eta & 0 \\ 0 & \eta \end{pmatrix}, \ \boldsymbol{E_{in}} = \begin{pmatrix} E_{in1} \\ E_{in2} \end{pmatrix} \end{gathered} \tag{5.4}$$

The same resonator mode is considered to be excited in the two directions, thus giving equal resonating frequencies, coupling coefficients η and intrinsic / extrinsic decay rates γ^{int}/Γ. The matrix $\boldsymbol{\Gamma^{ext}}$ for the extrinsic decay rate of the system is found from energy conservation: [87]:

$$2\boldsymbol{\Gamma}^{\boldsymbol{ext}} = \boldsymbol{K}^{+}\boldsymbol{K} \tag{5.5}$$

where the $^{+}$ symbol denotes the Hermitian adjoint. This returns:

$$\boldsymbol{\Gamma}^{\boldsymbol{ext}} = \begin{pmatrix} \frac{\eta^2}{2} & 0 \\ 0 & \frac{\eta^2}{2} \end{pmatrix} \tag{5.6}$$

As it appears from the diagonal form of the different matrices defined in Equation 5.4, no coupling between the two modes has been inserted up to now and the system describes the independent propagation of *cw* and *ccw* modes.

In general, the coupling between modes can be found both inside and outside the resonator. The inner coupling is related to the sidewall roughness of the microresonator and it is spread along the whole resonator circumference [99]. In our model, the strength of this coupling source is described by the coupling parameters β_{12} and β_{21} and it affects the non diagonal elements of the intrinsic matrix, which becomes:

$$\boldsymbol{\gamma}^{\mathbf{int}} = \begin{pmatrix} \gamma^{int} & \beta_{12} \\ \beta_{21} & \gamma^{int} \end{pmatrix} \tag{5.7}$$

The outer coupling source is found at the coupling region, where a portion of the waveguide field can be scattered back into the *ccw* mode [102]. Indeed, the effective index variation felt by the waveguide mode when approaching the resonator can bring to a partial reflection of the field. To this process is associated the backcoupling parameter η_{bc}, which appears in the coupling matrix as:

$$\boldsymbol{K} = \begin{pmatrix} \eta & \eta_{bc} \\ \eta_{bc} & \eta \end{pmatrix} \tag{5.8}$$

The extrinsic loss matrix is consequently modified to fulfill Equation 5.5, which returns:

$$\boldsymbol{\Gamma}^{\boldsymbol{ext}} = \begin{pmatrix} \frac{\eta^2+\eta_{bc}^2}{2} & \eta\eta_{bc} \\ \eta\eta_{bc} & \frac{\eta^2+\eta_{bc}^2}{2} \end{pmatrix} \tag{5.9}$$

Defining an extrinsic decay rate $\Gamma = \eta^2/2$ and backcoupling decay rate $\Gamma_{bc} = \eta_{bc}^2/2$, the extrinsic matrix can be rewritten in a more usual form as:

$$\boldsymbol{\Gamma}^{\boldsymbol{ext}} = \begin{pmatrix} \Gamma + \Gamma_{bc} & 2\sqrt{\Gamma\Gamma_{bc}} \\ 2\sqrt{\Gamma\Gamma_{bc}} & \Gamma + \Gamma_{bc} \end{pmatrix} \tag{5.10}$$

and the coupling matrix becomes:

$$\boldsymbol{K} = \begin{pmatrix} \sqrt{2\Gamma} & \sqrt{2\Gamma_{bc}} \\ \sqrt{2\Gamma_{bc}} & \sqrt{2\Gamma} \end{pmatrix} \tag{5.11}$$

From Equation 5.3, considering only one port excitation ($E_{in2} = 0$), the equation of

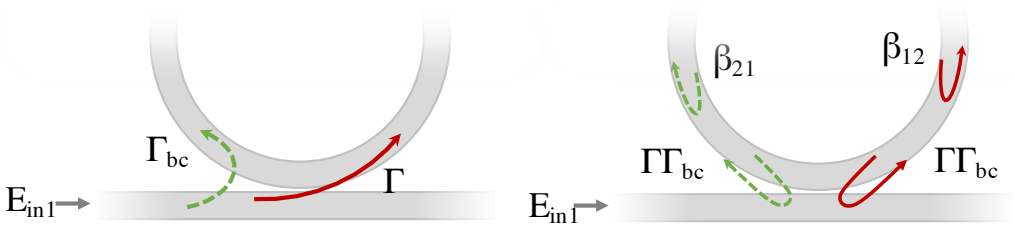

Figure 5.2: Schematic representation of the different excitation sources for the *ccw* (red lines) and *cw* (green-dashed line) modes considered in the model.

motion for two interacting *cw* and *ccw* fields is then obtained:

$$\begin{cases} \frac{d\alpha_{cw}}{dt} = (i\omega - \gamma^{int} - (\Gamma + \Gamma_{bc}))\,\alpha_{cw} - \left(2\sqrt{\Gamma\Gamma_{bc}} + \beta_{21}\right)\alpha_{ccw} + i\left(\sqrt{2\Gamma_{bc}}E_{in1}\right) \\ \frac{d\alpha_{ccw}}{dt} = (i\omega - \gamma^{int} - (\Gamma + \Gamma_{bc}))\,\alpha_{ccw} - \left(2\sqrt{\Gamma\Gamma_{bc}} + \beta_{12}\right)\alpha_{cw} + i\left(\sqrt{2\Gamma}E_{in1}\right) \end{cases} \tag{5.12}$$

The different excitation sources for the *cw* and *ccw* modes are schematically represented in Figure 5.2. In particular, in addition to the direct excitation from the waveguide, the *ccw* mode can be excited by internal coupling of the *cw* mode (β_{12}). Conversely, the *cw* mode receives indirect excitation from the backcoupled light coming from the waveguide field ($\sqrt{2\Gamma_{bc}}$) and from the internal coupling with the *ccw* mode (β_{21}). Finally, there is another coupling process, valid for both the modes, where the propagating mode inside the resonator can couple to the bus waveguide and be successively backcoupled to the opposite resonator mode ($\Gamma\Gamma_{bc}$). From this picture it becomes evident the different role of intrinsic and extrinsic coupling mechanism. The first acts only on the coupling between the two resonator modes, whereas the second modifies also the coupling between the resonator and the bus waveguide.

Before moving to a more specific analysis of the system response, some useful considerations on the mode coupling coefficients β_{12}, β_{21} and Γ_{bc} should be done.

A first important remark regards the coupling terms β_{12} and β_{21}: the model treats them as complex numbers, with real and imaginary components describing dissipative and reactive features of internal mode coupling, respectively. Despite this fact has already been proposed in other models [92], the most common ones usually take into account only the reactive term. In our case, the dissipative feature of the inner coupling is considered to originate from the multimodal nature of the microresonator: the possibility to transfer power to higher order modes during backscattering opens an additional loss channel that is not present in singlemode resonators[1].

A second note regards the relation between β_{12} and β_{21}. The isotropic distribution and orientation of sidewall defects and the field profiles associated to the *cw* and *ccw* modes suggest the existence of a symmetric coupling dynamics. Consequently, equal

[1]To be consistent with experimental observations, the 1^{st} order radial mode is considered as the main excited mode.

coupling coefficients can be used ($\beta_{12} = \beta_{21} = \beta$) without affecting the generality of the model and without alteration on the model predictions on real systems.

A final relevant note concerns the backcoupling term (Γ_{bc}). This external coupling element is considered to be negligible with respect to the inner term when resonators with radius larger than $10\mu m$ are used [102]. In this condition, the long and progressive approaching between the waveguide and the resonator creates an adiabatic variation in the mode effective index, which results in a negligible reflection coefficient. Since our simulative and experimental examples consist in resonators with $20\mu m$ and $25\mu m$ radii, respectively, it is possible to neglect the backcoupling term from Equation 5.12 without significant deviations from the real dynamics[2]. Actually, the contribution to Γ_{bc} does not come only from the reflection due to effective index variation, but also from the enhanced reflection along the coupling region. In this region, the electromagnetic field is more concentrated along the rough waveguide and resonator sidewalls, and this brings to an increment in the overall reflected field. Nonetheless in our experiment, the use of the vertical coupling geometry makes this effect negligible. Indeed, in this geometry the electromagnetic field of the modes is mainly concentrated along the top and bottom surfaces of the waveguide and resonator, respectively, and not on their sidewalls. Therefore, the lower degree of roughness associated to horizontal surfaces results in lower backscattering strength.

In these conditions, from Equation 5.12, considering a monochromatic excitation source $E_{in} = E_0 e^{i\omega_{in} t}$ and performing similar mathematical steps to those described in Section 4.2, it is possible to extract the stationary *cw* and *ccw* field amplitudes ($\bar{\alpha}_{cw}$ and $\bar{\alpha}_{ccw}$). The response of the system for a one port excitation is then obtained from the interference between the input and the *ccw* waves weighted by the coupling coefficient:

$$\begin{aligned} t(\omega) &= 1 + i\sqrt{2\Gamma}\bar{\alpha}_{ccw}(\omega) \\ &= 1 - \frac{2\Gamma}{(i\delta\omega + \gamma^{int} + \Gamma) - \frac{\beta^2}{(i\delta\omega + \gamma^{int} + \Gamma)}} \end{aligned} \tag{5.13}$$

where $\delta\omega = \omega - \omega_{in}$ is the relative detuning between the input laser frequency ω_{in} and the mode resonant frequency ω. Interestingly, the form of Equation 5.13 highly resembles that of Equation 4.19 and suggests some useful comparisons. The copropagating and counterpropagating modes of the present case are related to the 1^{st} and 2^{nd} copropagating modes of the multimodal resonator and, similarly, the mode interaction that previously was mediated by the waveguide is here represented by sidewall roughness. This analogy suggests once more to consider both dissipative and reactive effects in the coupling between backscattered modes. Hence, the mode interaction in the model is described by two coefficients β_r and β_i, which constitute the interaction

[2] Additionally, the wedge shape of the experimentally tested resonator produces an even more adiabatic alteration of the effective index in the coupling region with respect to common disk resonators.

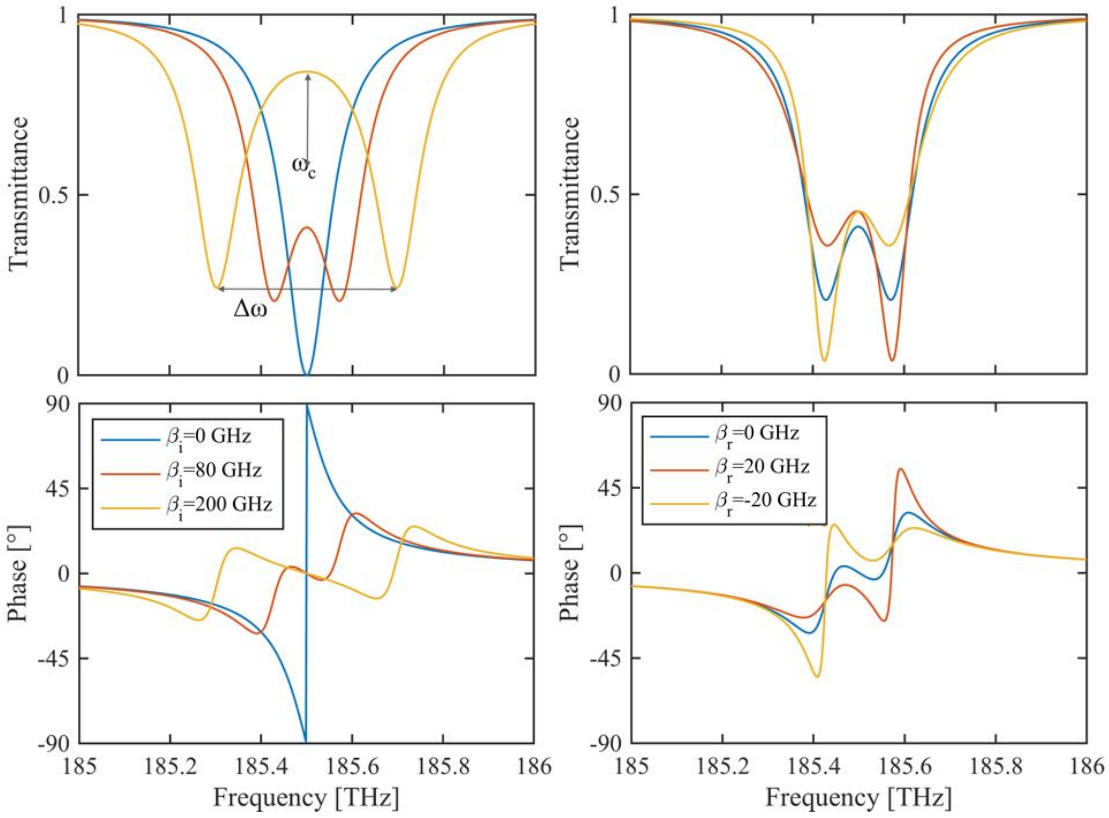

Figure 5.3: Transmittance and phase spectra as resulting from Equation 5.13 for varying values of (left) β_i and (right) β_r, with $\beta_r = 0$ and $\beta_i = 80GHz$, respectively; resonant frequencies of the top-right panel have been shifted for ease of visualization.

coefficient $\beta = \beta_r + i\beta_i$. Then, to characterize the action of these two parameters on the system response, the transmittance and the phase, computed as $T = |t|^2$ and $\varphi = \arg(t)$, can be simulated for different values of β_i and β_r (Figure 5.3).

Actually, a more clear view of the action of β_r and β_i on the doublet shown in the figure can be reached looking at the resonator symmetric and antisymmetric solutions. Indeed, the superposition of *ccw* and *cw* waves inside the resonator creates symmetric and antisymmetric standing waves [92], whose amplitudes α^+ and α^- can be defined as:

$$\alpha^+ = \frac{\alpha_{ccw} + \alpha_{cw}}{\sqrt{2}} \quad \alpha^- = \frac{\alpha_{ccw} - \alpha_{cw}}{\sqrt{2}} \tag{5.14}$$

This change of variables is very similar to the one performed in Chapter 4 (see Section 4.2) and it recalls the above described analogy between the two physical systems. Substituting Equation 5.14 into Equation 5.12, the equation of motion for these new quantities can be written as:

$$\begin{cases} \frac{d\alpha^+}{dt} = \left(i\omega - \gamma^{int} - \frac{\eta^2}{2} - \beta\right)\alpha^+ + i\left(\eta E_{in}\right) \\ \frac{d\alpha^-}{dt} = \left(i\omega - \gamma^{int} - \frac{\eta^2}{2} + \beta\right)\alpha^- + i\left(\eta E_{in}\right) \end{cases} \tag{5.15}$$

The transmittance of the system computed as:

$$t = 1 + i\eta \frac{(\alpha^+ + \alpha^-)}{\sqrt{2}} \tag{5.16}$$

returns the same result shown in Equation 5.13. Indeed, the only observable we have on the system still remains the power extracted from the *ccw* mode (or from the *cw* one if the E_{in2} port is used as excitation port). However, this new form gives a different and somehow more intuitive description of the system. The amplitudes of the symmetric and antisymmetric modes are closely related to the shape of the doublet, each peak being associated to α^+ or α^- resonances. When the *cw* mode begins to be excited from the backscattered *ccw* mode, the amplitudes and resonating wavelengths of α^+ and α^- cease to be degenerated, as it can be seen from Equation 5.15. As a consequence to this, a split in the spectrum appears, as it is found in the left panels of Figure 5.3. The doublet splitting is mainly affected by the imaginary component of the coupling (β_i) and it is found to be $\Delta\omega_s = 2\beta_i$. In the same figures (Figure 5.3(left)) a variation of the doublet separation is followed by a variation in the doublet transmittance. Equal intrinsic and extrinsic coefficients lead to critically coupled resonances in the case of non interacting modes, as it can be seen from the phase plot. Conversely, the same resonance with the same coefficients passes to the under coupling regime when the mode coupling is turned on. This observation is in accordance to other models [106, 111] and it can be ascribed to the interference between the symmetric and antisymmetric modes at the coupling stage. When a spectral shift between the two modes occurs (i.e. when β_i is different from 0), their superposition produces different values for the overall transmittance. This can be seen from Equation 5.16, where the dependence of the response of the system on the α^+ or α^- superposition is made explicit. Increasing the spectral distance, the transmittance minima stabilize to a fixed level, because of a lower superposition between the two fields is found. For what concerns the influence of the dissipative component of the coupling (β_r), it can be seen from Figure 5.3 that it mainly affects the symmetry and the linewidth of the doublet. The same prediction follows from Equation 5.13. As a real number, β_r constitutes a source of loss for one mode and a source of gain for the other mode, depending on its sign. Consequently, an unbalance in the intrinsic losses between α^+ and α^- results in a different intrinsic/extrinsic coupling ratio[3]. This gives different transmittance minima and linewidths.

5.3 Simulations

The above described model assumes the existence of a real component in the coupling between the *ccw* and *cw* modes and foresees the origin of this component in the

[3]In the following, the word "unbalance" and "asymmetry" are used to refer to the same spectral feature, the first recalling more the physical principle originating the doublet, the second being more related to its manifestation.

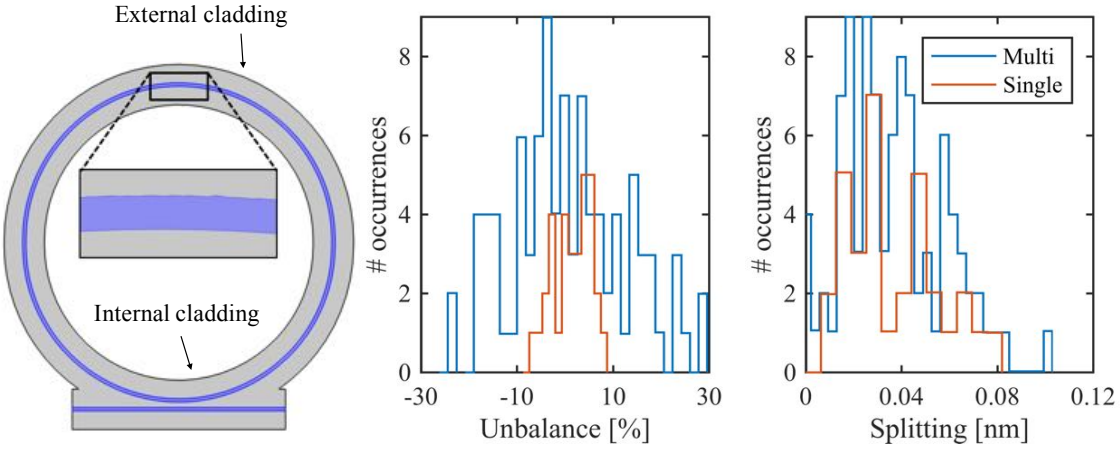

Figure 5.4: (left) Structure of the simulated resonator-waveguide system; blue colour indicates higher refractive index materials (n=2), while grey colour represents the internal and external cladding material (n=1.45); (center) unbalance, calculated from difference between transmittance minima (see method U_1 in Section 5.5), and (left) splitting occurrences as obtained for a singlemode (blue line) and a multimode (dashed red line) resonator; the difference between the two resonators is clear in the unbalance, whereas no net difference is observed in the resonance splitting.

multimodal nature of a resonator. In order to confirm this hypothesis, some FEM simulations were carried out with the COMSOL® software.

The investigation aims at verifying the differences between singlemode and multimode resonators in the appearance of resonance doublets. 2D simulations of an in-plane coupled resonator (Figure 5.4(left)) allow the transmittance to be computed at different wavelengths and to visualize the resonance minima of each doublet. Resonator radius and materials similar to those of the real structure investigated in Section 5.4 are used, and the rough sidewalls responsible for the backscattering are reproduced with a perturbation on the external circumference of the resonator (inset of Figure 5.4(left)). More in detail, sidewall roughness can originate from several fabrication steps (the lithographic process, the wet chemistry steps or common dry etching [47, 115]) and the appearance of scatterers along the resonator sidewall is basically a stochastic process. Therefore, the surface roughness can be truthfully reproduced by a Gaussian distributed noise along the resonator external edge. The RMS (ξ_{RMS}) and central wavelength (ξ_C) characterizing this distribution are chosen to match the real Q factor of the device and accounts for 0.008 and 100nm, respectively. Moreover, only a portion (1/3) of the resonator edge opposed to the coupling region is covered with the noise distribution. This is done to avoid the appearing of a roughness dependent coupling[4], which is not the subject of the study. Results of the simulations are synthesized in the two panels of Figure 5.4(center and right). In particular, the doublet unbalancing and splitting of a singlemode and of a multimode

[4]An example being the unwanted enhancement of backcoupling effects along the coupling region.

resonator are shown. The unbalance values are obtained from the difference between transmittance minima of the doublet, as explained in Section 5.5, while splitting is calculated as the spectral distance between doublet minima. Due to the stochastic nature of the process, only a statistic approach can reveal the properties of the devices. Several doublets are then considered and an histogram for each quantity is obtained.

As it can be seen from the data, a clear increment in the overall unbalancing is associated to the onset of multimode operation for the resonator (blue histogram), while very feeble asymmetry is found when singlemode resonators are considered (red histogram). This explains the symmetric modes that are observed in high-Q singlemode resonators [106, 116, 117]: when the multimode channel is not open, there is a higher probability for a backscattered photon to couple with the single opposite propagating mode; conversely, with a multimode resonator a non-null probability exists to couple a backscattered photon to a higher order mode, which does not contribute to the amplitude of the standing waves. Interestingly, a similar difference is not found in the doublet splitting, which reaches similar values in the singlemode and multimode resonators. Therefore, equal behaviour for the reactive component of single and multimode resonators seem not to be followed by equal behaviour of the dissipative component, thus suggesting that the multimode resonator can enhance the presence of asymmetric doublets. This fact has relevant practical consequences since different approaches to the phenomenon of backscattering should be used. Indeed, on one hand, the singlemode condition is preferred for the predominant presence of symmetric doublets, a property which makes the device response more predictable and more easy to be controlled. On the other hand, the multiple channel operation provided by multimode resonators is a favourable property for their implementation in photonic circuits. Moreover, there exists a possibility to exploit the asymmetry of a doublet in the generation of entangled photons [118], or even to alternatively suppress one of the two resonances and create a two way photonic switch.

5.4 Experimental results

In order to take advantage of the above-mentioned features of asymmetric split resonances or even to cancel asymmetry out, a proper control of the cw/ccw power balance is needed. In this sense, the variation of azhimutal number that has been exploited in Section 4.3 to tune the mode coupling parameters is not a useful tool. Indeed, highly variable asymmetry has been observed in neighbouring doublets [102, 109], mainly due to the randomly distributed roughness. A more practical solution relies on the tuning of a single doublet. Recently, tuning of the asymmetry has been proven in the case of nonlinear interaction inside the resonator when strongly exciting the resonance doublet [119, 120], the basic principle being the unbalance of self-phase and cross-phase modulations. However, both experiments showed symmetric resonances in low power conditions and their investigation was aimed at a different goal; namely,

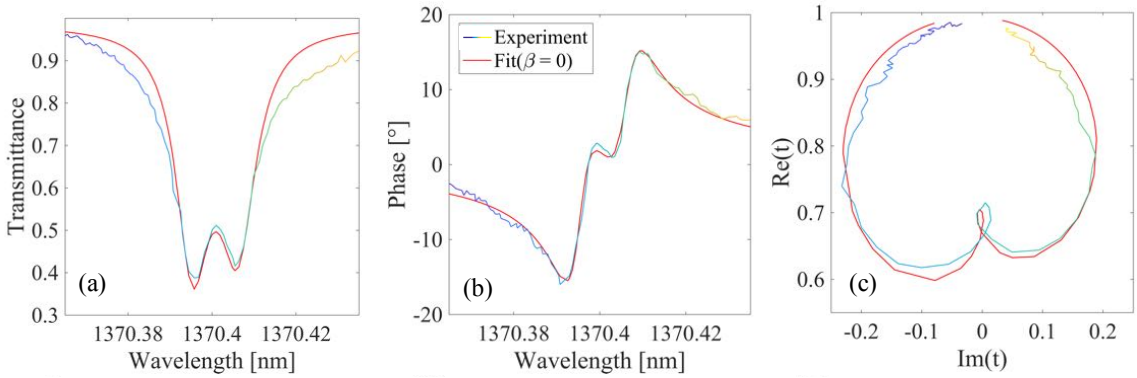

Figure 5.5: Transmittance, phase and phasor plot of the investigated doublet. It is useful to highlight the greater sensitivity offered by the phasor plot even in the central part of the doublet, where it more clearly evidences the small discrepancies between data and fit.

the symmetry breaking observed in pumped doublets.

In this section, an experimental investigation on doublet asymmetries is described. Asymmetric transmittance and phase doublets are observed under low power excitation. Moreover, all optical tuning of the asymmetry is demonstrated through Pump & Probe experiment, with transmittance unbalance reaching values up to -40% and 40%. The experiment also highlights different behaviours between imaginary (splitting) and real (dissipation) components of the coupling, and thus confirms the predictions of the simulations. It also provides a first validation of the theoretical model presented in Section 5.2 through accurate fitting of the experimental phase and transmittance data.

5.4.1 Pump and probe experiment

The analogy between multi mode coupling and ccw/cw described in Section 5.2 offers an interesting tool to prove the tuning of doublet asymmetry. Indeed, in a recent work by Bernard et al. [93], the reactive coupling between copropagating modes in a vertically coupled device is tuned by means of a pump laser, which basically serves as a heating source for the device. The observed variation of the coupling parameters suggests to exploit the same tool to investigate the tuning of coupling parameters in a backscattering doublet. Therefore, a pump and probe experiment is carried out on the wedge microresonator already studied in Chapter 3. The choice of a vertical geometry allows to truthfully discard the presence of backcoupling effects at the coupling region, as already pointed out in Section 5.2. Moreover, the use of a wedge resonator decreases the intrinsic losses with respect to a similar disk resonator [12] and allows backscattering doublets to be observed. Indeed, despite this structure does not show doublets in the C-band (1530-1565nm), the larger transparency of the resonator material (SiN) in the E-band (1360-1460nm) allows doublets resonances to be observed in this spectral region. In particular, in Figure 5.5, the transmittance

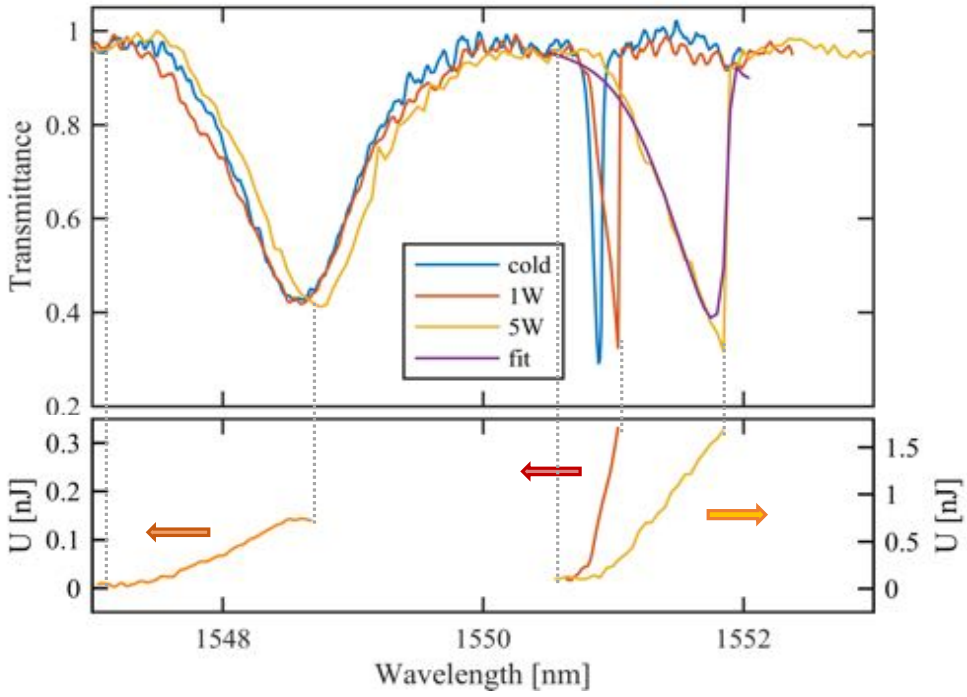

Figure 5.6: (top) Spectrum of the tested device in three power excitation regimes and (bottom) stored energy for the two observed resonances in high power conditions.

and phase spectra of the investigated resonance at 1371 nm are shown and two split resonances are clearly visible. Fit of the experimental data with the theoretical model returns values for the dissipative (β_i) and reactive (β_r) components of the mutual coupling of about 1GHz and 30MHz, respectively. The low but not null real component is justified by the weak asymmetry, while the large imaginary part confirms the large splitting observed in transmittance. The evidence of doublet splitting appears also in the phasor plot as a small circle right in the center of the phasor curve.

Exploiting the setup described in Chapter 2, it is possible to study both the transmittance and the phase of the doublet with a probe laser, while exciting another resonance in a different spectral region. The pumped resonance is chosen in the C-band region to allow an easier optical filtering of the pump signal from the probe one. The selective excitation offered by the vertical coupling allows two different resonator modes to be effectively excited in that region: the 1^{st} radial mode corresponding to a narrow resonance ($Q \sim 20000$) and the 2^{nd} radial mode associated to a broader one ($Q \sim 1000$). The spectrum of the device, showing these two resonances in low and high power excitation, is plotted in Figure 5.6, together with the stored power inside the resonator, obtained from Equation 1.16. The typical triangular transmittance due to thermo-optic effect is observed for the 1^{st} mode when pumped at 5W and, less intense, at 1W. A similar resonance alteration is not found for the 2^{nd} mode at the same excitation powers, because the lower mode confinement produces lower values of stored energy; in addition, the larger resonance width makes a possible alteration of

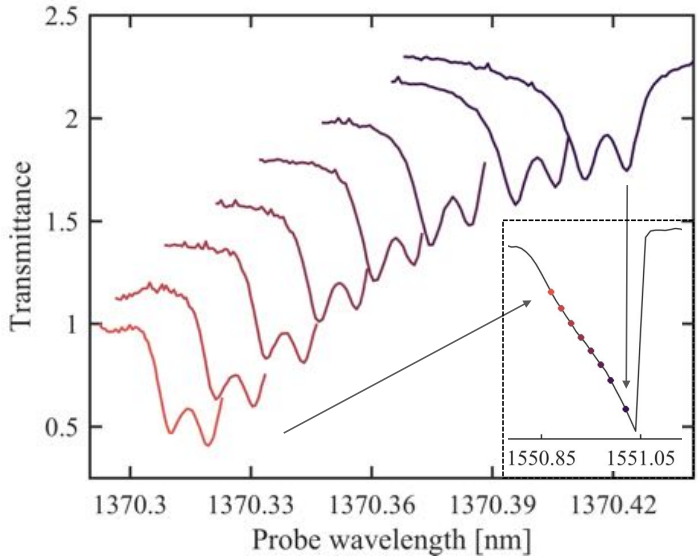

Figure 5.7: Transmittance spectra of the probe doublet acquired at increasing pump wavelength (transmittance is vertically offset and the right part of the resonances is not shown for a more clear visualization); in the inset, the recorded pump spectrum is shown, with different dots indicating the pump position for each acquired probe spectra; a clear shift of the doublet central wavelength is observed as the pump moves towards the resonance center; data are obtained with the pump laser exciting the 1^{st} radial mode and with an input power of 1W; variation of the doublet unbalance is also visible in the figure.

its shape less visible. A fit of the triangularly shaped resonance at 5W with Equation 6.6 presented in Chapter 6 is also shown in figure.

The thermo optic effect combined with the high input power allows a fine tuning of the doublet wavelength to be achieved. Indeed, the sudden increase of energy that occurs when the pump wavelength approaches the resonance produces a corresponding increase in the resonator temperature due to power absorption from the material. Thanks to the thermo-optic effect, this temperature increment is translated into an increase of the effective index of any resonance of the device (a more detailed explanation and a quantitative analysis of this phenomenon is contained in Chapter 6). Hence, a scan of the resonance at 1550nm produces a red shift of the doublet at 1370nm. This is observed in Figure 5.7, where the probe spectrum acquired for different pump positions is shown. As the pump moves towards the resonance center a larger shift of the probe is found, with values as high as 100pm when the pump reaches the resonance center.

The fine tuning of the doublet position offered by this method allows a value for the doublet unbalance (U_1) to be obtained at different wavelengths: with fixed pump power, the resonator internal power is tuned by scan of the C-band resonance and the consequent variation of the doublet spectral position and unbalance is monitored with the probe laser. A first sign of a wavelength dependent unbalance is already present in Figure 5.7: as the doublet moves to larger wavelengths, an evident variation in the

doublet asymmetry occurs. In order to perform a wider investigation on this property, this measurement has been carried out for different pump powers and radial modes. In particular, the results for three pump mode-power combinations (1^{st}-1W, 1^{st}-5W, 2^{nd}-5W) are synthesized in Figure 5.8, where the doublet unbalance vs doublet central wavelength is plotted[5]. An additional set of data, called *off-resonance*, is present and it serves as a reference level for the evaluation of thermal effects due to the strong laser power. In this case, the laser wavelength is kept fixed at an out of resonance condition throughout all the measurement, while its power is smoothly increased up to 5W. In this way only the distributed thermal effects occurring outside the resonator are considered, such as the temperature variation occurring to the whole sample due to facet absorption and waveguide absorption. The out of resonance condition assures that resonator based effects coming from the resonator excitation are not observed. A first comment on Figure 5.8 regards the comparison between these *off-resonance* data and the 2^{nd}-5W ones. The good overlap between the two set of data suggests that no additional effects are given by the resonator to the doublet unbalance when the 2^{nd} mode is excited. More precisely, the possible effects related to resonance excitation seems to be overwhelmed by the distributed thermal effects produced by the strong 5W pump. This fact is confirmed by the 1^{st}-5W set of data, which shows some points in accordance with the "off-resonance" and 2^{nd}-5W ones. These points corresponds to a largely detuned pump wavelength, still far from the resonance center, which basically corresponds to the *off-resonance* case; therefore, in this case the distributed thermal effects can be truthfully considered as the most prominent source of shift and unbalance variation for the doublet central wavelength. As it is expected, this effect ceases to play a significant role when the resonator begins to be effectively excited. Other doublets belonging to the 1^{st}-5W set are found at longer wavelengths due to the larger power circulating inside the resonator. These points exhibit an oscillating behaviour in their unbalance, as it can be seen from the central panel of the figure, where the unbalance over a larger spectral range is shown. Unfortunately, mode hops in the probe laser forbid measurements in the middle excitation range. Nonetheless, in the observed points the unbalance reaches values as high (low) as 40% (-40%). A similar oscillating behaviour is observed also for the 1^{st}-1W set. In this case, the unbalance immediately moves away from the other data set, indicating a small influence of the distributed thermal effect. This is because the pump power is 5 times lower than the 2^{nd}-5W case and its thermal effect is rapidly canceled in favor of a resonator dependent effect.

From this analysis, two competing phenomena responsible for the unbalance variation can be highlighted: (1) a first effect related to a distributed homogeneous heating of the sample, produced by power absorption outside the resonator and (2) a second effect strictly related to the local heating obtained with the excitation of the 1^{st} resonator mode. The first effect shows a weaker dependence on wavelength, with

[5]The 2^{nd}-1W combination is not shown because of the negligible central wavelength variation that is observed.

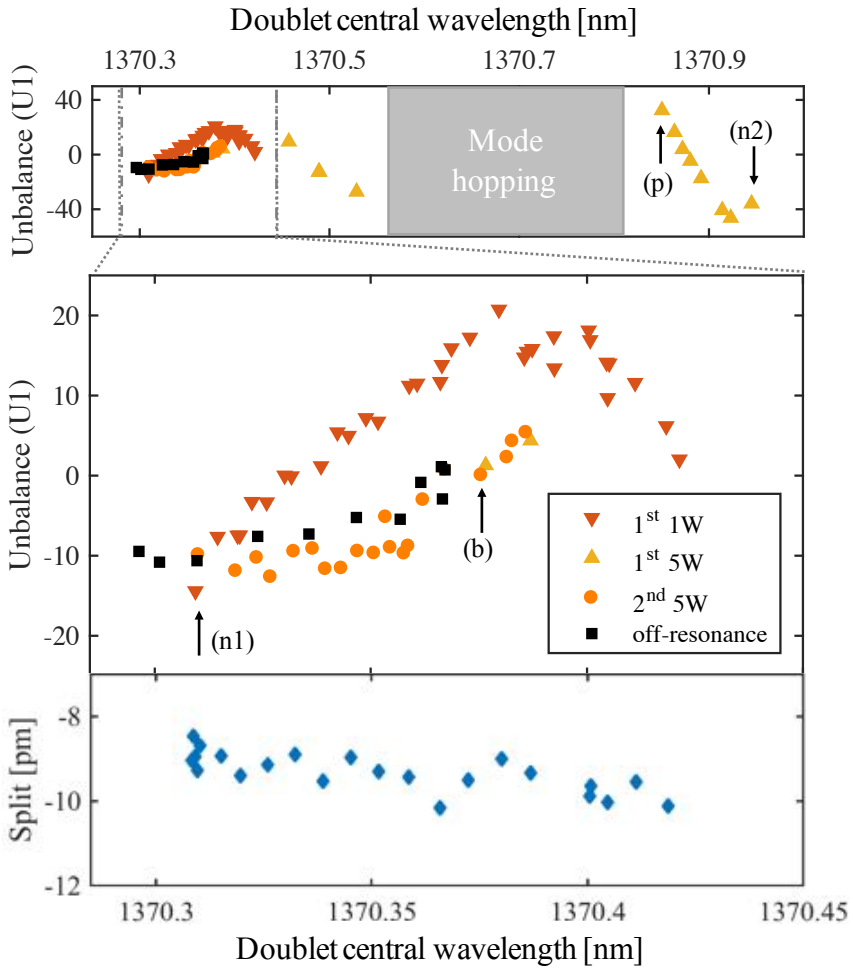

Figure 5.8: (top) Wide range plot showing the doublet unbalance for large shifts of the doublet central wavelength and for different pump mode-power combinations; the four different scenario presented in the text are highlighted with different marker shapes and colours; the unbalance is obtained from transmittance difference method U_1 (see Section 5.5). (center) Zoomed view of the same data (bottom) Doublet split for the 1^{st}-1W combination. Arrows refer to the data shown in Figure 5.10.

an average unbalance variation of about 15% over a 70pm shift. Moreover, it does not manifest any evident oscillation, but simply a smooth increase. The second effect produces a stronger unbalance variation of about 30% over the same spectral shift. Most importantly, it produces an oscillation in the doublet asymmetry, which makes possible to switch from a -40% to a 40% unbalance in a 100pm shift of the resonance wavelength. The oscillation is continued over all the spectral shift obtained with the 5W pump power. Interestingly, the doublet split does not follow the oscillations of the asymmetry (see Figure 5.8(bottom)), similarly to what obtained by simulations.

In oder to understand the origin of the stronger effect (2) a second simulation, similar to the one presented in Section 5.3, is carried out. In this case the heating is strongly localized in the region of the first order mode. Therefore, only locally the refractive index is changing. To model this, only the refractive index of the inter-

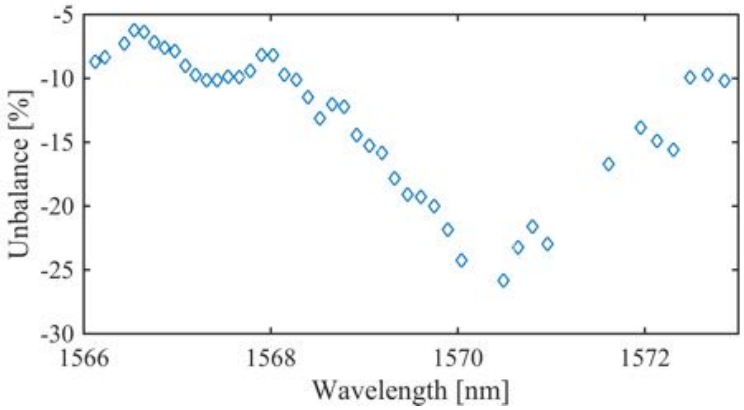

Figure 5.9: Unbalance dependence on doublet central wavelength as obtained from 2D simulation of a $20\mu m$ radius microresonator; simulation parameters are the same as those used to obtain Figure 5.4 (for the multimodal case), the only difference being the central wavelength of the noise distribution ξ_C, which is decreased from 100nm to 10nm; spectral shift of the doublet is due to the increase of internal cladding refractive index from 1.44 to 1.46, with step of 4×10^{-3}.

nal cladding is increased. Indeed, the wedge shaped resonator pushes the mode to propagate in a more internal radius at increasing wavelengths (see Figure 3.8). Consequently, the local temperature increase produced by pump absorption is displaced from the probe profile to a more inner radius. Therefore, the probe field perceives an asymmetric increase of the refractive index, which can be simulated with a higher refractive index of the inner cladding. Results of the simulation (see Figure 5.9) qualitatively follows what is experimentally observed. An overall oscillating unbalance with wavelength appears, with maximum and minimum values reaching -5% and -25% respectively. The differences between simulation and data are mainly ascribed to the limitations of 2D model over a complex 3D real structure (wedge shape) and to not accurate roughness parameters.

Despite this qualitative agreement between experiment and simulation, a clear understanding of the physical origin for the oscillating unbalance is not yet reached. From a mathematical point of view, the only multimodal nature of the resonator that is introduced to explain the asymmetry is not sufficient to explain the observed dependence on wavelength. This can be described with an oscillation in the real component of the coupling, which means a variation in the energies stored in the symmetric and antisymmetric standing modes. A first tentative explanation relies on the relative position between these two modes with respect to the waveguide. As described in [121] a variation in the position of a defect results in different losses, and then unbalancing, for the two standing modes. In our case the defect could be the waveguide, which can introduce losses at the coupling region. Instead of a physical movement of the waveguide, a variation of the defect position can be reproduced by the wavelength increase. The field profiles of the standing modes at the coupling region depend periodically on wavelength and bring to wavelength dependent coupling

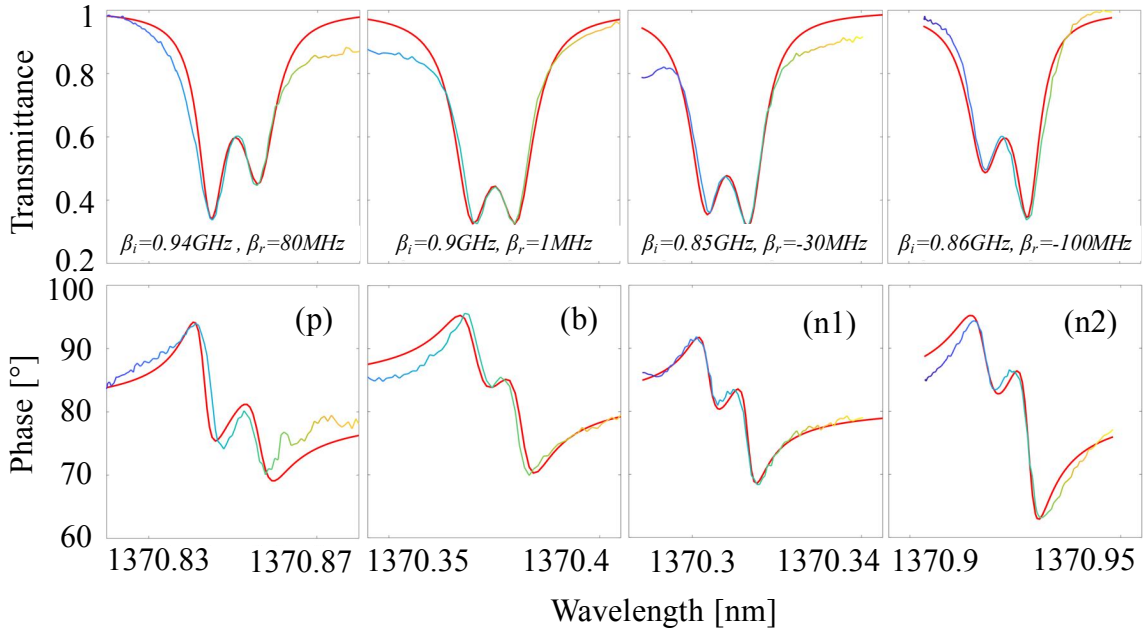

Figure 5.10: Experimental (coloured lines) and fitted (red lines) transmittance and phase of differently unbalanced doublets (positive (p), balanced (b) and negative (n1)-(n2); agreement between the two curves is observed, with discrepancies mainly due to Fabri-Perot oscillations, which becomes visible in out of resonance conditions.

induced losses, which could explain the unbalance oscillation. This interpretation can explain the weak unbalance variation observed for the thermal effect as the beginning of weak oscillations. The stronger variation observed for a 1^{st} mode pump is explained with a local asymmetric alteration of the refractive index, which brings to a spectral shift similar to the case of an homogeneous increase, but with an enhanced difference in the coupling induced losses.

As a last analysis, the different symmetric and asymmetric doublets observed during the pump and probe experiment can be used to test the theoretical model. In Figure 5.10 transmittance and phase spectra for different doublets are shown, together with theoretical fitted curves. The spectra are related to the unbalance points addressed by arrows in Figure 5.8 and they have been chosen to cover different possible asymmetry configurations. Fitting parameters for the doublets are shown in the figure. As expected, the real coupling coefficient assumes positive, negative and almost negligible values, thus following the three observed asymmetries. The imaginary component is found at about 90MHz, which results in a spectral distance between the two minima of about 11pm, in agreement with the experimental data shown in Figure 5.8(bottom). Despite good agreement between data and model is found for all the doublets, some divergences are observed, especially in the extreme parts of the spectra. These discrepancies are mainly ascribed to the Fabry-Perot oscillations, whose intensity becomes more visible when the transmittance flattens, i.e. outside resonance. Moreover, the initial assumption on the mode coupling parameter

$\beta_{12} = \beta_{21}$ should be carefully reconsidered since the wedge shape of the resonator can displace the symmetric and antisymmetric modes at different radial positions and create overall different losses and coupling strength.

5.5 Doublet visualization

5.5.1 Identification

As a last topic, a new method for the identification of a doublet and for the recognition of its asymmetry is proposed. Indeed, a doublet is usually distinguished by looking at resonance alteration in the transmittance spectrum [111]. In particular, a doublet becomes visible when the transmittance shows two different minima. In this case, even if the split does not overcome the FWHM of the single resonances, the doublet can be said to be resolved in transmittance. Actually, several cases can be found where a not resolved doublet affects the device properties [104]. Therefore, a method for the identification of doublets that are partially or completely hidden in their transmittance spectrum is a desirable goal. Figure 5.11 contains four different panels, associated to different identification methods. In each panel three curves related to three different coupling strengths (β_i) are shown to evidence the sensitivity of the methods to weakly backscattered modes. The first panel (top-left) presents the most common approach, which exploits the information on the system that is given by transmittance and looks for a bifurcation in the resonance dip. In addition, phase observation (bottom-left) can be joined to transmittance to give a two side observation of the system. However, as evidenced by the figure, these two separated quantities do not provide a sensible visualization tool in the case of weak coupling. In a second approach, the condensed phasor plot can be exploited (top-right). This method had already been theoretically proposed [101], but it becomes useful only when large coupling parameters are present. As it can be seen in the figure, the phasor barely changes its circular shape and it can be hardly used to univocally identify the presence of a doublet. Interestingly, a much sensible and efficient way to extract the split nature of a resonance is obtained when looking at the response inverse ($1/t$). Actually, the curve representing the real and imaginary components of the response inverse in a 2D plot ($x = Re(1/t)$ and $y = Im(1/t)$) is a common circle, which can be represented in an inverse phasor plot. Generally speaking, the complex inverse mapping ($t \rightarrow 1/t$) transforms circles (phasor plot) in circles (inverse phasor plot), where the only difference lays in their radii. In this way, no improvement in the sensitivity is obtained with respect to the common phasor plot. However, when the phasor circle is forced to pass through the origin of the axes ($Re(t) = 0$ and $Im(t) = 0$) its inverse mapping becomes a straight line. This is observed in the bottom-right panel of Figure 5.11, where the straight line (blue horizontal line) is the inverse phasor curve of non interacting resonator modes. When this requirement is fulfilled, the inverse representation is able to reveal backscattering doublets that were hidden in

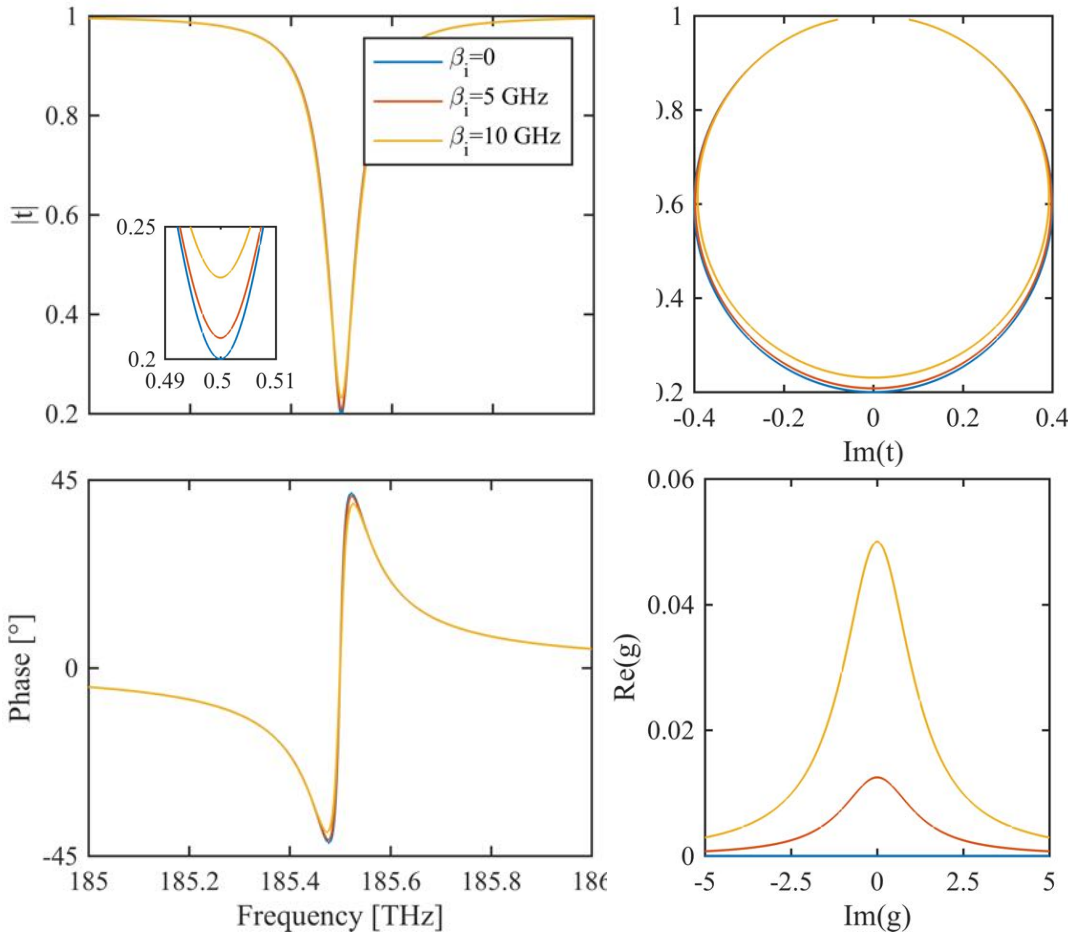

Figure 5.11: Different methods for the identification of a doublet: (left) transmittance (with zoomed transmittance minima in the inset) and phase spectra as obtained from Equation 5.13, (top-right) phasor plot and (bottom-right) inverse phasor plot; no doublet asymmetry is considered in the simulation to simplify the description ($\beta_r = 0$).

other methods: the red and yellow lines obtained for weakly interacting modes show an evident deviation from the blue straight curve for non interacting ones. This evidence demonstrates the high sensitivity reached with this new visualization method. Actually, in order to have a phasor curve always passing through the origin, a unity down shift of the real component is applied, and the plotted new quantity is not the response inverse but $g = 1/(1-t)$.

In order to illustrate the experimental relevance and the increased sensitivity offered by the new method, a study of a not resolved doublet is performed. The involved resonance is found nearby the one investigated in Section 5.4 and it does not show any relevant sign related to the presence of a doublet, nor in transmittance neither in phase response (see Figure 5.12). In this sense, fitting of the experimental curves with the model can help to evidence the presence of backscattering. The two fit curves are obtained considering a model with or without interaction (i.e with β_i

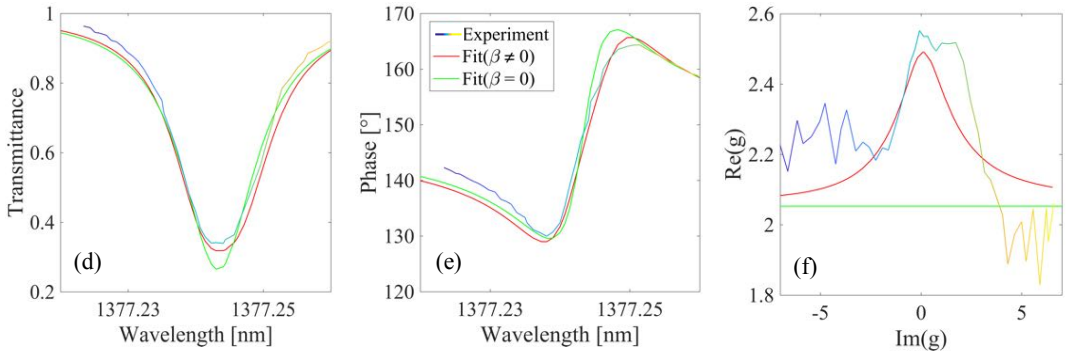

Figure 5.12: Experimental and fitted transmittance (left) and phase (center) of the microresonator investigated in Section 5.4 for a not visible doublet; lack of evident transmittance alteration prevents recognition of the doublet to be easily performed with the only experimental data; (right) inverse phasor plot obtained from the same curves showing clear alteration from the straight line associated to singlemode propagation.

as fitting parameter or with β_i fixed to 0; $\beta_r = 0$ in both cases). Despite they both are able to describe the main features of the experimental data, the relevance of the imaginary coupling coefficient obtained with the interacting fit ($\beta_i = 400MHz$) seems to indicate the presence of a backscattering interaction. However, a definitive and much clear confirmation to this hypothesis is obtained with the inverse phasor plot (see Figure 5.12(right)), which presents a clear bump in correspondence to the resonance center, where the doublet is expected to appear. Moreover, the qualitative good agreement with the interacting model and the clear discrepancy with the non interacting one definitively confirm the presence of a hidden doublet.

This example already shows the potentiality of the new identification method, which does not remain a theoretical proposal but becomes a fruitful tool also in testing real devices. The high sensitivity makes it a useful tool both for the analysis and the prevention of split resonances. Indeed, an inverse phasor analysis on a (thought) normal resonance can reveal the presence of a hidden mode coupling in the system. Therefore, successive investigations on the same device, for example the search for higher Q factors through increase of the radius, should take this effect into account. Remarkably, this analysis can be performed even before the coupling effect creates a visible alteration in the resonator spectrum. Nonetheless, the easier and more common transmittance and phase observations remain proper methods to get a sufficient insight on a system with large mode splitting.

5.5.2 Asymmetry

As the doublet can be recognized through different methods, its asymmetry (or unbalance) can be evaluated in different ways. We here present some possible choices, which are related to the identification method explained in the previous section. For example, when the common transmittance splitting is used, the most simple and

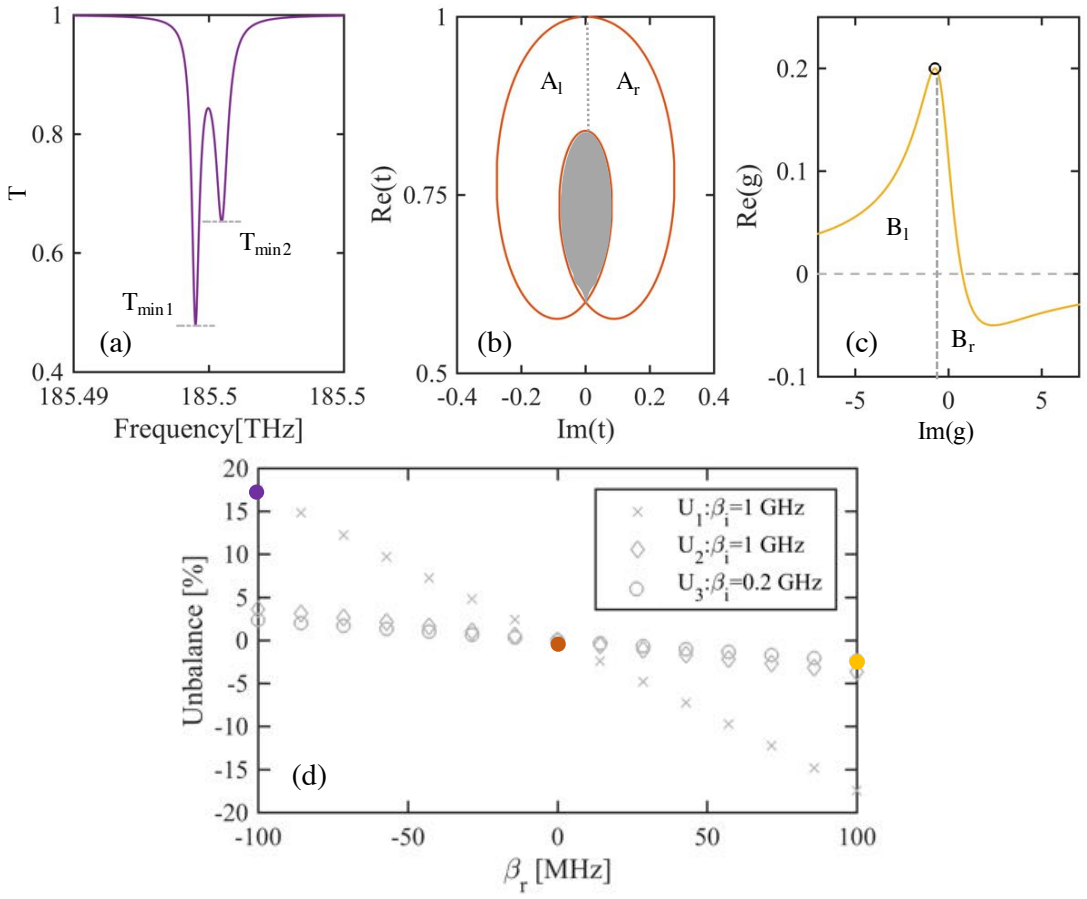

Figure 5.13: Unbalancing identification can rely on: (a) transmittance minima, (b) phasor area and (c) inverse phasor; (d) percentage unbalance found with the different methods for varying values of β_r; a direct comparison between different methods cannot be easily obtained due to the different values of β_i

effective experimental parameter is represented by the transmittance minima of the two coupled resonances, T_{min1} and T_{min2} , as described in Figure 5.13(a). The doublet unbalancing is then defined as the difference between these two values:

$$U_1 = T_{min1} - T_{min1} \tag{5.17}$$

An alternative approach can be followed when also the phase of the outcoming signal is measured. In this case the phasor plot of a doublet shows a flattened and perturbed circle, with one left and one right lobes (see 5.13(b)). When the transmittance shows a resolved doublet also a third central lobe is drawn by the phasor curve. In this description, the unbalance measurement is related to the area covered by the left and right lobes, whose mathematical description is:

$$A_r = \int_{-\infty}^{\varphi_c} |t|\cos(\varphi) + |t|\sin(\varphi)d\omega \qquad A_l = \int_{\varphi_c}^{+\infty} |t|\cos(\varphi) + |t|\sin(\varphi)d\varphi \tag{5.18}$$

where $\varphi = \varphi(\omega)$ is the phase response and $\varphi_c = \varphi(\omega_c)$, with ω_c the doublet central wavelength. The unbalancing is then defined as the difference between the two area normalized by the overall area:

$$U_2 = \frac{A_l - A_r}{A_l + A_r} \tag{5.19}$$

Despite these two are the most direct definitions of unbalance, there could be the case of unresolved resonances, where the identification of the doublet requires the inverse complex method described above. In this context, other definitions of unbalance are needed. In Figure 5.13(c) the inverse phasor is shown for the case of weak unbalancing ($\beta_r = 2MHz$, five times lower than for the curves shown in panel (a) and (b)). A first definition of unbalance relies on the integral of $Re(g)$ along the imaginary component $Im(g)$. In order to obtain an unbalance definition showing 0 value for a perfectly balanced doublet, the integral is computed in two different domains: (B_l) from $-\infty$ to the zero derivative point (black dot in figure), which corresponds to the central wavelength of the doublet, and (B_r) from the zero derivative point to $+\infty$. The unbalance value is then defined as:

$$U_3 = \frac{B_l - B_r}{B_l + B_r} \tag{5.20}$$

In Figure 5.13(d) the unbalance level computed with the three different methods is shown for different values of β_r. The simulation parameters are the same for U_1 and U_2, with a larger value of the imaginary component ($\beta_i = 100MHz$) with respect to the one used for U_3; this is needed to have a resolved doublet where the two methods can be applied. Remarkably, despite the five times lower splitting, the inverse phasor method returns unbalance values as large as the one observed with the phasor method, thus confirming its sensitivity. Actually, a real comparison of U_1, U_2 with U_3 definitions can not be done. The unbalance can be computed with the inverse phasor method only when not resolved doublets are present. For larger backscattering interaction, when a resolved doublet appears, the distorted shape of the inverse phasor curve brings to nonlinear dependence of the unbalance with β_r and prevents a suitable definition to be obtained. This fact manifests the complementary between different methods. Despite U_3 makes possible to highlight the presence of asymmetric doublets in extremely low backscattering conditions, it cannot be used for spectrally resolved doublets, where, however, U_1 and U_2 definitions can be fruitfully exploited.

5.6 Conclusion and perspectives

In this Chapter, a theoretical, simulative and experimental investigation on the backscattering phenomenon occurring inside a microresonator has been presented.

A theoretical model able to describe both symmetric and asymmetric doublets

has been proposed, with no restrictions on the resonator dimension and coupling scheme. The main characteristics of the model is the complex coefficient describing the coupling of *cw* and *ccw* modes, which indicates the presence of both reactive and dissipative effects of the coupling. The addition of a real (i.e. dissipative) component to the more common imaginary (i.e. reactive) one stems from the analogy with another system, namely, the multimodal coupling inside vertically coupled resonators, and it highlights an interesting connection between different phenomena. From a physical point of view the dissipative effect has been addressed to the multimodal nature of the resonator; this hypothesis has been confirmed with 2D simulations, which showed an increase of the doublet average asymmetry in the case of multimodal resonators. This fact represents an important results towards complete understanding and handling of the backscattering effect. Indeed, the number of modes supported by a resonator becomes an important design parameter, which should be considered to effectively obtain the desired effect (enhancement or reduction of asymmetry). Experimental validation of the proposed model has also been performed for the case of a vertically coupled resonator. Accurate fitting of transmittance and phase spectra for both symmetric and asymmetric doublets confirmed the ability of the model to correctly describe the system response. The peculiar properties of the tested samples (large radius wedge resonator and vertical coupling) allows to focus the investigation only on the internal backscattering source (i.e. sidewall roughness) and to neglect backcoupling effects at the coupling region. In this sense, a future study on the phenomenon should deal with both external and internal sources of coupling, trying to identify their relevance on the final response. The same experiment showed also tuning of the doublet asymmetry through spectral shift of the doublet central wavelength. Despite this interesting observation, which could be useful to control the generation of entangled photons or to create all optical switches, a clear understanding of its driving principles has not been achieved, yet. Future experiments should verify the presence of this effect in other samples. Moreover, investigation on a different coupling scheme, i.e. in-plane coupling, could help to distinguish the specific contribution of the waveguide-resonator coupling from the one of the resonator itself.

Finally, the enhanced visibility of a backscattering doublet provided by inverse phasor plot has been demonstrated both theoretically and experimentally; this new approach constitutes a remarkable tool for both the design and the fabrication of microresonators. Indeed, an early experimental identification of backscattering signatures permits a prompt correction of both design and fabrication parameters to be carried out, with consequent time and cost saving.

Chapter 6

Thermo optic effect induced bistability

An important quantity that must be taken into account when testing, designing and modeling photonic devices is temperature. Thermal effects in photonics have been widely studied, for the problems they can bring to the device operation, but also for the new processes they can enable [122]. Indeed, since the early observation of Thermo-Optic Effect (TOE) in Silicon, several Silicon-based devices have been produced to take advantage of this effect, from switches, to filters and modulators [123]. Specific attention must be paid to thermal effects in microresonators, where a correct thermal analysis becomes essential to fully control the device properties. Indeed, the sharp peaks associated to resonant modes increases the sensitivity of this device to temperature variations. This fact has both positive and negative consequences: on one hand, it opens to thermal control of the resonance position and thus, to microresonator-based switches and routers [124]; on the other hand, it increases the sensitivity to external temperature fluctuations and requires additional feedback control [125, 126]. Active control of a resonator temperature can be performed with a metal wire placed on top of the resonator: the wire heats up through Joule effect and heat conduction produces a temperature variation in the resonator volume. A different source of heat relies in the absorption of an optical signal inside the resonator: photons absorption by defects or by Two Photon Absorption (TPA) or Free Carrier Absorption (FCA) mechanisms constitutes a source of heat inside the resonator and thus increases its temperature. This effect is known as all-optic TOE and it is a nonlinear effect [127]. As it will be shown later in the Chapter, this nonlinearity makes the system a bistable one, showing different transmittance values for equal input signals and fixed parameters. The all-optical control of a bistable system through TOE can be exploited in the creation of all-optical memories and buffers [128] and it represents an important degree of freedom for the device. Therefore, a proper analysis on thermal effects in microresonators is a needed step towards optimization of temperature dependent functionalities. This is the aim of the present Chapter, which provides a brief analysis on the thermal effects occurring in SiN microresonators. The discus-

sion firstly introduces TOE: the origin and the proposed applications of this effect in microresonators are briefly presented in Section 6.1. All-optical TOE is described in Section 6.2, where the experimental realization of all-optic resonance tuning is also shown. The optical nonlinearity introduced by this mechanism is discussed in Section 6.3, where bistable operation of the resonator under optical TOE is demonstrated. The tested device is similar to those used in previous chapters of the thesis and the actual investigation can be used to highlight and discriminate thermal effects from other physical phenomena.

6.1 Thermo optic effect (TOE)

Modulation of the refractive index of a material can be achieved through different mechanisms: mechanical stress/strain [129, 130], heat [131], carrier injection [132] and nonlinear phenomena, such as TPA [133] or χ_3 (Kerr) [134], can alter the electronic distribution of a semiconductor and therefore modify its interaction with a propagating electromagnetic field inside the material. Among these, heating of a device is one of the most common techniques to control the optical properties of a device.

Indeed, when a material undergoes a temperature variation $\Delta T = T_1 - T_0$, a corresponding variation is found in the real part of its refractive index:

$$n(T_1) = n(T_0) + \left.\frac{dn}{dT}\right|_{T_0} \Delta T \tag{6.1}$$

where the term dn/dT is the thermo optic coefficient of the material.

Manifestation of this effect in the optical domain is commonly found in the spectral displacement of fringes and peaks of interferometers and resonators, respectively [1]. This is computed as:

$$\Delta\lambda_{TOE} = \lambda_1 - \lambda_0 = \left.\frac{d\lambda}{dT}\right|_{T_0} \Delta T = \left.\frac{d\lambda}{dn}\,\frac{dn}{dT}\right|_{T_0} \Delta T \tag{6.2}$$

where λ_0 and λ_1 are the peak/fringe wavelengths at T_0 and $T_1 = T_0 + \Delta T$. In the specific case of a microresonator, Equation 1.5 allows the above equation to be simplified to:

$$\Delta\lambda_{TOE} \sim \left.\frac{\lambda_0}{n_0}\,\frac{dn}{dT}\right|_{T_0} \Delta T \tag{6.3}$$

The above equation is an approximated one, because it takes into account only a variation of the refractive index of the resonator and not of the cladding. In Silicon-On-Insulator (SOI) microresonators, the ten times lower thermo optic coefficient of Silica with respect to Silicon [135] justifies the approximation. Conversely, the ob-

[1] Fabri-Perot fringes in waveguides are interferometric fringes and they are also affected by TOE.

served similar values for the thermo-optic coefficient of SiN and Silica makes the approximation less effective in the case of SiN resonators. Since here a SiN based resonator is studied, careful considerations must be done when evaluating quantitative experimental results for this structure.

Equation 6.3 can be used to obtain a first experimental estimate of the thermo optic coefficient of the device: the spectral displacement of a resonance is monitored at different temperatures. These are set by an external Peltier cell or metal wires integrated in the chip [136, 137]. The same equation suggests practical applications of microresonators as temperature sensors [138, 139, 140, 141]. In this last view, the Q-factor of the device plays an important role: a higher Q resonator enhances the sensitivity of the device to temperature variations due to a sharper linewidth. This fact represents also a drawback of high-Q resonators, because slight variations in the external temperature can strongly alter the response of the device. In this sense, microresonator based filters and routers, where accurate positioning of the resonance is required, are usually equipped with TOE-based temperature controllers, which are used to compensate fabrication errors or to cancel spectral displacements due to variations in the environment. TOE in microresonators is too slow to act as the main tuning mechanism: the slow heat dissipation occurring in micrometer sized structures limits the characteristic time of this effect to μs [142, 143], much longer than with other effects such as Two Photon Absorption (TPA) and Kerr effects, where ps switches are currently achieved [2] [145, 146, 147]. Actually, the different timescales between TOE and other nonlinear phenomena can be fruitfully exploited to achieve self-pulsing behaviour in microresonators and to create chaotic signals [148, 149]

Besides timing of the different processes, the impact of TOE on the device properties usually exceeds that of other nonlinear effects [150]. Therefore, a correct comprehension of its role is of crucial importance, both to take advantage or to reduce its intensity. For this last point, successful results have been obtained in slotted silicon microresonators applying a polymer (PMMA) with negative-thermo optic coefficient on top of the resonator [151]: the negative coefficient of the polymer allows to completely compensate the spectral shift produced by the resonator material with an opposite shift due to TOE occurring in the cladding. Other proposed solutions rely on careful control of the fabrication process: by thermal annealing of a Silicon photonic crystal cavity in N_2 atmosphere or by controlling the oxidation level in porous Silicon microcavities, null or strongly reduced TOE have been demonstrated [152, 153].

[2] Actually, a device exploiting fast thermo-optic effect with dissipation time about tens of ps and speed rate as high as 50Gbit/s has been theoretically proposed [144]; this exploits surface plasmon polaritons to shrink the field distribution to few nanometers and improve heat dissipation. This demonstrates that thermal effects are not intrinsically slow, but they are strongly limited by heat diffusion mechanisms.

6.2 Thermo optic effect: experiment

Despite the temperature control provided by external elements, there exists another way to tune the spectral position of resonances inside a resonating structure. Temperature variations can be achieved also by pumping a resonance with a strong laser source: the field enhancement produces a large optical power circulating in the resonator cavity and the linear absorption transform this power into heat, and then temperature gradient. This effect can be used to perform all-optical tuning of a resonance as it can be mathematically described with Equation 6.3:

$$\begin{aligned} \Delta\lambda_{TOE} &\sim \tfrac{\lambda_0}{n_0}\,\tfrac{dn}{dT}\big|_{T_0}\, R_{th} P_{abs} \\ &\sim \tfrac{\lambda_0}{n_0}\,\tfrac{dn}{dT}\big|_{T_0}\, R_{th}(1-T) P_{in} e^{-\alpha L} \end{aligned} \tag{6.4}$$

where the dependence of the temperature gradient ΔT on both the absorbed circulating power P_{abs} and on the thermal resistance of the resonator has been made explicit.

In the second line of Equation 6.4 a more practical description of the wavelength shift is provided, where an explicit form of the resonator absorbed power is given in terms of transmittance (T), laser input power (P_{in}) and absorption loss (αL). This last term mainly comes from impurities in the resonator material and it can be identified with overall intrinsic losses; indeed, other sources of loss like bending losses or surface scattering have negligible values due to the large radius and low index contrast of the resonator, respectively. From the Equation 6.4, it comes out that low transmittance and high intrinsic losses (i.e. low Q-factor) bring to larger resonance displacements. Therefore, to avoid TOE, undercoupled/overcoupled high-Q resonators with large thermal conductivity (low thermal resistance) should be used. In this sense, free-standing resonators, which shows higher resistance due to their insulation from the substrate, are more affected by TOE than their counterpart fixed to the substrate.

The all optical resonance tuning described by Equation 6.4 can be used in practical applications as an alternative tool to the temperature control, since it does not require design of external heating elements and it simplifies the fabrication process. Actually, the spectral displacement provided by the pump affects also the pump-resonance position, and thus modifies the power dropped in the resonator, with consequent alteration in the spectral displacement. Therefore, feedback control is needed to drive the circulating power to the needed value, which makes this method an alternative and not a substitute to the external one.

Experimental demonstration of TOE in a SiN microresonator can be obtained from high power transmittance measurements. The tested device is a microdisk wedge resonator similar to the ones investigated in Chapters 3 and 5. In Figure 6.1(top) the transmittance of an isolated resonance of the device is given for different input powers, while scanning the resonance from low to high wavelengths. A triangular shaped

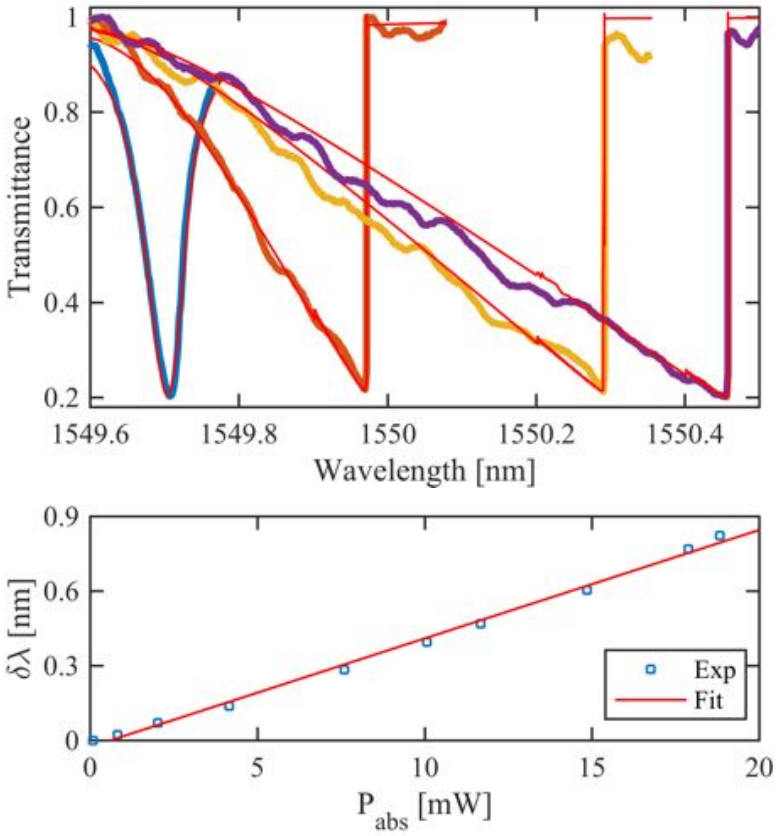

Figure 6.1: (top) Transmittance of a SiN wedge resonator for different pump powers: 0.8, 7.6, 14.8, 17.9 mW and (bottom) extinction ratio vs input power: experiment and linear fit.

curve is observed when the pump power is increased and it can be easily explained considering the TOE. Indeed, as the laser wavelength approaches the resonance, the dropped power in the resonator increases and consequently brings to a redshift of the resonance, as described by Equation 6.4. As the wavelength scan goes on this results in a slower decrease of the transmittance with respect to the low power spectrum. Once the laser reaches the blue shoulder of the resonance, the dropped power in the cavity starts to decrease (due to the increase of transmittance) and the TOE is no more able to sustain the redshifted position of the resonance, which abruptly steps back to its cold position and consequently brings transmittance to unity (being the laser far off resonance). The action of the TOE can be seen as a feedback on the resonance position: it is positive when a red detuned laser field is injected in the resonator and it brings to a lengthened red part of the resonance; it becomes negative for blue detunings, leading to a shortened (and almost not visible) blue shoulder.

Fit of the data (red curves in Figure 6.1) is obtained with a simple model which takes into account the nonlinear contribution provided by TOE. The resonating mode amplitude α is computed as:

$$\begin{aligned}\frac{d\alpha}{dt} &= \left[i\left(\omega_0 - \omega_{inc}\right) - \gamma_i - \Gamma^{rad}\right]\alpha + i\sqrt{2\Gamma^{rad}}E_{in} + \\ &+ iC\left|\alpha\right|^2\alpha\end{aligned} \tag{6.5}$$

The first line represents the usual equation for a single mode resonator (see Equation 4.1 or Equation 5.1 for comparison), whereas the second line contains the nonlinear contribution provided by TOE. A more detailed description on the origin of this nonlinearity is found below (Section 6.3). The coefficient C is chosen to be positive or negative depending on the sign of the thermo-optic coefficient. The laser drift is reproduced by a continuous change of the incident frequency: $\omega_{inc} = \omega_{inc}^0 - v_s t_s$, where v_s and t_s are the fixed scan speed and increasing scan time, respectively. Numerical solution of Equation 6.5 allows obtaining the device transmittance as:

$$T(\omega_{in}) = \left|1 + i\frac{\alpha(\omega_{in})2\Gamma^{rad}}{E_{in}}\right|^2 \tag{6.6}$$

It is important to notice that the described shape for the transmittance is found when materials with positive thermo optic coefficients are considered, as it is the case of SiN and Silica. Otherwise, the same reasoning works but with opposite scan direction: a triangular shape for the transmittance is observed when the laser scans the resonance from red to blue, and it reveals elongated and hidden blue and red resonance shoulders, respectively.

In Figure 6.1(bottom) the measured spectral displacement of the resonance center $\delta\lambda$ (corresponding to minimum transmittance in the data) for different resonator absorbed powers is shown, together with a linear fit of the data. Negligible or null contribution is observed from higher order terms. This is an expected result and it comes from the absence of TPA and, consequently, FCA related shifts due to the larger bandgap of SiN with respect to Si. On one hand, this fact simplifies the system and its analysis because fewer physical phenomena come into play. On the other hand, it prevents the observation of TPA based self-pulsing and chaotic behaviours.

From the slope of the linear fit a and from Equation 6.4, it is possible to extract the thermal resistance of the device as:

$$R_{th} = \frac{a}{\frac{\lambda_0}{n_0}\frac{dn}{dT}\Big|_{T_0}} \tag{6.7}$$

Inserting the thermo optic coefficient of SiN ($2.45 \times 10^{-5} K^{-1}$) as found from literature [122] and considering absorption loss as high as $\alpha = 0.9 cm^{-1}$[14], the resulting resistance at 1550nm is $R_{th} = (2 \pm 1) \times 10^3 [K/W]$. The large error associated to this experimental estimate comes from the limited precision in the evaluation of the input losses of the setup. As an example, an error of 1dB in the input losses (i.e. under/over estimation of coupling losses to the sample) brings to more than 25% of variation in the resulting thermal resistance. A reference value for the thermal resistance can be obtained through simulation of the system through Comsol software: in order to

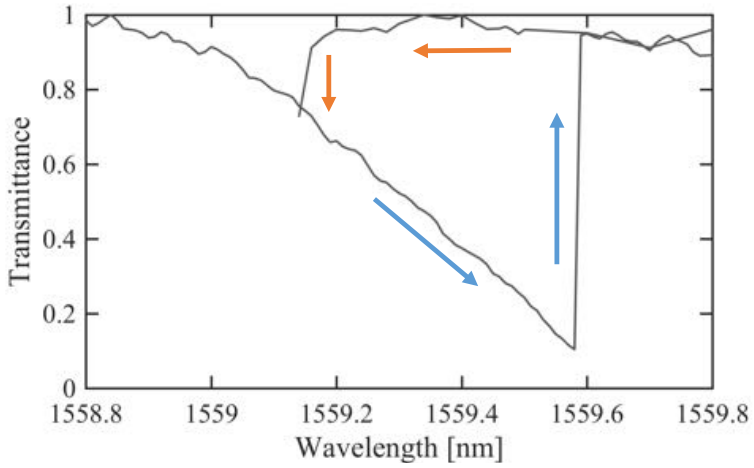

Figure 6.2: Resonator transmittance for two scanning directions (evidenced by arrows); bistable behaviour is highlighted by different values for the same input wavelength

correctly simulate the heat source, the profile of the propagating optical mode is used as the heat profile and the temperature variation of the resonator (weighted by the optical field profile) is evaluated for a given heat power. The resulting resistance is $R_{th} = 2.9 \times 10^3 [K/W]$, which agrees with the experimental one.

6.3 TOE induced bistability

The relation between the electric field E and the polarization P of a material is:

$$P = \varepsilon_0 \chi^{(1)} E + \varepsilon_0 \chi^{(2)} E^2 + \dots \tag{6.8}$$

where only the linear and quadratic susceptibilities $\chi^{(1)}$, $\chi^{(2)}$ have been considered. Being $\chi^{(1)} = n^2 - 1$, a variation in the refractive index $\Delta n = n_2 - n_1$ can be related to a variation in the linear susceptibility: $\Delta\chi \sim 2n_1\Delta n$.[3] Therefore, considering a variation in the refractive index produced by temperature, as described by Equation 6.1, the consequent polarization difference reads:

$$\Delta P = \varepsilon_0 \left(2n_1 \frac{dn}{dT} \Delta T \right) E + \dots \tag{6.9}$$

From this equation it becomes evident that the only presence of TOE does not bring to a nonlinear behaviour of the material. However, when an all optic TOE effect is considered, the temperature variation depends on the electric field intensity ($\Delta T = R_{th} P_{abs}$) and the TOE becomes a nonlinear effect.

A first evidence of this nonlinearity is the deformed response shown in Figure 6.1, where a nonlinear term is needed to explain the observed curve. A second

[3] A small variation Δn is here considered, such that $n_2 + n_1 \sim 2n_1$.

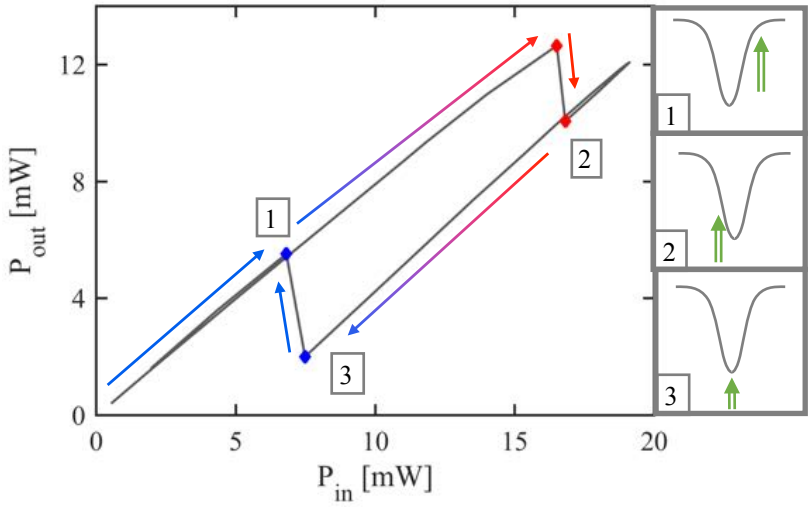

Figure 6.3: (left) Power output vs input at fixed blue detuned wavelength showing hysteresis and, hence, bistable behaviour; (right) schematic representation of the pump-resonance detuning

clue on the nonlinear nature of all optic TOE is presented in Figure 6.2, where the transmittance of a resonance is measured for two detuning directions of the input laser (from red to blue and vice versa). As it is found from the figure, the two curves clearly shows different behaviours, with the transmittance assuming two different values for the same incident wavelength. This comes from the TOE, which acts as a positive feedback while scanning the resonance from blue to red, and becomes a negative one when the opposite scan direction is chosen [154].

This result suggests a bistable behaviour of the system and requires a nonlinear phenomenon to be present (TOE in our case).

This statement is confirmed by another experiment, reported in Figure 6.3. The power at the waveguide output is acquired for increasing and decreasing values of the input power and for a fixed red detuned laser wavelength. As it is evident from the figure a bistable behaviour is observed. Explanation of this effect relies on the TOE and can be easily obtained following the panels on the right side of the figure, which represent the pump laser position with respect to the resonance:

1. At low powers the red detuned off-resonance laser pump results in a cold cavity and in almost unitary value for the transmittance; when the laser power is increased, a linear behaviour between input and output power is found, due to an almost constant transmittance level;

2. At a given threshold input power (highlighted by red dots) the TOE, activated by the circulating power, starts to move the resonance towards red; the consequent reduction of transmittance (the laser is getting more on-resonance) brings to larger circulating power and, then, to larger thermal shift of the resonance; the dynamics becomes a feedback dynamics, which rapidly moves the resonance

towards red and makes the laser passes from almost red off-resonance position (1) to blue detuned one (2), with an abrupt decrease in output power;

3. Once the input power starts to decrease, no abrupt variation is found at position (2) and the input vs output relation remains linear up to a lower input power (position 3); this is the result of a positive feedback provided by the TOE; indeed, as far as the power is decreased, a weaker TOE occurs and the center of the resonance moves towards the laser wavelength; however, this movement increases the dropped power in the cavity (the laser is going more and more on-resonance), and hinders the blue movement caused by lower input power; the effect holds until the resonance center finally reaches the laser wavelength (position 3); at this point the positive feedback becomes negative (as it happens for laser wavelength scans) and the resonance quickly moves back to its initial cold position (1).

The above described dynamics needs a red detuned pump laser and a positive thermo-optic coefficient, which basically moves the resonance on the red with input power. The same experiment performed with a blue detuned laser pump results in what is called an optical limiting behaviour, with the resonance moving off the laser pump as the power is increased, thus returning a limited cavity dropped power and an almost unity transmittance.

The bistable behaviour of the system can be investigated also by looking at the resonator stored energy U_i, which is experimentally obtained from Equation 1.16 (here reported for ease of visualization):

$$U_i = (1 - T)\frac{P_{in}}{\gamma_i} \tag{6.10}$$

U_i obtained from the data shown in Figure 6.3 is shown in Figure 6.4(a), where the four interesting points are highlighted by blue and red dots. As it is expected, low output power values correspond to high values for the stored energy.

Inserting the spectral shift provided by TOE into the equation for the resonator internal energy, an interesting insight on the nonlinearity provided by all optics TOE can be reached. From the usual transmittance equation the internal energy reads [49]:

$$U_i = \frac{2\Gamma^{rad} P_{in}}{(\omega_0 - \Delta\omega_{TOE} - \omega_p)^2 + (\gamma_i + \Gamma)^2} \tag{6.11}$$

The frequency shift $\Delta\omega_{TOE}$ due to TOE can be computed from Equation 6.4 and it becomes:

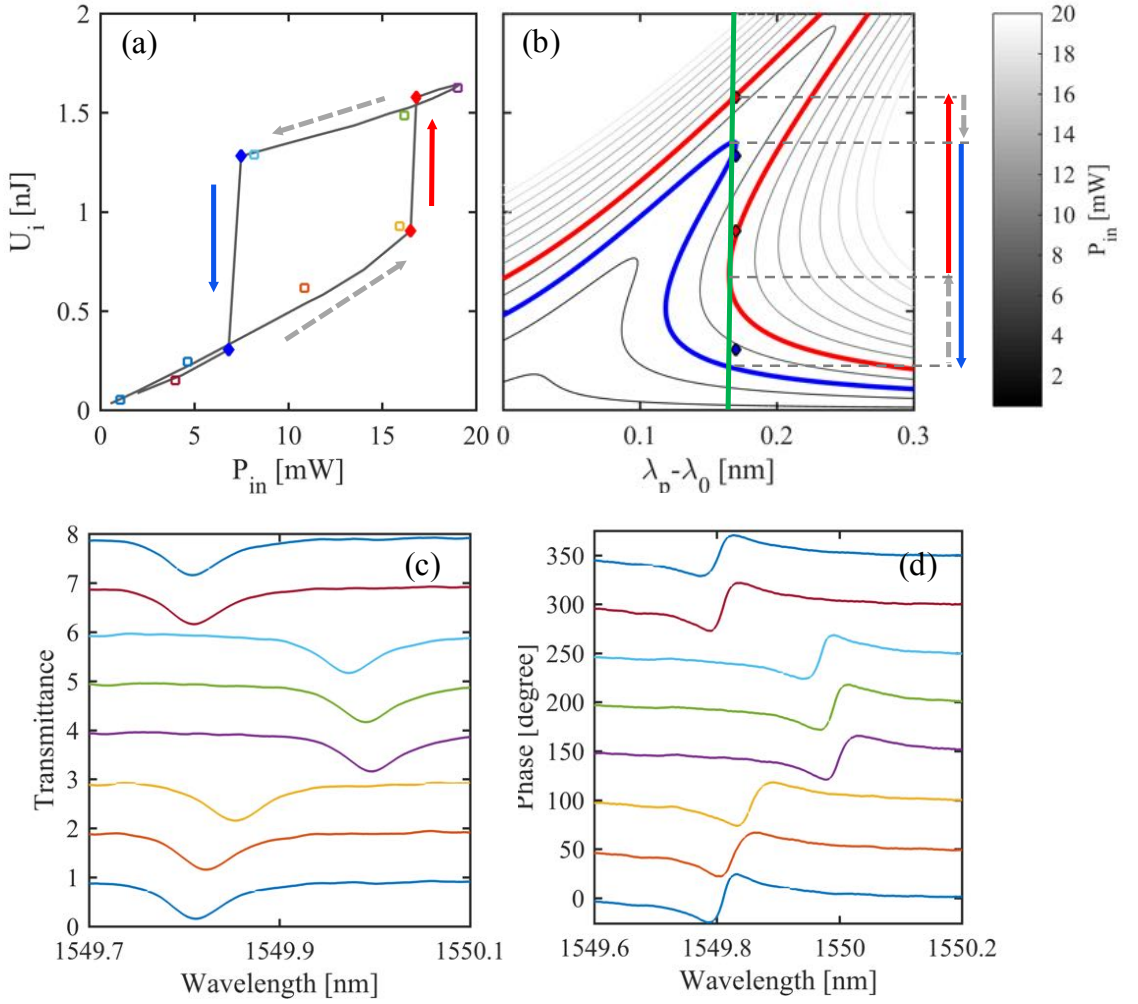

Figure 6.4: (a) Resonator stored energy U_i as obtained from experimental data presented in Figure 6.3 through Equation 1.16; coloured squares refer to the probe spectra shown in panel (c) and (d); (b) contour plot of the input power as a function of pump-resonance detuning and resonator stored energy; grey curves highlights equal input power points and clearly show the deformation produced by the nonlinear TOE; in the same panel the experimental points extracted from panel (a) are reported and the used laser wavelength is evidenced by the green line; good agreement between the data and the theoretical curves is observed; (c) transmittance and (d) phase of a probe resonance at different input powers (reported in panel (a)) showing two clearly distinguished states of the system, thus confirming its bistable behaviour; for ease of visualization, subsequent transmittance and phase spectra have been upshifted by unity and 50 degrees, respectively.

$$\begin{aligned}\Delta\omega_{TOE} &= \tfrac{\omega^2}{c}\Delta\lambda_{TOE} \\ &= \omega\tfrac{1}{n_0}\left.\tfrac{dn}{dT}\right|_{T_0} R_{th}P_{abs} \\ &= \omega\tfrac{1}{n_0}\left.\tfrac{dn}{dT}\right|_{T_0} R_{th}e^{-\alpha L}\gamma_i U_i \\ &= \omega\chi U_i\end{aligned} \tag{6.12}$$

The addition of a energy dependent shift produces a nonlinear behaviour of the resonator. This is clearly visible in panel (b) of Figure 6.4, where the dependence of the input power P_{in} over internal energy U_i and pump-resonance detuning is represented in a contour plot, as obtained inverting Equation 6.11. Curves belonging to fixed input powers are highlighted in grey scale and they basically represent the resonator internal energy at varying pump wavelength. Interestingly, the positive nonlinear coefficient χ bends the resonance towards red and creates a bistable region, where the system with fixed wavelength and input power can be loaded with two internal energies. This is more easily revealed by blue and red curves, which belongs to two input powers.

Blue, red and grey-dashed arrows on the right part of the panel schematically describes the internal energy steps that characterize the measurement shown in panel (a), with a fixed frequency detuning represented by the green line in panel (b): starting from the lower dashed line, the input power is increased and the system continuously increases its internal energy going from the blue to the red curve; the threshold point is found on the knee of the red curve, when the system jumps between two points with equal input energy but with remarkably different internal energies (red arrow); the successive decrease of input power shows a smooth decrease of the internal energy, following the grey-dashed curve up to a second threshold point, represented by the intersection with the blue curve; in this configuration another jump is made possible, from the maximum internal energy to a much lower value (blue arrow), which brings the system back to its initial condition. Experimental values shown in panel (a) are reported in panel (b) as blue and red dots and they qualitatively follows what is predicted by the theoretical curves.

The bistable nature of the system is proven also by the transmittance and phase of a probe resonance. While scanning the input pump power on the 1559nm resonance to obtain the data in panel (a), several spectra of a nearby resonance (at 1549nm) are acquired with the setup described in Chapter 2. Measurements shown in panels (c) and (d) of Figure 6.4 are related to the coloured points in panel (a). A clear relation is found between spectral shift of the probe and internal energy of the resonator. In particular, the redshifted probe spectra (3^{th} to 5^{th} lines from top to bottom) corresponds to large internal stored energy, where the thermal shift is more consistent.

In order to more deeply understand the properties of a bistable system the measurement presented in Figure 6.4(a) has been repeated for different pump-resonance

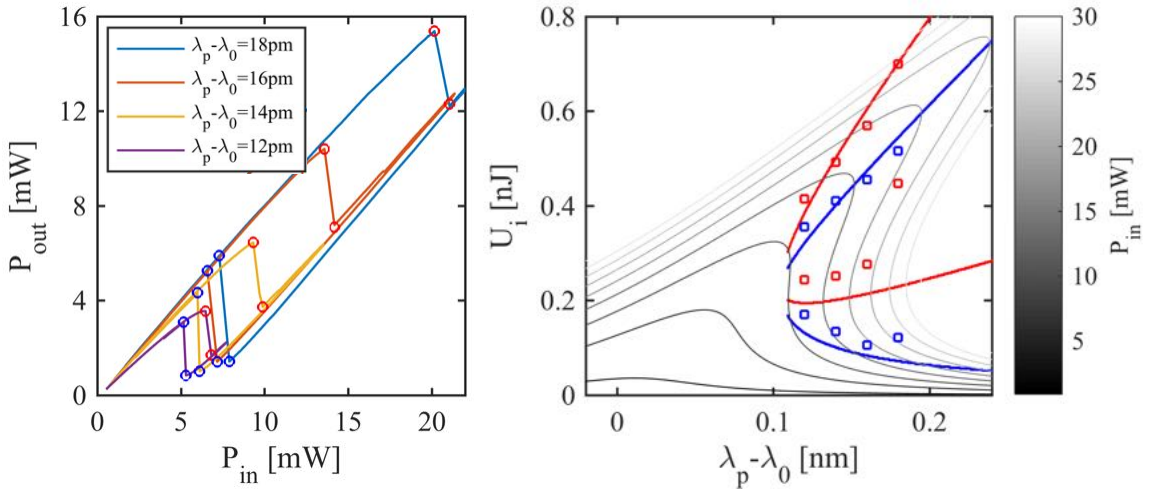

Figure 6.5: (left) Power output vs power input plot at different pump-resonance wavelength detunings; (right) Input power dependence on detuning and stored energy; blue and red lines/squares indicates simulated/experimental threshold values at different wavelength detunings.

(positive) detunings. Results of the measurement are shown in Figure 6.5. On the left, the output vs input power plot is shown: as the pump gets off resonance, larger input powers are needed to reproduce the hysteresis curve and a larger difference between high power and low power thresholds (red and blue dot, respectively) is found. In order to explain this experimental evidence, it is useful to look at the right panel of the figure, where a similar plot to the one presented in Figure 6.4(b) is shown. The blue and red curves represent the low and high threshold points for increasing input power. As it can be seen from the plot, when the detuning is increased the blue and red curves crosses always lighter curves, meaning that larger input powers are needed to reach threshold points. Theoretical curves shown in the figure are mainly driven by the nonlinear coefficient χ:

$$\chi = \frac{1}{n_0}\frac{dn}{dT}\bigg|_{T_0} e^{-\alpha L}\gamma_i R_{th} \tag{6.13}$$

which depends on several system parameters. Curves shown in Figure 6.4, are obtained with thermo-optic coefficient and propagation loss α taken from literature [122, 14], while the intrinsic loss γ_i comes from fitting of a cold resonance spectrum. Finally, the thermal resistance value comes from the FEM simulation ($R_{th} = 2.9 \times 10^3 [K/W]$). Remarkably, the experimental points in the figure related to threshold values (blue and red squares) extracted from the data shown in the left panel (blue and red circles) qualitatively resemble the system behaviour predicted by simulation. Quantitative discrepancies could be due to inexact evaluation of system loss or from slightly different sample parameters (i.e. thermo-optic effect or intrinsic losses).

6.4 Conclusion and perspectives

In this Chapter, the effect of optically driven TOE in SiN microresonators have been addressed. Linear absorption of photons inside the resonator has been identified as the main source of heating, with negligible contribution from higher order nonlinear phenomena. This result confirms the hypothesis made in Chapter 5, where the doublet shift observed in the Pump and Probe experiment was addressed to the linear absorption of Pump power inside the resonator. Description of the nonlinear phenomenon leading to a bistable behaviour of the system has been given and the dependence of bistability on wavelength has been investigated. Experimental data allows to obtain an estimate on the thermal resistance of the resonator which accounts for $R_{th} = (2 \pm 1) \times 10^3 [K/W]$. This value shows qualitative accordance with the simulated value ($R_{th} = 2.9 \times 10^3 [K/W]$) and it is about one order of magnitude lower than for a free-standing SiN resonator [155]. This last is an expected result: the free-standing resonator is more isolated from the substrate and the heat produced by the optical mode can only be dissipated through the thin pedestal[4]. To quantitatively confirm this fact, thermal simulation of a free-standing resonator isolated from the substrate by a $3\mu m$ Silica pedestal has been performed [5] and the found thermal resistance $R_{th} = 2.4 \times 10^4 [K/W]$ is about ten times larger than the one obtained for the in-plane resonator. The relevant uncertainty of the experimental estimate is mainly due to the limited precision on input/output losses estimation. In this sense, accurate measuring of the diverse source of losses and systematic monitoring of the device alignment stages must be considered for future investigations, especially when quantitative results are required. Finally, a simple measurement, which can help to clarify the analysis, is an experimental estimation of the thermo-optic coefficient of the device through TOE (i.e. with an external heating source). This can confirm or reassess the value found in literature.

[4] Dissipation through air is considered to be negligible.

[5] The same geometrical and material parameters described in [155] have been used.

Conclusions

The thesis mainly deals with a specific coupling technique for microresonators, that is, vertical coupling. The aim is to propose a comprehensive investigation of the several physical phenomena observed in vertically coupled microresonators to obtain a valuable tool for the exploitation of these structures in various applicative and fundamental researches.

In Chapter 3, the peculiar features connected to coupling of light to and from a single mode resonator have been discussed and a specific theoretical model has been proposed: remarkable difference is demonstrated between common in-plane coupling and vertical coupling, with the latter showing an oscillating coupling strength, both for wavelength and gap variations. Theoretical predictions have been validated with experiments on a vertically coupled SiN wedge resonator, both in the visible and in the IR domains. The possibility to critically couple both IR and visible modes suggests fruitful applications of vertically coupled resonators as multiple channel filters and the oscillatory dependence on waveguide position can be exploited in optomechanical systems involving free-standing resonators.

The selective excitation of different radial mode orders is another observed property of vertical coupling, which distinguishes it from other coupling techniques. This last feature allows more than one mode order to be simultaneously excited and provides an optimal platform to investigate the properties of intermode coupling in multimode resonators. These were discussed in Chapter 4, where the waveguide mediated coupling between the 1^{st} and 2^{nd} radial mode orders of a vertically coupled SiN resonator was studied, both theoretically and experimentally. The presence of reactive and dissipative components in the intermode coupling was demonstrated and their role in the appearance of asymmetric resonances was discussed. In particular, the reactive component is shown to strongly enhance or reduce the 1^{st} mode related resonance, depending on the relative detuning between the two modes, reaching also complete cancellation of the resonance. Thanks to the different FSR of the two families, experimental validation of the theoretical model for different detunings has been possible, confirming both resonance enhancement and suppression. The theoretical model already proposed in [13] to describe the intermode coupling dynamics has been here extended to the case of quasi-degenerate modes (i.e. modes with similar intrinsic/extrinsic losses and resonance position).

The similarity between the description of intermode coupling in multimode res-

onators and the one usually proposed for backscattered clockwise and counterclockwise modes suggests the presence of a dissipative term even in this last physical phenomenon, where only a reactive component is usually adopted. This possibility has been investigated in Chapter 5, where the subject of backscattering in microresonators has been treated. A general theoretical model for the description of asymmetric resonance doublets has been proposed: following the model described in Chapter 4, real (dissipative) and imaginary (reactive) components for the coupling of backscattered modes have been considered. The physical origin of these two components has been discussed and their effect on doublet shape has been highlighted. In particular, the real component was shown to describe unbalanced resonance doublets, without need of nonlinear interaction. Experiments to verify the model prediction were carried out on a vertically coupled SiN wedge resonator. Indeed, despite the model is valid for any coupling scheme, the peculiar waveguide position in vertically coupled systems allows to discard possible sources of backscattering at the coupling region and thus simplifies the analysis. Through pump and probe experiment, it was possible to tune the doublet spectral position and to observe doublets with different degrees of unbalance. Proper fitting of these doublets with the developed model returned non-null values for the real components, thus confirming the need of dissipative coupling between backscattered modes. Curiously, an oscillating dependence of the doublet unbalance on the doublet spectral position has been found. Despite simulations qualitatively reproduce the trend, the origin for this behaviour has not been identified yet. Some tentative explanations have been given. As a side topic, also the identification of symmetric and asymmetric resonance doublets has been considered: comparison of different identification methods provided a clear evidence on the additional sensitivity that is gained when phase measurements are combined with transmittance ones.

As a last topic, the behaviour of a SiN microresonator under high power excitation has been studied. The absence of χ_2 and χ_3 related nonlinearities simplifies the description of the system, which is mainly driven by TOE. Observation of transmittance spectra under different excitation powers provided an experimental estimate of the thermal resistance of the system, which agrees with the value simulated with FEM software. Bistable condition has been also observed and it can be explained in terms of nonlinear optical TOE. From this nonlinearity, a simple model describing the relation between input power and internal stored energy allowed to evidence the presence of a bistable region and to study its dependence on pump-resonance detuning. Input power vs output power plots acquired for different detunings qualitatively follow the prediction of the model and provided a second estimate for the thermal resistance compatible with the simulated one.

Chapter 2 deserves a separate mention. Indeed, no specific physical phenomena have been investigated in this chapter, but a comprehensive description of an interferometric setup has been given. The different components, the acquisition modes and the experimental characterization of the setup with waveguides and resonators have

been exposed. The same setup has been used to perform the phase and transmittance measurements that were shown throughout the thesis: in this sense the chapter deals more with a measurement method than with a device. Indeed, despite the main subject of the thesis is the vertically coupled resonator, a second subject can be recognized, that is, the phase measurement. Combined with transmittance, this quantity yields complete information on the investigated device, which helps to clarify known aspects or to highlight new features that are not apparent in the transmittance. In this sense, emblematic results are the definitive and unambiguous identification of the coupling regime in multimode resonators (Chapter 4) and the enhanced visibility obtained for unresolved resonance doublets through the inverse phasor method (Chapter 5). Actually, the advantages carried by phase measurements should not be restricted to resonating devices: phase measurements in a FWM process on a SiON waveguide are going to be performed to demonstrate the results described by Larrè et al. [156, 157] on a specific analogy between Bose-Einstein Condensates (BEC) and photon bunches conceived within the theory of fluids of light.

Clearly, some improvements are also possible in each of the investigated subject. A general advance in the measurements can be obtained with the introduction of a new delay line in the interferometric setup and with a more efficient isolation from temperature variations: these steps should reduce the noise and help to stabilize the system response. The results provided in Chapter 3 for transmittance values can be joined with phase measurements to confirm or reassess the proposed model. For what concerns Chapter 4, the new model for quasi-degenerate modes should be experimentally tested. Additional investigation is required also for the backscattering phenomena described in Chapter 5: the model must be confirmed with measurements on different resonators and different coupling schemes, taking into account also the backcoupling term that has been discarded in the present analysis. Moreover, accurate studies on the oscillating unbalance should be performed to identify the actual source for this behaviour. Finally, a more precise evaluation of the system losses is required to obtain accurate results, as demonstrated in Chapter 6.

In conclusion, the results described in this thesis represent an advancement towards a deeper comprehension and a more conscious exploitation of vertically coupled resonators. Theoretical modeling of fundamental physical phenomena in microresonators, such as intermode coupling and backscattering, has been experimentally validated on vertically coupled resonators. Despite the peculiaries of these structures, the generality of the proposed models makes them suitable also for different kind of coupling geometries. Finally, the additional information provided by phase measurement suggests to join it to common transmittance measurements when a different point of view on a given phenomenon is needed.

Appendix A

Dispersion model for delay line calibration

An explanation to the oscillating pattern of the interference in Figure 2.6(b) relies on two main contributes, a physical one and a mathematical one. From a physical point of view the different dispersions of the materials placed along the two arm of the interferometer (SiN and glass in our case) makes the phase difference between the two arms to change with wavelength. In order to study this phenomenon a simple model considers two propagating laser beams: $E_1 \propto e^{i\beta_1 L_1}$ and $E_2 \propto e^{i\beta_2 L_2}$ where the subscript 1,2 indicate the sample and the free arm respectively. β_i and L_i are the propagation constant and the path covered by light along the different materials composing the two arms, respectively (Figure A.1). Additionally, Fabry-Perot interference can be added by superimposing a second propagating beam with length 3L, 5L,... to the forward propagating electric field. Since the results presented in this work are barely influenced by Fabry-Perot fringes they have not been considered in the fitting model. Once the two beams have been propagated along all their individual arms, the intensity of the three detected beams can be found from: $I_0 = |E_1 + E_2|^2, I_1 = |E_1|^2, I_2 = |E_2|^2$. It is worth to notice that a good result for the interference signal cannot be obtained without considering the contribution of the

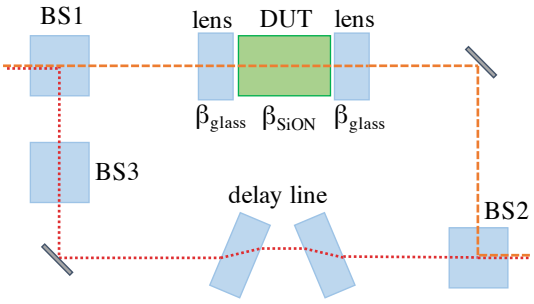

Figure A.1: Schematic representation of the setup with the elements considered in the model.

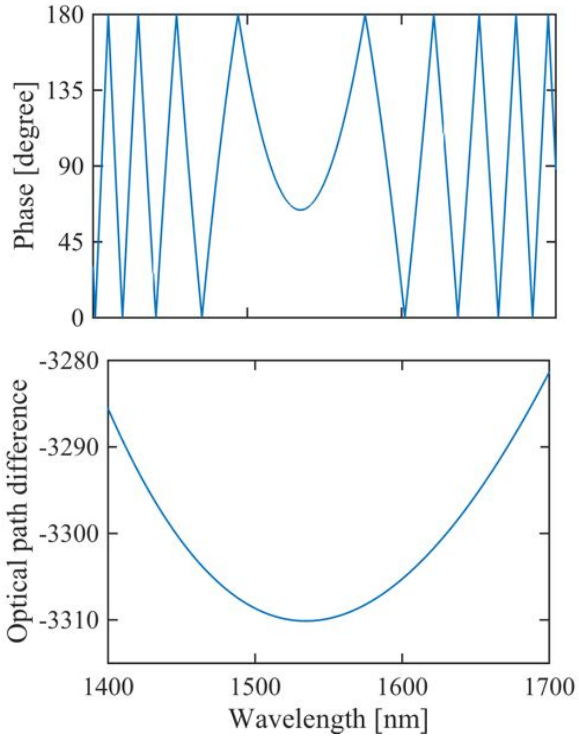

Figure A.2: Simulated phase and optical path differences using the described model for the scheme shown in Figure A.1

lenses in the two coupling objectives along the sample arm, which modify the optical path. Once the three signals are found, the phase response can be obtained from Equation 2.2. At this stage the mathematical issue becomes important: the presence of the $\cos^{-1}$ function in the equation requires to shrink the phase values between 0 and π to have a one-to-one correspondence. Therefore, a folded phase representation is obtained, as it can be seen in Figure A.2(top), where the phase is folded each time it reaches 0 and π values. The corresponding unfolded representation can be obtained with postprocessing of the phase signal and it resembles a parabola which opens upward. A more clear understanding of the phenomenon creating the phase oscillation can be reached by looking at the difference between the optical path along the free and the sample arms (Figure A.2(bottom)). Indeed, despite a large difference is observed throughout the spectrum the phase response shows a flat region at about 1520nm, where the optical path difference shows null slope. Moreover, the shape of the optical path difference resembles the phase response in its unfolded form: a larger slope of the first produces a larger slope of the second (i.e. faster oscillations in the folded representation). From this brief analysis, it becomes evident the main role of the delay line, which is not to compensate the phase delay between the two arms but their dispersions.

Appendix B

Quality factor analysis

A comparison of the 2^{nd} family resonances for the IR spectra in the two configurations can lead to a better understanding of the system. According to the transmittance values (see Figure 3.11), in the wg_2 configuration, the system should change from under- to over-coupling regimes as the wavelength increases, fulfilling a critical coupling condition at about 1530nm. Considering transmittance as the main information channel, wg_1 seems to follow the same behaviour, increasing its transmittance and thus becoming more and more overcoupled at higher wavelengths. Surprisingly, a similar analysis on the total Q returns different situation: the assumed overcoupled wg_1 configuration actually shows Q values always greater than those of wg_2, where the critical coupling condition is reached (see Figure B.1(top)).

Despite the two analysis (on transmittance and on Q) seems to reach opposite results, a solution to this apparent inconsistency is obtained by considering the total losses (Γ_{tot}) composed by two main channels, the intrinsic one (Γ_{int}), due to the material, and the radiative one (Γ_{rad}), mainly due to coupling:

$$\Gamma_{tot} = \Gamma_{int} + \Gamma_{rad} = \Gamma_{int}(1+k) \tag{B.1}$$

where $k = \frac{\Gamma_{rad}}{\Gamma_{int}}$ is the coupling coefficient. Then, the extinction ratio value can be written as:

$$ER = \left(\frac{\Gamma_{int} - \Gamma_{rad}}{\Gamma_{int} + \Gamma_{rad}}\right)^2 = \left(\frac{1-k}{1+k}\right)^2 \tag{B.2}$$

Experimental data of ER extracted from the IR spectra have been used in Equation B.2 to obtain the two possible k solutions of this second order equation for both the configurations wg_1 and wg_2. Knowing that $\Gamma_{tot} = \omega_0/Q_{tot}$, Γ_{int} and Γ_{rad} values could be extracted from Equation B.1. Since Equation B.1 and Equation B.2 are symmetric for Γ_{rad} and Γ_{int} they can be swapped in the calculations with no variation on the results. Therefore unexpected behaviour can be understood as follows. The intrinsic Q (Q_{int}) are the same for both wg_1 and wg_2 showing a particular strong dependence on wavelength (see Figure B.1). The similarity of the two values is an expected result since the two resonators belong to the same processed wafer. In contrast to the 1^{st} family modes, showing oscillatory coupling (main text), the low

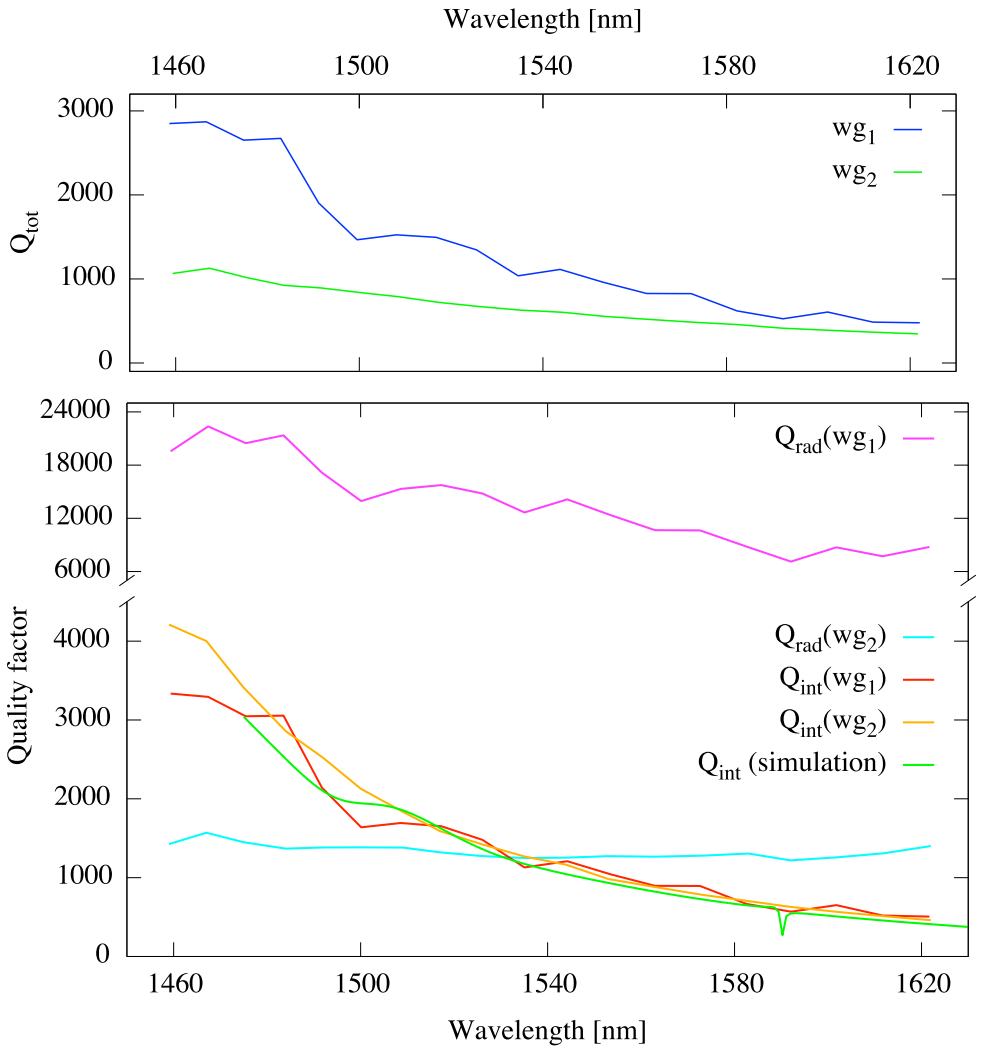

Figure B.1: (top) Quality factors from the IR spectra for wg_1 and wg_2; (bottom) Intrinsic and radiative quality factors for wg_1 and wg_2 configurations.

confinement of the 2^{nd} one induces a remarkable coupling to the Si substrate of the wafer through the SiO_2 bottom cladding limiting the Q_{int} with a strong wavelength dependency. This assumption has been confirmed by a FEM simulation which perfectly match the experimental values (green line in Figure B.1). As expected, much lower losses are found for the wg_1 configuration, which becomes mainly dependent on intrinsic losses ($Q_t \approx Q_i$). In the wg_2 case the small difference between both loss channels (Γ_{rad} and Γ_{int}) results in an overall small Q, limited mainly by radiative losses for wavelengths below 1525 nm and by internal losses for higher wavelengths. In summary, the strong dependence of the intrinsic losses of the 2^{nd} family results in a peculiar behaviour where the system remains in undercoupling regime in wg_1, whereas for wg_2 it passes from overcoupled to undercoupled when the wavelength is increased.

Bibliography

[1] F. Morichetti, C. Ferrari, A. Canciamilla, and A. Melloni, "The first decade of coupled resonator optical waveguides: bringing slow light to applications," *Laser & Photonics Reviews*, vol. 6, no. 1, pp. 74–96, 2012.

[2] *Nonlinear Optics with Microresonators*, pp. 123–148. New York, NY: Springer New York, 2008.

[3] S. Azzini, D. Grassani, M. J. Strain, M. Sorel, L. Helt, J. Sipe, M. Liscidini, M. Galli, and D. Bajoni, "Ultra-low power generation of twin photons in a compact silicon ring resonator," *Optics express*, vol. 20, no. 21, pp. 23100–23107, 2012.

[4] A. Schliesser and T. J. Kippenberg, "Cavity optomechanics with whispering-gallery mode optical micro-resonators," *Advances In Atomic, Molecular, and Optical Physics*, vol. 58, pp. 207–323, 2010.

[5] R. G. Walker and C. D. W. Wilkinson, "Integrated optical ring resonators made by silver ion-exchange in glass," *Appl. Opt.*, vol. 22, pp. 1029–1035, Apr 1983.

[6] M. A. Foster, J. S. Levy, O. Kuzucu, K. Saha, M. Lipson, and A. L. Gaeta, "Silicon-based monolithic optical frequency comb source," *Optics Express*, vol. 19, no. 15, pp. 14233–14239, 2011.

[7] K. De Vos, I. Bartolozzi, E. Schacht, P. Bienstman, and R. Baets, "Silicon-on-insulator microring resonator for sensitive and label-free biosensing," *Optics express*, vol. 15, no. 12, pp. 7610–7615, 2007.

[8] K. Vandoorne, P. Mechet, T. Van Vaerenbergh, M. Fiers, G. Morthier, D. Verstraeten, B. Schrauwen, J. Dambre, and P. Bienstman, "Experimental demonstration of reservoir computing on a silicon photonics chip," *Nature communications*, vol. 5, 2014.

[9] M. Ghulinyan, R. Guider, G. Pucker, and L. Pavesi, "Monolithic whispering-gallery mode resonators with vertically coupled integrated bus waveguides," *IEEE Photonics Technology Letters*, vol. 23, no. 16, pp. 1166–1168, 2011.

[10] F. Turri, F. Ramiro-Manzano, I. Carusotto, M. Ghulinyan, G. Pucker, and L. Pavesi, "Wavelength dependence of a vertically coupled resonator-waveguide system," *Journal of Lightwave Technology*, vol. 34, no. 23, pp. 5385–5390, 2016.

[11] F. Ramiro-Manzano, M. Ghulinyan, N. Prtljaga, G. Pucker, and L. Pavesi, "Silicon-based monolithically integrated whispering-gallery mode resonators," in *SPIE LASE*, pp. 86001G–86001G, International Society for Optics and Photonics, 2013.

[12] F. Ramiro-Manzano, N. Prtljaga, L. Pavesi, G. Pucker, and M. Ghulinyan, "A fully integrated high-q whispering-gallery wedge resonator," *Optics express*, vol. 20, no. 20, pp. 22934–22942, 2012.

[13] M. Ghulinyan, F. R. Manzano, N. Prtljaga, M. Bernard, L. Pavesi, G. Pucker, and I. Carusotto, "Intermode reactive coupling induced by waveguide-resonator interaction," *Physical Review A*, vol. 90, no. 5, p. 053811, 2014.

[14] M. Ghulinyan, F. Ramiro-Manzano, N. Prtljaga, R. Guider, I. Carusotto, A. Pitanti, G. Pucker, and L. Pavesi, "Oscillatory vertical coupling between a whispering-gallery resonator and a bus waveguide," *Physical review letters*, vol. 110, no. 16, p. 163901, 2013.

[15] S. E. Miller, "Integrated optics: An introduction," *Bell Labs Technical Journal*, vol. 48, no. 7, pp. 2059–2069, 1969.

[16] H. Liang, R. Soref, J. Mu, X. Li, and W.-P. Huang, "Long range mid-infrared propagation in si and ge hybrid plasmonic-photonic nano-ribbon waveguides," *Opt. Express*, vol. 22, pp. 28489–28499, Nov 2014.

[17] L. Stefan, M. Bernard, R. Guider, G. Pucker, L. Pavesi, and M. Ghulinyan, "Ultra-high-q thin-silicon nitride strip-loaded ring resonators," *Optics letters*, vol. 40, no. 14, pp. 3316–3319, 2015.

[18] R. Yang, R. A. Wahsheh, Z. Lu, and M. A. G. Abushagur, "Efficient light coupling between dielectric slot waveguide and plasmonic slot waveguide," *Opt. Lett.*, vol. 35, pp. 649–651, Mar 2010.

[19] J. Dai, M. Zhang, F. Zhou, and D. Liu, "Highly efficient tunable optical filter based on liquid crystal micro-ring resonator with large free spectral range," *Frontiers of Optoelectronics*, vol. 9, no. 1, pp. 112–120, 2016.

[20] A. V. Krasavin and A. V. Zayats, "Silicon-based plasmonic waveguides," *Optics express*, vol. 18, no. 11, pp. 11791–11799, 2010.

[21] D. Dai and S. He, "A silicon-based hybrid plasmonic waveguide with a metal cap for a nano-scale light confinement," *Optics express*, vol. 17, no. 19, pp. 16646–16653, 2009.

[22] J. Broeng, D. Mogilevstev, S. E. Barkou, and A. Bjarklev, "Photonic crystal fibers: A new class of optical waveguides," *Optical fiber technology*, vol. 5, no. 3, pp. 305–330, 1999.

[23] B. E. Saleh, M. C. Teich, and B. E. Saleh, *Fundamentals of photonics*, vol. 22. Wiley New York, 1991.

[24] G. P. Agrawal, *Nonlinear fiber optics*. Academic press, 2007.

[25] R. W. Boyd, "Nonlinear optics," in *Handbook of Laser Technology and Applications (Three-Volume Set)*, pp. 161–183, Taylor & Francis, 2003.

[26] B. E. Saleh and M. C. Teich, "Nonlinear optics," *Fundamentals of Photonics*, pp. 737–798, 2001.

[27] M. Borselli, T. J. Johnson, and O. Painter, "Beyond the rayleigh scattering limit in high-q silicon microdisks: theory and experiment," *Optics express*, vol. 13, no. 5, pp. 1515–1530, 2005.

[28] E. Dulkeith, F. Xia, L. Schares, W. M. Green, and Y. A. Vlasov, "Group index and group velocity dispersion in silicon-on-insulator photonic wires," *Optics express*, vol. 14, no. 9, pp. 3853–3863, 2006.

[29] G. T. Reed, *Silicon Photonics: the state of the art*. John Wiley & Sons, 2008.

[30] Y. Namihira, "Relationship between nonlinear effective area and modefield diameter for dispersion shifted fibres," *Electronics Letters*, vol. 30, no. 3, pp. 262–264, 1994.

[31] D. J. Moss, R. Morandotti, A. L. Gaeta, and M. Lipson, "New cmos-compatible platforms based on silicon nitride and hydex for nonlinear optics," *Nature Photonics*, vol. 7, no. 8, pp. 597–607, 2013.

[32] "Whispering gallery modes microcavities on a si-chip." http://inac.cea.fr/en/Phocea/Vie_des_labos/Ast/ast_service.php?id_unit=844.

[33] "Nano-photonics and quantum electronics group, northwestern university." http://users.eecs.northwestern.edu/~sth/Research001.htm.

[34] X. Chen, M. Mohamed, Z. Li, L. Shang, and A. R. Mickelson, "Process variation in silicon photonic devices," *Applied optics*, vol. 52, no. 31, pp. 7638–7647, 2013.

[35] A. Mazzei, S. Götzinger, L. d. S. Menezes, V. Sandoghdar, and O. Benson, "Optimization of prism coupling to high-q modes in a microsphere resonator using a near-field probe," *Optics communications*, vol. 250, no. 4, pp. 428–433, 2005.

[36] M. Cai, G. Hunziker, and K. Vahala, "Fiber-optic add-drop device based on a silica microsphere-whispering gallery mode system," *IEEE Photonics Technology Letters*, vol. 11, no. 6, pp. 686–687, 1999.

[37] A. Polman, B. Min, J. Kalkman, T. Kippenberg, and K. Vahala, "Ultralow-threshold erbium-implanted toroidal microlaser on silicon," *Applied Physics Letters*, vol. 84, no. 7, pp. 1037–1039, 2004.

[38] D. Dai, Y. Shi, S. He, L. Wosinski, and L. Thylen, "Silicon hybrid plasmonic submicron-donut resonator with pure dielectric access waveguides," *Optics express*, vol. 19, no. 24, pp. 23671–23682, 2011.

[39] J. S. Levy, M. A. Foster, A. L. Gaeta, and M. Lipson, "Harmonic generation in silicon nitride ring resonators," *Optics express*, vol. 19, no. 12, pp. 11415–11421, 2011.

[40] M. A. Foster, A. C. Turner, J. E. Sharping, B. S. Schmidt, M. Lipson, and A. L. Gaeta, "Broad-band optical parametric gain on a silicon photonic chip," *Nature*, vol. 441, no. 7096, pp. 960–963, 2006.

[41] B. E. Little and W. Huang, "Coupled-mode theory for optical waveguides," *Progress In Electromagnetics Research*, vol. 10, pp. 217–270, 1995.

[42] M. L. Gorodetsky and V. S. Ilchenko, "Optical microsphere resonators: optimal coupling to high-q whispering-gallery modes," *JOSA B*, vol. 16, no. 1, pp. 147–154, 1999.

[43] L. F. Stokes, M. Chodorow, and H. J. Shaw, "All-single-mode fiber resonator," *Optics Letters*, vol. 7, no. 6, pp. 288–290, 1982.

[44] J. E. Heebner, V. Wong, A. Schweinsberg, R. W. Boyd, and D. J. Jackson, "Optical transmission characteristics of fiber ring resonators," *IEEE journal of quantum electronics*, vol. 40, no. 6, pp. 726–730, 2004.

[45] M. Fujita, R. Ushigome, and T. Baba, "Continuous wave lasing in gainasp microdisk injection laser with threshold current of 40/spl mu/a," *Electronics Letters*, vol. 36, no. 9, pp. 790–791, 2000.

[46] M. Hammer, K. R. Hiremath, R. Stoffer, F. Michelotti, A. Driessen, and M. Bertolotti, "Analytical approaches to the description of optical microresonator devices," in *AIP conference proceedings*, vol. 709, pp. 48–71, AIP, 2004.

[47] M. M. Mancinelli, *Linear and non linear coupling effects in sequence of microresonators*. PhD thesis, University of Trento, 2013.

[48] M. F. Yanik, S. Fan, and M. Soljačić, "High-contrast all-optical bistable switching in photonic crystal microcavities," *Applied Physics Letters*, vol. 83, no. 14, pp. 2739–2741, 2003.

[49] M. Borghi, *Linear, nonlinear and quantum optics in Silicon Photonics*. PhD thesis, University of Trento, 2016.

[50] F. Xia, L. Sekaric, and Y. Vlasov, "Ultracompact optical buffers on a silicon chip," *Nature photonics*, vol. 1, no. 1, pp. 65–71, 2007.

[51] J. B. Khurgin, "Optical buffers based on slow light in electromagnetically induced transparent media and coupled resonator structures: comparative analysis," *JOSA B*, vol. 22, no. 5, pp. 1062–1074, 2005.

[52] L. . i. e. j. J. Wang, A. Kuzmich, and A. Dogariu, "Gain-assisted superluminal light propagation," *Nature*, vol. 406, no. 6793, pp. 277–279, 2000.

[53] A. Dogariu, A. Kuzmich, and L. Wang, "Transparent anomalous dispersion and superluminal light-pulse propagation at a negative group velocity," *Physical Review A*, vol. 63, no. 5, p. 053806, 2001.

[54] R. Y. Chiao and P. W. Milonni, "Fast light, slow light," *Optics and Photonics News*, vol. 13, no. 6, pp. 26–31, 2002.

[55] L. L. Sánchez-Soto, J. J. Monzón, and G. Leuchs, "The many facets of the fabry–perot," *European Journal of Physics*, vol. 37, no. 6, p. 064001, 2016.

[56] R. R. Syms and J. R. Cozens, *Optical guided waves and devices*. McGraw-Hill, 1992.

[57] T. Chalyan, R. Guider, L. Pasquardini, M. Zanetti, F. Falke, E. Schreuder, R. G. Heideman, C. Pederzolli, and L. Pavesi, "Asymmetric mach–zehnder interferometer based biosensors for aflatoxin m1 detection," *Biosensors*, vol. 6, no. 1, p. 1, 2016.

[58] D. Yuan, Y. Dong, Y. Liu, and T. Li, "Mach-zehnder interferometer biochemical sensor based on silicon-on-insulator rib waveguide with large cross section," *Sensors*, vol. 15, no. 9, pp. 21500–21517, 2015.

[59] F. Prieto, B. Sepulveda, A. Calle, A. Llobera, C. Domınguez, and L. M. Lechuga, "Integrated mach–zehnder interferometer based on arrow structures for biosensor applications," *Sensors and actuators B: Chemical*, vol. 92, no. 1, pp. 151–158, 2003.

[60] Z. Lu, H. Yun, Y. Wang, Z. Chen, F. Zhang, N. A. Jaeger, and L. Chrostowski, "Broadband silicon photonic directional coupler using asymmetric-waveguide based phase control," *Optics express*, vol. 23, no. 3, pp. 3795–3808, 2015.

[61] D. K. Gifford, B. J. Soller, M. S. Wolfe, and M. E. Froggatt, "Optical vector network analyzer for single-scan measurements of loss, group delay, and polarization mode dispersion," *Applied optics*, vol. 44, no. 34, pp. 7282–7286, 2005.

[62] S. Mas, J. Matres, J. Marti, and C. Oton, "Accurate chromatic dispersion characterization of photonic integrated circuits," *IEEE Photonics Journal*, vol. 4, no. 3, pp. 825–831, 2012.

[63] S. Biasi, F. Ramiro-Manzano, P.-É. Larré, F. Turri, M. Ghulinyan, G. Pucker, I. Carusotto, and L. Pavesi, "Transmittance and phase fano line-shape spectra induced by reactive coupling in an integrated microresonator," to be published.

[64] M.-C. Tien, J. F. Bauters, M. J. Heck, D. T. Spencer, D. J. Blumenthal, and J. E. Bowers, "Ultra-high quality factor planar si 3 n 4 ring resonators on si substrates," *Optics express*, vol. 19, no. 14, pp. 13551–13556, 2011.

[65] B.-B. Li, Y.-F. Xiao, C.-L. Zou, Y.-C. Liu, X.-F. Jiang, Y.-L. Chen, Y. Li, and Q. Gong, "Experimental observation of fano resonance in a single whispering-gallery microresonator," *Applied Physics Letters*, vol. 98, no. 2, p. 021116, 2011.

[66] G. Cocorullo, F. G. Della Corte, I. Rendina, and P. M. Sarro, "Thermo-optic effect exploitation in silicon microstructures," *Sensors and Actuators A: Physical*, vol. 71, no. 1, pp. 19–26, 1998.

[67] "http://lunainc.com/ova5000."

[68] S. Spillane, T. Kippenberg, O. Painter, and K. Vahala, "Ideality in a fiber-taper-coupled microresonator system for application to cavity quantum electrodynamics," *Physical Review Letters*, vol. 91, no. 4, p. 043902, 2003.

[69] H. A. Haus, *Waves and fields in optoelectronics*. Prentice-Hall,, 1984.

[70] T. Carmon, S. Y. Wang, E. P. Ostby, and K. J. Vahala, "Wavelength-independent coupler from fiber to an on-chip cavity, demonstrated over an 850nm span," *Optics express*, vol. 15, no. 12, pp. 7677–7681, 2007.

[71] A. Yariv, "Universal relations for coupling of optical power between microresonators and dielectric waveguides," *Electronics letters*, vol. 36, no. 4, pp. 321–322, 2000.

[72] D. Gandolfi, F. Ramiro-Manzano, F. J. Aparicio Rebollo, M. Ghulinyan, G. Pucker, and L. Pavesi, "Role of edge inclination in an optical microdisk resonator for label-free sensing," *Sensors*, vol. 15, no. 3, pp. 4796–4809, 2015.

[73] A. Yariv, "Critical coupling and its control in optical waveguide-ring resonator systems," *IEEE Photonics Technology Letters*, vol. 14, no. 4, pp. 483–485, 2002.

[74] L.-W. Luo, S. Ibrahim, A. Nitkowski, Z. Ding, C. B. Poitras, S. B. Yoo, and M. Lipson, "High bandwidth on-chip silicon photonic interleaver," *Optics express*, vol. 18, no. 22, pp. 23079–23087, 2010.

[75] F. Ramiro-Manzano, N. Prtljaga, L. Pavesi, G. Pucker, and M. Ghulinyan, "Monolithic integration of high-q wedge resonators with vertically coupled waveguides," in *SPIE Microtechnologies*, pp. 876704–876704, International Society for Optics and Photonics, 2013.

[76] H.-P. Breuer and F. Petruccione, *The theory of open quantum systems*. Oxford University Press on Demand, 2002.

[77] R. G. Hulet, E. S. Hilfer, and D. Kleppner, "Inhibited spontaneous emission by a rydberg atom," *Physical review letters*, vol. 55, no. 20, p. 2137, 1985.

[78] P. Lodahl, A. F. Van Driel, I. S. Nikolaev, A. Irman, K. Overgaag, D. Vanmaekelbergh, and W. L. Vos, "Controlling the dynamics of spontaneous emission from quantum dots by photonic crystals," *Nature*, vol. 430, no. 7000, pp. 654–657, 2004.

[79] W. E. Lamb Jr and R. C. Retherford, "Fine structure of the hydrogen atom by a microwave method," *Physical Review*, vol. 72, no. 3, p. 241, 1947.

[80] M. I. Tribelsky, S. Flach, A. E. Miroshnichenko, A. V. Gorbach, and Y. S. Kivshar, "Light scattering by a finite obstacle and fano resonances," *Physical review letters*, vol. 100, no. 4, p. 043903, 2008.

[81] A. B. Matsko, *Practical applications of microresonators in optics and photonics*. CRC Press, 2009.

[82] M. A. Popović, C. Manolatou, and M. R. Watts, "Coupling-induced resonance frequency shifts in coupled dielectric multi-cavity filters," *Optics Express*, vol. 14, no. 3, pp. 1208–1222, 2006.

[83] Q. Xu, S. Sandhu, M. L. Povinelli, J. Shakya, S. Fan, and M. Lipson, "Experimental realization of an on-chip all-optical analogue to electromagnetically induced transparency," *Physical review letters*, vol. 96, no. 12, p. 123901, 2006.

[84] K.-J. Boller, A. Imamoğlu, and S. E. Harris, "Observation of electromagnetically induced transparency," *Physical Review Letters*, vol. 66, no. 20, p. 2593, 1991.

[85] L. Maleki, A. Matsko, A. Savchenkov, and V. Ilchenko, "Tunable delay line with interacting whispering-gallery-mode resonators," *Optics letters*, vol. 29, no. 6, pp. 626–628, 2004.

[86] S. Weis, R. Rivière, S. Deléglise, E. Gavartin, O. Arcizet, A. Schliesser, and T. J. Kippenberg, "Optomechanically induced transparency," *Science*, vol. 330, no. 6010, pp. 1520–1523, 2010.

[87] S. Fan, W. Suh, and J. Joannopoulos, "Temporal coupled-mode theory for the fano resonance in optical resonators," *JOSA A*, vol. 20, no. 3, pp. 569–572, 2003.

[88] C.-H. Dong, C.-L. Zou, Y.-F. Xiao, J.-M. Cui, Z.-F. Han, and G.-C. Guo, "Modified transmission spectrum induced by two-mode interference in a single silica microsphere," *Journal of Physics B: Atomic, Molecular and Optical Physics*, vol. 42, no. 21, p. 215401, 2009.

[89] U. Fano, "Effects of configuration interaction on intensities and phase shifts," *Physical Review*, vol. 124, no. 6, p. 1866, 1961.

[90] A. E. Miroshnichenko, S. Flach, and Y. S. Kivshar, "Fano resonances in nanoscale structures," *Reviews of Modern Physics*, vol. 82, no. 3, p. 2257, 2010.

[91] B.-B. Li, Y.-F. Xiao, C.-L. Zou, Y.-C. Liu, X.-F. Jiang, Y.-L. Chen, Y. Li, and Q. Gong, "Experimental observation of fano resonance in a single whispering-gallery microresonator," *Applied Physics Letters*, vol. 98, no. 2, p. 021116, 2011.

[92] J.-B. Shim, P. Schlagheck, M. Hentschel, and J. Wiersig, "Nonlinear dynamical tunneling of optical whispering gallery modes in the presence of a kerr nonlinearity," *Physical Review A*, vol. 94, no. 5, p. 053849, 2016.

[93] M. Bernard, F. R. Manzano, L. Pavesi, G. Pucker, I. Carusotto, and M. Ghulinyan, "Complete crossing of fano resonances in an optical microcavity via nonlinear tuning," *arXiv preprint arXiv:1701.06332*, 2017.

[94] Y.-F. Xiao, V. Gaddam, and L. Yang, "Coupled optical microcavities: an enhanced refractometric sensing configuration," *Optics express*, vol. 16, no. 17, pp. 12538–12543, 2008.

[95] C.-Y. Chao and L. J. Guo, "Biochemical sensors based on polymer microrings with sharp asymmetrical resonance," *Applied Physics Letters*, vol. 83, no. 8, pp. 1527–1529, 2003.

[96] L. Y. Mario, S. Darmawan, and M. K. Chin, "Asymmetric fano resonance and bistability for high extinction ratio, large modulation depth, and low power switching," *Optics express*, vol. 14, no. 26, pp. 12770–12781, 2006.

[97] S. F. Mingaleev, A. E. Miroshnichenko, and Y. S. Kivshar, "Coupled-resonator-induced reflection in photonic-crystal waveguide structures," *Optics express*, vol. 16, no. 15, pp. 11647–11659, 2008.

[98] K. Totsuka, N. Kobayashi, and M. Tomita, "Slow light in coupled-resonator-induced transparency," *Physical review letters*, vol. 98, no. 21, p. 213904, 2007.

[99] D. Weiss, V. Sandoghdar, J. Hare, V. Lefevre-Seguin, J.-M. Raimond, and S. Haroche, "Splitting of high-q mie modes induced by light backscattering in silica microspheres," *Optics letters*, vol. 20, no. 18, pp. 1835–1837, 1995.

[100] F. Morichetti, A. Canciamilla, and A. Melloni, "Statistics of backscattering in optical waveguides," *Optics letters*, vol. 35, no. 11, pp. 1777–1779, 2010.

[101] Q. Li, Z. Zhang, J. Wang, M. Qiu, and Y. Su, "Fast light in silicon ring resonator with resonance-splitting," *Optics express*, vol. 17, no. 2, pp. 933–940, 2009.

[102] A. Li, T. Vaerenbergh, P. Heyn, P. Bienstman, and W. Bogaerts, "Backscattering in silicon microring resonators: a quantitative analysis," *Laser & Photonics Reviews*, vol. 10, no. 3, pp. 420–431, 2016.

[103] Y. Hu, L. Shao, S. Arnold, Y.-C. Liu, C.-Y. Ma, and Y.-F. Xiao, "Mode broadening induced by nanoparticles in an optical whispering-gallery microcavity," *Physical Review A*, vol. 90, no. 4, p. 043847, 2014.

[104] J. Wu, B. Liu, J. Peng, J. Mao, X. Jiang, C. Qiu, C. Tremblay, and Y. Su, "On-chip tunable second-order differential-equation solver based on a silicon photonic mode-split microresonator," *Journal of Lightwave Technology*, vol. 33, no. 17, pp. 3542–3549, 2015.

[105] J. Zhu, S. K. Ozdemir, Y.-F. Xiao, L. Li, L. He, D.-R. Chen, and L. Yang, "On-chip single nanoparticle detection and sizing by mode splitting in an ultrahigh-q microresonator," *Nature photonics*, vol. 4, no. 1, pp. 46–49, 2010.

[106] T. Kippenberg, S. Spillane, and K. Vahala, "Modal coupling in traveling-wave resonators," *Optics letters*, vol. 27, no. 19, pp. 1669–1671, 2002.

[107] G. Gao, D. Li, Y. Zhang, S. Yuan, A. Armghan, Q. Huang, Y. Wang, J. Yu, and J. Xia, "Tuning of resonance spacing over whole free spectral range based on autler-townes splitting in a single microring resonator," *Optics express*, vol. 23, no. 21, pp. 26895–26904, 2015.

[108] A. Li and W. Bogaerts, "Fundamental suppression of backscattering in silicon microrings," *Optics Express*, vol. 25, no. 3, pp. 2092–2099, 2017.

[109] G. Ballesteros, J. Matres, J. Martí, and C. Oton, "Characterizing and modeling backscattering in silicon microring resonators," *Optics express*, vol. 19, no. 25, pp. 24980–24985, 2011.

[110] Z. Zhang, M. Dainese, L. Wosinski, and M. Qiu, "Resonance-splitting and enhanced notch depth in soi ring resonators with mutual mode coupling," *Optics express*, vol. 16, no. 7, pp. 4621–4630, 2008.

[111] J. Matres and W. V. Sorin, "Simple model for ring resonators backscatter," *Optics Express*, vol. 25, no. 4, pp. 3242–3251, 2017.

[112] S. Tallur and S. A. Bhave, "Rayleigh scattering boosted multi-ghz displacement sensitivity in whispering gallery opto-mechanical resonators," *Optics express*, vol. 21, no. 23, pp. 27780–27788, 2013.

[113] S. Tallur and S. A. Bhave, "A silicon electromechanical photodetector," *Nano letters*, vol. 13, no. 6, pp. 2760–2765, 2013.

[114] A. Li, T. Van Vaerenbergh, Y. Xing, P. Bienstman, W. Bogaerts, *et al.*, "Experimentally demonstrate the origin for asymmetric resonance splitting and contributions from couplers to backscattering in soi microrings," in *Integrated Photonics Research, Silicon and Nanophotonics*, pp. IM2B–6, Optical Society of America, 2015.

[115] D. Melati, A. Melloni, and F. Morichetti, "Real photonic waveguides: guiding light through imperfections," *Advances in Optics and Photonics*, vol. 6, no. 2, pp. 156–224, 2014.

[116] T. J. A. Kippenberg, *Nonlinear optics in ultra-high-Q whispering-gallery optical microcavities*. PhD thesis, California Institute of Technology, 2004.

[117] B. E. Little, J.-P. Laine, and S. T. Chu, "Surface-roughness-induced contradirectional coupling in ring and disk resonators," *Optics letters*, vol. 22, no. 1, pp. 4–6, 1997.

[118] M. Xian-Wu, B. Jiang-Xiang, and L. De-Jun, "Optomechanical entanglement in a whispering-gallery cavity," *Chinese Physics B*, vol. 21, no. 3, p. 030303, 2012.

[119] Q.-T. Cao, H. Wang, C.-H. Dong, H. Jing, R.-S. Liu, X. Chen, L. Ge, Q. Gong, and Y.-F. Xiao, "Experimental demonstration of spontaneous chirality in a nonlinear microresonator," *Phys. Rev. Lett.*, vol. 118, p. 033901, Jan 2017.

[120] L. Del Bino, J. M. Silver, S. L. Stebbings, and P. Del'Haye, "Symmetry breaking of counter-propagating light in a nonlinear resonator," *Nature Reports*, 2017.

[121] A. Mazzei, S. Götzinger, L. d. S. Menezes, G. Zumofen, O. Benson, and V. Sandoghdar, "Controlled coupling of counterpropagating whispering-gallery modes by a single rayleigh scatterer: a classical problem in a quantum optical light," *Physical review letters*, vol. 99, no. 17, p. 173603, 2007.

[122] A. C. Hryciw, R. D. Kekatpure, S. Yerci, L. Dal Negro, and M. L. Brongersma, "Thermo-optic tuning of erbium-doped amorphous silicon nitride microdisk resonators," *Applied Physics Letters*, vol. 98, no. 4, p. 041102, 2011.

[123] F. G. Della Corte, G. Cocorullo, M. Iodice, and I. Rendina, "Temperature dependence of the thermo-optic coefficient of inp, gaas, and sic from room temperature to 600 k at the wavelength of 1.5 μm," *Applied Physics Letters*, vol. 77, no. 11, pp. 1614–1616, 2000.

[124] S. Feng, T. Lei, H. Chen, H. Cai, X. Luo, and A. W. Poon, "Silicon photonics: from a microresonator perspective," *Laser & photonics reviews*, vol. 6, no. 2, pp. 145–177, 2012.

[125] S. Manipatruni, R. K. Dokania, B. Schmidt, N. Sherwood-Droz, C. B. Poitras, A. B. Apsel, and M. Lipson, "Wide temperature range operation of micrometer-scale silicon electro-optic modulators," *Optics letters*, vol. 33, no. 19, pp. 2185–2187, 2008.

[126] G. T. Reed, G. Mashanovich, F. Gardes, and D. Thomson, "Silicon optical modulators," *Nature photonics*, vol. 4, no. 8, pp. 518–526, 2010.

[127] V. Van, T. Ibrahim, P. Absil, F. Johnson, R. Grover, and P.-T. Ho, "Optical signal processing using nonlinear semiconductor microring resonators," *IEEE Journal of Selected Topics in Quantum Electronics*, vol. 8, no. 3, pp. 705–713, 2002.

[128] W. Yoshiki and T. Tanabe, "Analysis of bistable memory in silica toroid microcavity," *JOSA B*, vol. 29, no. 12, pp. 3335–3343, 2012.

[129] M. Cazzanelli, F. Bianco, E. Borga, G. Pucker, M. Ghulinyan, E. Degoli, E. Luppi, V. Véniard, S. Ossicini, D. Modotto, *et al.*, "Second-harmonic generation in silicon waveguides strained by silicon nitride," *Nature materials*, vol. 11, no. 2, pp. 148–154, 2012.

[130] C.-S. Kim, Y. Han, B. H. Lee, W.-T. Han, U.-C. Paek, and Y. Chung, "Induction of the refractive index change in b-doped optical fibers through relaxation of the mechanical stress," *Optics Communications*, vol. 185, no. 4, pp. 337–342, 2000.

[131] T. Toyoda and M. Yabe, "The temperature dependence of the refractive indices of fused silica and crystal quartz," *Journal of Physics D: Applied Physics*, vol. 16, no. 5, p. L97, 1983.

[132] Q. Xu, S. Manipatruni, B. Schmidt, J. Shakya, and M. Lipson, "12.5 gbit/s carrier-injection-based silicon micro-ring silicon modulators," *Optics express*, vol. 15, no. 2, pp. 430–436, 2007.

[133] Q. Xu and M. Lipson, "Carrier-induced optical bistability in silicon ring resonators," *Optics letters*, vol. 31, no. 3, pp. 341–343, 2006.

[134] M. Soljačić, M. Ibanescu, S. G. Johnson, Y. Fink, and J. Joannopoulos, "Optimal bistable switching in nonlinear photonic crystals," *Physical Review E*, vol. 66, no. 5, p. 055601, 2002.

[135] D. Hohlfeld and H. Zappe, "An all-dielectric tunable optical filter based on the thermo-optic effect," *Journal of optics A: Pure and applied Optics*, vol. 6, no. 6, p. 504, 2004.

[136] F. Ramiro-Manzano, N. Prtljaga, L. Pavesi, G. Pucker, and M. Ghulinyan, "Thermo-optical bistability with si nanocrystals in a whispering gallery mode resonator," *Optics letters*, vol. 38, no. 18, pp. 3562–3565, 2013.

[137] A. Arbabi and L. L. Goddard, "Measurements of the refractive indices and thermo-optic coefficients of si 3 n 4 and sio x using microring resonances," *Optics letters*, vol. 38, no. 19, pp. 3878–3881, 2013.

[138] G. Cocorullo, F. G. Della Corte, M. Iodice, I. Rendina, and P. M. Sarro, "A temperature all-silicon micro-sensor based on the thermo-optic effect," *IEEE Transactions on electron devices*, vol. 44, no. 5, pp. 766–774, 1997.

[139] G. Guan, S. Arnold, and V. Otugen, "Temperature measurements using a microoptical sensor based on whispering gallery modes," *AIAA journal*, vol. 44, no. 10, pp. 2385–2389, 2006.

[140] B.-B. Li, Q.-Y. Wang, Y.-F. Xiao, X.-F. Jiang, Y. Li, L. Xiao, and Q. Gong, "On chip, high-sensitivity thermal sensor based on high-q polydimethylsiloxane-coated microresonator," *Applied Physics Letters*, vol. 96, no. 25, p. 251109, 2010.

[141] G.-D. Kim, H.-S. Lee, C.-H. Park, S.-S. Lee, B. T. Lim, H. K. Bae, and W.-G. Lee, "Silicon photonic temperature sensor employing a ring resonator manufactured using a standard cmos process," *Optics express*, vol. 18, no. 21, pp. 22215–22221, 2010.

[142] M. W. Geis, S. J. Spector, R. Williamson, and T. Lyszczarz, "Submicrosecond submilliwatt silicon-on-insulator thermooptic switch," *IEEE photonics technology letters*, vol. 16, no. 11, pp. 2514–2516, 2004.

[143] M. Harjanne, M. Kapulainen, T. Aalto, and P. Heimala, "Sub-microsecond switching time in silicon-on-insulator mach-zehnder thermooptic switch," *IEEE Photonics Technology Letters*, vol. 16, no. 9, pp. 2039–2041, 2004.

[144] J. B. Khurgin, G. Sun, W. T. Chen, W.-Y. Tsai, and D. P. Tsai, "Ultrafast thermal nonlinearity," in *Lasers and Electro-Optics (CLEO), 2016 Conference on*, pp. 1–2, IEEE, 2016.

[145] W. Bogaerts, P. De Heyn, T. Van Vaerenbergh, K. De Vos, S. Kumar Selvaraja, T. Claes, P. Dumon, P. Bienstman, D. Van Thourhout, and R. Baets, "Silicon microring resonators," *Laser & Photonics Reviews*, vol. 6, no. 1, pp. 47–73, 2012.

[146] T. Liang, L. Nunes, T. Sakamoto, K. Sasagawa, T. Kawanishi, M. Tsuchiya, G. Priem, D. Van Thourhout, P. Dumon, R. Baets, *et al.*, "Ultrafast all-optical switching by cross-absorption modulation in silicon wire waveguides," *Optics Express*, vol. 13, no. 19, pp. 7298–7303, 2005.

[147] J. S. Pelc, K. Rivoire, S. Vo, C. Santori, D. A. Fattal, and R. G. Beausoleil, "Picosecond all-optical switching in hydrogenated amorphous silicon microring resonators," *Optics express*, vol. 22, no. 4, pp. 3797–3810, 2014.

[148] J. Petrcek, Y. Eksioglu, and A. Sterkhova, "Simulation of self-pulsing in kerr-nonlinear coupled ring resonators," *Optics Communications*, vol. 318, pp. 147–151, 2014.

[149] M. Mancinelli, M. Borghi, F. Ramiro-Manzano, J. Fedeli, and L. Pavesi, "Chaotic dynamics in coupled resonator sequences," *Optics express*, vol. 22, no. 12, pp. 14505–14516, 2014.

[150] P. E. Barclay, K. Srinivasan, and O. Painter, "Nonlinear response of silicon photonic crystal microresonators excited via an integrated waveguide and fiber taper," *Optics express*, vol. 13, no. 3, pp. 801–820, 2005.

[151] L. Zhou, K. Okamoto, and S. Yoo, "Athermalizing and trimming of slotted silicon microring resonators with uv-sensitive pmma upper-cladding," *IEEE Photonics Technology Letters*, vol. 21, no. 17, pp. 1175–1177, 2009.

[152] R. Shankar, I. Bulu, R. Leijssen, and M. Lončar, "Study of thermally-induced optical bistability and the role of surface treatments in si-based mid-infrared photonic crystal cavities," *Optics express*, vol. 19, no. 24, pp. 24828–24837, 2011.

[153] S. Weiss, M. Molinari, and P. Fauchet, "Temperature stability for silicon-based photonic band-gap structures," *Applied Physics Letters*, vol. 83, no. 10, pp. 1980–1982, 2003.

[154] T. Carmon, L. Yang, and K. J. Vahala, "Dynamical thermal behavior and thermal self-stability of microcavities," *Optics Express*, vol. 12, no. 20, pp. 4742–4750, 2004.

[155] C. Baker, S. Stapfner, D. Parrain, S. Ducci, G. Leo, E. M. Weig, and I. Favero, "Optical instability and self-pulsing in silicon nitride whispering gallery resonators," *Optics express*, vol. 20, no. 27, pp. 29076–29089, 2012.

[156] P.-É. Larré and I. Carusotto, "Propagation of a quantum fluid of light in a cavityless nonlinear optical medium: General theory and response to quantum quenches," *Physical Review A*, vol. 92, no. 4, p. 043802, 2015.

[157] P.-É. Larré, S. Biasi, F. Ramiro-Manzano, L. Pavesi, and I. Carusotto, "Bogoliubov dispersion relation in a channel optical waveguide," *arXiv preprint arXiv:1612.07485*, 2016.

Ringraziamenti

Ho saltato i ringraziamenti per la laurea triennale, ho saltato quelli per la magistrale, forse con il dottorato ce la facciamo.
Ringrazio il professor Pavesi, perchè in questi anni mi ha dimostrato piena disponibilità ed è stato paziente e comprensivo, nonostante gli immancabili ritardi nelle consegne.
Ringrazio Fernando e Stefano per le (dis)avventure in laboratorio che hanno permesso a questa tesi di realizzarsi, non so come avrei fatto senza.
Ringrazio i compagni del NanoLab, italiani e non, con i quali ho condiviso gioie (e dolori) della fisica sperimentale, ma anche della mensa (ah, la mensa) e delle gite fuori porta (ah, la Sicilia...a proposito, chi è il prossimo che organizza un matrimonio, possibilmente al mare).
Ringrazio Tanya, che permette al NanoLab di funzionare senza (troppi) intoppi.
Ringrazio anche Mher e Georg, perchè con un solo run sono riusciti a creare il dispositivo più fruttuoso del nostro laboratorio.
Ringrazio i Fisici_TN, compagni di studio matto e disperatissimo, che alla fine sono diventati un gran bel gruppo di amici. Probabilmente non vi dedico abbastanza tempo, però sappiate che è sempre un piacere rivedervi.
Ringrazio in particolar modo Fabrizio, Lorenzo, Zeno e Martino, per avermi sopportato negli anni di studio a Povo (va beh, ci sono anche Marco, Mattia e Nicolò, ma loro sono ingegneri e matematici, quindi non contano). Sono stati anni intensi e preziosi e sono contento di averli condivisi con voi.
Forse in modo un po' insolito, ringrazio i miei professori di fisica delle superiori, il Marco Cazzaniga e il Gigi Vaona, perchè hanno fatto crescere in me la passione per la fisica, al punto da farla diventare un lavoro. Ringrazio anche la professoressa Tonici e la maestra Emanuela, perchè in fondo è grazie a loro che questa passione è nata.
Non so quante volte ancora potrò permettermi di scrivere una pagina di ringraziamenti, perciò mi prendo la libertà di inserire anche le persone che mi circondano, che non sono strettamente legate alla tesi, che però hanno contribuito a farmi raggiungere questo obiettivo.
Ringrazio la mia mamma, perchè è stata la mia prima insegnante, perchè ha fatto di tutto per me e ancora continua a farlo.
Ringrazio mio papà, perchè c'è sempre stato quando ne avevo bisogno, e perchè mi ha trasmesso la serenità e la pazienza che tanto mi sono di aiuto.
Ringrazio Nico, da quando siamo nati sei sempre stato una spalla su cui poter contare.
Ringrazio la famiglia allargata degli zii e dei nonni, perchè sono stati sempre un punto fermo, con loro sono cresciuto e mi sono divertito. Continuate così!
Ringrazio Silvia, per aver scelto di diventare mia amica, morosa, fidanzata e moglie (in quest'ordine). Senza di te sarei a metà.
Infine un grazie alla Cate, che mi ricorda ogni giorno quali sono le cose importanti nella mia vita.